DISC WINDS AND LINE-WIDTH DISTRIBUTIONS IN ACTIVE GALACTIC NUCLEI

LAURA S. CHAJET

A DISSERTATION SUBMITTED TO
THE FACULTY OF GRADUATE STUDIES
IN PARTIAL FULFILMENT OF THE REQUIREMENTS
FOR THE DEGREE OF
DOCTOR OF PHILOSOPHY

GRADUATE PROGRAM IN PHYSICS AND ASTRONOMY
YORK UNIVERSITY
TORONTO, ONTARIO

DECEMBER 2015

Abstract

We study Active Galactic Nucleus (AGN) emission-line profiles by combining an improved version of the accretion disc-wind model of Murray & Chiang with the magneto-hydrodynamic model of Emmering et al. We consider central objects with different masses and/or luminosities. We show how the shape, broadening and shift of the C IV line depend not only on the viewing angle to the object but also on the wind launching angle, especially for small launching angles. We have compared the dispersions in our model C IV line-width distributions to observational upper limits on that dispersion, considering both smooth and clumpy torus models. Following Fine et al., we transform that scatter in the profile line-widths into a constraint on the torus geometry. We show how the half-opening angle of the obscuring structure depends on the mass and luminosity of the central object.

Acknowledgements

I would like to thank my supervisor, Professor Patrick Hall, for his support and guidance during this work.

I would also like to thank the two other members of my supervisory committee, Professors De Robertis and McCall for their insightful suggestions and comments during the years as a Ph.D. candidate.

My immense gratitude to Marlene Caplan, for being always so caring and helping me in all circumstances. Thanks also to Professor Paul Delaney, Director of the Natural Science Division at York University, who has always been so open and friendly.

To all them, my additional thanks for their patience and understanding during the difficult moments when I was sick and under treatment.

Many thanks to al members of the examining committee, for their insightful comments on the thesis. In particular, I would like to thank Prof. Michael Eracleous, the committee external member, for his feedback and very helpful comments and suggestions and also for the interesting discussions that we had during his visits to York.

Thanks also to my fellow students, who helped me in a variety of ways. My special thanks to my former officemate, Sunne Dong with whom I share the passion for science and art, and George Conidis, with whom I had so many long conversations, spanning from astrophysics to history to music, etc. They were of great support during these years, but particularly during my illness.

Thanks to my family: my parents (my mom passed away two years ago, but it is as she still were there), my brother and my mother-in-law, and my two wonderful nephews, Jesica and Alex.

And the biggest of all thanks to my husband Jorge, for his love and support. Without him and his constant encouragement I could not have finished this work, or gone through the difficulties I faced. And thanks to my cats, Amelia and Bentley, and my late ones, Venus and Apolo, for their love and company.

Table of Contents

List of Tables

List of Figures

Abbreviations

- 2QZ: 2dF QSO Redshift survey (2dF: 2-degree Field)
- 2SLAQ: 2dF-SDSS LRG and QSO survey (LRG: Luminous Red Galaxy)
- AGN: Active Galaxy Nucleus
- BAL: Broad Absorption Line
- BEL: Broad Emission Line
- BH: Black Hole
- BLR: Broad Line Region
- EQW: Equivalent Width
- FWHM: Full Width at Half-Maximum
- IPV: Inter-Percentile Value
- LOS: Line of Sight

- MHD: MagnetoHydrodynamics
- NLR: Narrow Line Region
- (N)IR: (Near) Infrared
- ODE: Ordinary Differential Equation
- PDE: Partial Differential Equation
- QSO: Quasi-Stellar Object
- RM: Reverberation Mapping
- SDSS: Sloan Digital Sky Survey
- SED: Spectral Energy Distribution
- SMBH: Super Massive Black Hole
- UV: Ultraviolet

1 Introduction

This chapter is devoted to an overview of the Active Galactic Nucleus phenomenon, and serves to introduce definitions that will be needed in subsequent chapters.

It has been recently found that most (if not all) sufficiently massive galaxies harbour a supermassive black hole (SMBH) at the centre (e.g. Kormendy & Richstone 1995; Magorrian et al. 1998; McLure & Dunlop 2001; Decarli et al. 2007). Moreover, it has been shown that there is a tight relationship between the masses of the black holes and the galaxy bulges (e.g. Marconi & Hunt 2003; Häring & Rix 2004; Gültekin et al. 2009), suggesting their co-evolution. In a fraction of those galaxies, collectively known as active galactic nuclei (AGN), the central region releases enormous amounts of energy at virtually all wavelengths from radio to the X-ray (and in some cases, the γ-ray) range. These active nuclei are so luminous that they often outshine the rest of the galaxy.

Active galaxies are defined as galaxies with an energy source in the central portion of the galaxy, or the bulge, that emits radiation that cannot be attributed to stars. This radiation usually has a high energy tail that follows a power law, $F_\nu \propto \nu^{-\alpha}$, where α is

the spectral index. We first introduce the currently most accepted model of the physical structure of AGN, and highlight the corresponding features observed in their spectral energy distributions (SEDs) and spectra. This favoured "unified" model (Antonucci 1993, Urry & Padovani 1995), based on a phenomenological description, can be (and has been) used to explain the different observational classes of AGN. Basically, the model posits that different classes of AGN are intrinsically the same kind of object seen from different directions. This model does not account for all observational characteristics of AGN, and certainly requires some modifications, as suggested by many authors (e.g., Nenkova et al. 2008; Elvis 2012; Bianchi et al. 2012), but its major aspects are still widely accepted.

1.1 Standard Model

In the standard paradigm, AGNs are assumed to be powered by accretion onto a supermassive black hole (SMBH), with masses in the range 10^6 - 10^{10} $M_\odot$ (e.g. Zeldovich & Novikov 1964; Lynden-Bell 1969; Rees 1984). The accreting structure, assumed to be disc-like, consists of a hot (10^4 - 10^6 K) and normally optically thick plasma, that is responsible for most of the ultraviolet (UV) and optical continuum emission. The broad emission lines, prominent in the UV/optical spectra of many AGNs, are explained by photoionization of the dense gas surrounding the central engine, in the broad line region (BLR). The central region is embedded in a dusty molecular torus that obscures some lines of sight (LOS) to the nucleus, accounting for some of the AGN phenomenon diver-

sity (e.g. Elitzur 2008). The torus is replaced by a warped disc in some models, (e.g. Lawrence & Elvis 2010). At larger distances ($r \sim 100 - 1000$ pc) lies the narrow line region (NLR), a less dense ($n \sim 10^3 - 10^6$ cm^{-3}) gas structure. The gas there, photoionised by the nuclear radiation field, emits allowed and forbidden narrow lines. Figure 1.1, from Mundell et al. (1995), shows a depiction of the AGN unification paradigm. Note that the BLR is shown as system of individual cloudlets although in the model applied to this work it is a wind originating above the disc.

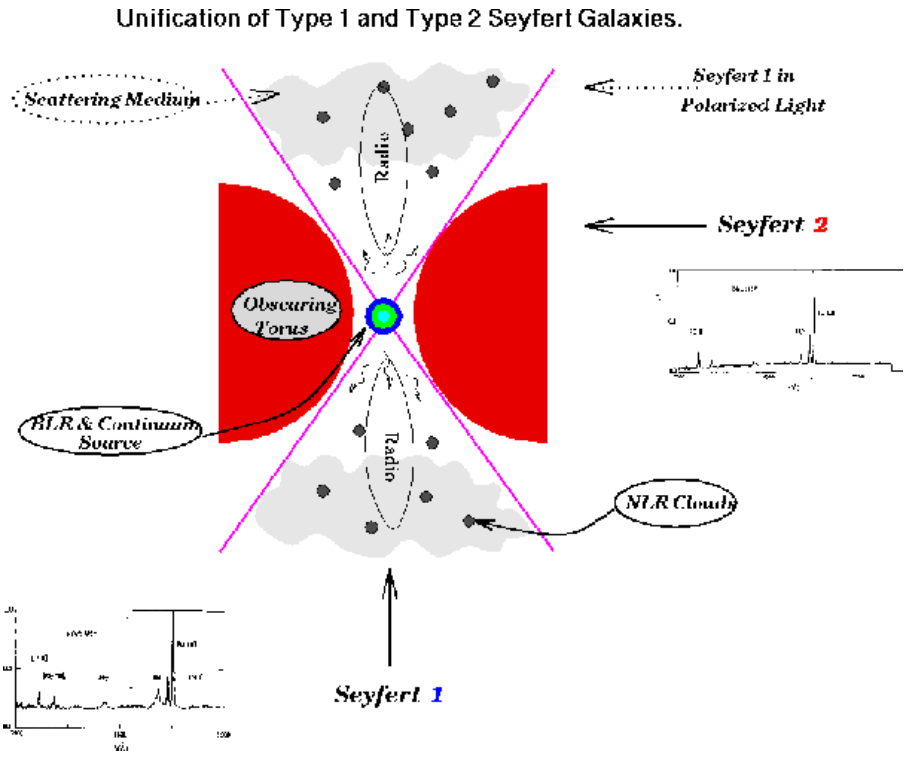

Figure 1.1: Schematic representation of our understanding of the AGN phenomenon in the unified scheme, adopted from Mundell et al. (1995). The type of object we see depends on the viewing angle, whether or not the AGN produces a significant jet emission, and how powerful the central engine is.

1.1.1 The central engine

The standard physical model of an AGN starts with a central black hole (BH) that is growing via mass accretion. The accretion luminosity is given by

$$L_{\rm acc} = \eta \dot{M} c^2, \tag{1.1}$$

where $\dot{M}$ is the mass accretion rate, c is the speed of light in a vacuum, and η is the mass-energy efficiency conversion. The accretion efficiency depends on the location of the innermost stable orbit, $R_{\rm ISCO}$, which in turn is dependent on the black hole spin. For a spin zero Scwarzschild black hole this is predicted to be $\eta = 0.057$. In the case of a spinning (Kerr) BH, the efficiency depends on the direction of the motion with respect to the direction of the black hole. Calculations indicate that in the case of co-rotation around a maximally spinning Kerr BH, $\eta = 0.42$, neglecting the fact that some liberated energy close to the horizon will be lost to the black hole. Including this effect a more realistic value would be $\eta = 0.3$ (Thorne 1974). A theoretical upper limit on $L_{\rm acc}$ can be calculated assuming accretion of fully ionised hydrogen onto a BH of mass $M_{\rm BH}$, when the force of gravity is equal to the radiation pressure from the accretion luminosity. This upper-limit is known as the "Eddington luminosity" and is given by

$$L_{\rm Edd} = \frac{4\pi G M m_{\rm p} c}{\sigma_{\rm T}} \approx 1.3 \times 10^{38}\ (M_{\rm BH}/M_{\odot})\ {\rm erg\ s^{-1}}, \tag{1.2}$$

where $m_{\rm p}$ is the proton mass, G is the gravitational constant and $\sigma_{\rm T} \simeq 6.652 \times 10^{-25}$ cm^2 is the Thomson scattering cross-section for an electron. The Eddington ratio, defined as

$$\dot{m} = \frac{L_{\rm Bol}}{L_{\rm Edd}} = \frac{\dot{M}}{\dot{M}_{\rm Edd}} \tag{1.3}$$

is a useful measure for comparing BH accretion rates over a wide range of BH masses. The quantity in the numerator is the bolometric luminosity, $L_{\rm Bol}$, related to the UV monochromatic luminosity by $L_{\rm Bol} = A + B \log(\lambda L_\lambda)$, where A and B are constants that can be determined by analysing a sample of the objects of interest, AGNs in our case. In practice, the constant A is usually assumed to be zero. Examples of recent works available in the literature include Richards et al. (2006), Nemmen & Brotherton (2010), Runnoe et al. (2012) and Krawczyk et al. (2013). The bolometric correction accounts for the fact that, observationally, it is only possible to measure a monochromatic luminosity, L_λ, i.e., a fraction of the object's bolometric luminosity. The bolometric luminosity is defined as the integrated area under the full spectral energy distribution (SED).

As mentioned above, in the standard AGN model the BH is fed by a surrounding accretion disc . If it is assumed that this accretion disc is optically thick (e.g., Shakura & Sunyaev 1973), the resulting continuum spectrum of a "typical" AGN (i.e., with $M_{\rm BH} \approx 10^8$ M$_\odot$; $\dot{m} \approx 0.1$) would be thermal with a black-body temperature of $T \approx 2 \times 10^5$ K that peaks in the UV. Indeed, AGN are often observed to have a peak in their optical-UV continuum that is referred to as the "big blue bump".

The basics of the process of accretion are that matter spirals around a central mas-

sive body, losing angular momentum and radiating away part of its gravitational energy. Accretion is a fairly common powering process, present in many astrophysical environments, such as young stellar objects (YSOs), cataclysmic variables (CVs), X-ray binaries (XRBs), and gamma-ray bursts (GRBs).

Around the accretion disc there is thought to be an optically thin corona that is responsible, via Compton scattering of the photons produced at the accretion disc, for the power-law of the high-energy X-ray portion of the AGN spectra. These X-ray photons may also reflect off the torus and/or the accretion disc to produce an additional "reflection" component in the X-ray region (e.g., George & Fabian 1991).

1.1.2 Broad Line Region

The broad emission lines (BELs), generally blueshifted with respect to the systemic velocity and single-peaked, are one of the most significant spectroscopic features of AGNs. Although photoionization is well determined as the primary physical mechanism for their production, a detailed description of the region where the BELs originate is still an open question. Indeed, this region, the BLR, is spatially unresolved and its structure and dynamics remain unclear.

The BEL characteristics can in principle be explained by lines arising from either a nearly spherical distribution of discrete clouds, with no preferred velocity direction, or at the base of a wind from an accretion disc (e.g., Murray & Chiang 1997, hereafter MC97).

In the cloud scenario, the BLR is described as composed of numerous optically-thick clouds that, photoionised by the continuum-source emission, are the emitting entities responsible for the observed lines. However, this model leaves unsolved questions such as cloud formation and confinement.

In models of outflowing gas, two major accelerating mechanisms have been invoked: magnetohydrodynamic (MHD) driving (e.g., Emmering et al. 1992, hereafter EBS92), and radiative acceleration (e.g., Murray et al. 1995; Kurosawa & Proga 2009). In some of these wind models the flow is assumed to be continuous (e.g., Königl & Kartje 1994, MC97), while in others it contains embedded inhomogeneities or clouds (e.g., Bottorff et al. 1997). Both of these types of models have been successful in fitting AGN observations. The spectral line shapes can be used as a tool to study the kinematics and physics of plasmas in AGNs. We discuss the BLR and BEL production, particularly in the framework of wind models, in Chapter 2 and in Chapter 3 we analyse the MHD wind driving.

Reverberation mapping (RM) studies in several AGNs have shown that the BLR is a stratified structure (e.g., Peterson & Wandel 2000). In effect, it was found that, within the same AGN, the high-ionization lines are produced closer to the central source (i.e., have smaller $r_{\rm BLR}$) than the low-ionization lines.

1.1.3 Obscuring Structure

According to the unified model, surrounding the inner regions of an AGN is a geometrically thick and optically thick dusty region, with an inner radius set by the dust sublimation temperature. In the standard model, this region has a torus shape, however, the geometry of this structure is still the subject of debate. Alternative structures have been proposed in the literature, such as a clumpy torus, as oppose to a dense structure, (e.g., Hönig et al. 2006; Nenkova et al. 2008) or warped discs (e.g., Lawrence & Elvis 2010).

The dust in this region, heated by absorbing the photons from the accretion disc obscures the accretion disc along some LOS. This heated dust re-emits thermal radiation in the infrared (IR) regime, at wavelengths $\lambda \sim$ 1-1000 μm (e.g., Pier & Krolik 1992, Rowan-Robinson 1995, Polletta et al. 2000). Although the exact form of the IR emission for an AGN varies from source to source, the peak in this torus component seems to be around $\lambda \approx$ 20-50 μm and falls rapidly off at longer wavelengths (e.g., Schartmann et al. 2008, Mullaney et al. 2011, Alonso-Herrero et al. 2012).

1.2 Classification

AGN taxonomy, developed to classify the phenomenon on the basis of optical or radio emission characteristics is rather complex. According to their observed luminosity, spectral and morphological properties, AGN have been historically classified as Quasars

(most luminous sources), Seyfert galaxies, radio galaxies, blazars, etc. AGN unification posits that the diversity of AGN properties can be explained by a small number of physical (such as mass and luminosity) and observational parameters, such as viewing angle (e.g. Barthel 1989, Antonucci 1993, Urry & Padovani 1995).

AGN are divided into Type 1 and Type 2 AGN depending on the presence or absence, respectively, of broad (up to a few $\times 10^4$ km s^{-1}) emission lines in their optical/UV spectra, and into Radio Loud and Radio Quiet AGN on the basis of the radio emission power. In this work we are interested in the Type 1/Type 2 dichotomy, [1] that is explained invoking the anisotropic obscuration due to a structure (generally assumed to be a dusty torus) on scales of a few to tens of parsecs, of otherwise intrinsically the same type of objects (Antonucci 1993; Tran 1995; Nenkova et al. 2002). Because of its large physical scale, the NLR can not be (completely) obscured by the putative torus. Therefore, an AGN appears as a Type 2 source when our LOS to the BLR and the accretion disc is blocked by the obscuring structure and only narrow lines are present in the spectrum. As an example, a composite spectrum of these sources, adopted from Hainline et al. (2011) is shown in Figure 1.2.

[1] A recent review by Netzer (2015) explores critically this unification scheme.

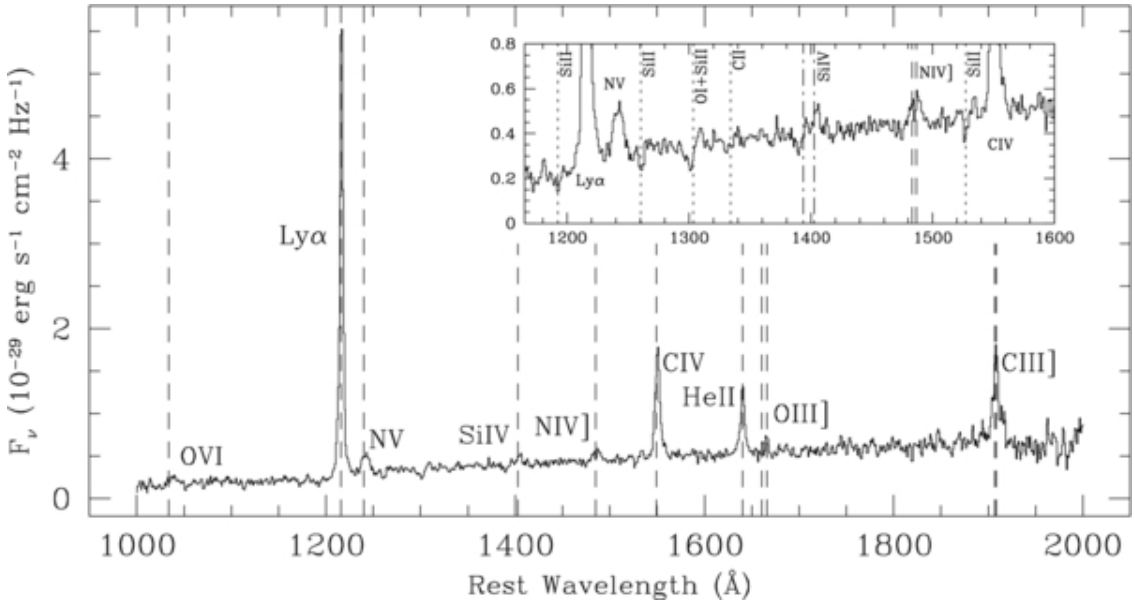

Figure 1.2: Composite rest-frame UV spectrum for 33 Type 2 AGNs at $z \sim 2-3$. Several emission lines are visible in the spectrum, such as N V λ 1240, C IV λ1549, and He II λ 1640, indicate by the dashed lines. The inset highlights some of the more prominent absorption features. Dotted lines are used to mark low-ionization absorption features, and dot-dashed lines indicate high-ionization absorption features. Adopted from Hainline et al. (2011).

A source is classified as Type 1 when the putative torus is not in the LOS, and therefore the emission from the central engine can reach the observer directly. The spectra of these sources exhibit both broad and narrow lines, among them, the transition studied in this work, the broad C IV emission line. An example of composite spectra of Type 1 objects, adopted from Richards et al. (2011), is shown in Figure 1.3.

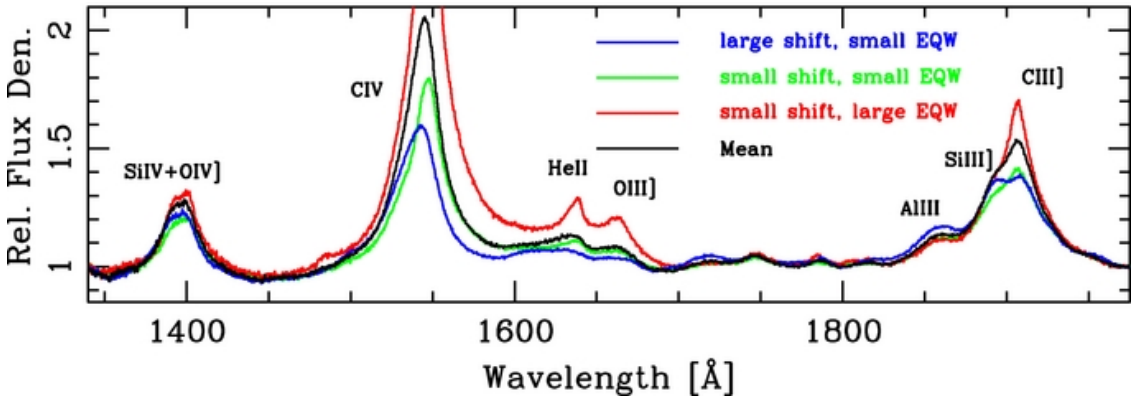

Figure 1.3: Composite rest-frame UV spectra of Type 1 AGNs, showing the region from Si IV to O IV] through C III] for four regions of C IV equivalent width-blueshift parameter space, each represented with a different colour. The equivalent width (EQW), a quantity originally defined for absorption lines, is a measure of the line strength and is not related to the actual width of the line. The equivalent width of a line is the width of the adjacent continuum that has the same area as covered by the absorption line, and is measured in length units (e.g. Å or nm). Mathematically, it is given by EQW $= \int \frac{F_c - F_\lambda}{F_\lambda} d\lambda$, where F_λ is the observed flux across the emission line at the wavelength λ, and $F_c(\lambda)$ is the continuum level at the position of the line. In the case of emission lines, the equivalent widths should be interpreted as a measure of the continuum range over which to integrate to obtain the same energy flux as is in the emission line.

Red indicates objects with large C IV EQW and small blueshift, blue indicates small EQW and large blueshift. Green indicates small blueshift and small EQW, while black shows the "mean" spectrum consisting of objects that are intermediate in both parameters. The spectra are normalized to unity at the ends of the plot region. Adopted from Richards et al. (2011).

Support for the unification scheme comes from the detection of broad lines in the polarized light in a significant fraction of Type 2 AGNs(e.g. Antonucci & Miller 1985; Miller & Goodrich 1990; Moran et al. 2000). On the other hand, the existence of a handful of "changing-look" sources (e.g. LaMassa et al. 2015 and references therein), that are classified differently at different epochs might represent a challenge for a purely geometric interpretation. An important parameter in this model is the opening angle of the torus, that in the standard unified model is assumed to be the same independent of the object. However, there is no reason for that and the torus-opening angle may depend on the AGN's intrinsic parameters.

We developed a model that results from combining an improved version of the MC97 disc wind model with the MHD driving of EBS92 and have applied the results to set constraints on the putative torus half-opening angle.

1.3 Thesis Outline

This work is organized as follows. In Chapter 2 we introduce some of the disc wind models in the literature, exploring the motivation of outflows versus cloud distribution for modelling the BLR. In Chapter 3 we discuss extensively the ideal, time independent magnetohydrodynamical approximation to plasmas that constitute the driving mechanism of the outflows in our model for the broad emission lines, that is described in Chapter 4. The rationale for modelling emission lines is that due to their ubiquity, some authors

(e.g. Richards 2012) regard emission lines as a more powerful tool for studying AGN than absorption lines, because the latter are only present in a fraction of the quasar population. Broad emission lines are produced close to the central engine and, therefore, carry important information on that region of the phenomenon. Therefore, accurate emission line models are important for studying AGN properties, such as black hole masses and accretion rates and put constraints on the unification paradigm. In Chapter 5 we apply our model to a fiducial set of black hole parameters and, using observational constraints on the dispersion of the line width, we derive constraints on the putative torus applicable to that particular case. We explore both homogeneous and clumpy torus and a warped disc as the obscuring structure. In Chapter 6 we extend the application of the model to a set of different combinations of black hole masses and ionising luminosities. The same observational constraints are used to study the influence of these mass-luminosity combinations to the putative torus, in both the homogeneous and clumpy cases. We present a summary and concluding remarks in Chapter 7. There are two appendices at the end. Appendix A provides a brief overview on the radiative transfer problem, aimed to introduce the physical significance of the source function. Appendix B shows the calculations pertaining to one of the warping modes introduced in Chapter 5.

Following the most extended use in the literature on MHD, we adopted the cgs Gaussian units system in this work. One of the advantages is that, in cgs system, both the electric ($\mathbf{E}$) and magnetic (B) fields have the same units.

2 Broad Line Region Models

Broad Emission Lines (BELs) are one characteristic feature of the spectra of Type 1 AGNs. Such lines are generally single-peaked and blueshifted with respect to the AGN rest frame. In Chapter 1 we discussed briefly the structure where these lines form, the BLR, and mentioned that currently there is no consensus on its nature while several models have been developed to explain it. Constraints from early spectroscopic observations of AGNs impose that the gas in the BLR has to be dense and with a small volume filling factor. Moreover, the structure is stratified, with higher ionization lines arising at smaller average radii than lower ionization lines (e.g., Peterson & Wandel 2000). The BEL characteristics can be explained by lines arising from either an approximately spherical distribution of discrete clouds, with no preferred velocity direction (e.g., Kaspi & Netzer 1999) or at the base of a wind from an accretion disc (e.g., Bottorff et al. 1997, Murray et al. 1995, Murray & Chiang 1997). Here we will discuss in more detail two popular scenarios.

In the cloud scenario, the BLR is described as composed of numerous optically-thick

clouds that, photoionised by the continuum-source emission, are the emitting entities responsible for the observed lines. Although this model can explain many observed spectral features, it also leaves several unsolved issues, such as the formation and confinement of the clouds (e.g., Netzer 1990). The two relevant time-scales for these clouds are the sound crossing time $t_{\rm sc}$ and the dynamical time $t_{\rm dyn}$. According to the models, the masses of individual BLR clouds are below their Jeans mass [2], therefore without a confinement mechanism such clouds will disintegrate on a time-scale $t_{\rm sc} \ll t_{\rm dyn}$, in which case they would need to be continuously produced. In addition, the number of clouds needed to reproduce the observed smoothness of BEL profiles (Arav et al. 1998, Dietrich et al. 1999) is very large. Furthermore, even if the clouds are confined, cloud-cloud collisions would destroy the clouds on a dynamical timescale (e.g. Mathews & Capriotti 1985), again requiring a high rate of cloud formation or injection.

One approach aimed at solving the discrete-cloud model difficulties was proposed by Emmering, Blandford & Shlosman (1992). In their model, the BLR is associated with disc-driven, hydromagnetic winds and the lines are formed by clouds which are confined by the magnetic pressure. Low-ionization line profiles, (e.g., Mg II), and high-ionization line profiles (e.g., C IV) are produced in the wind at different latitudes and radii. Within that framework, the estimated values of parameters such as ionizing flux,

[2]The Jeans mass is the minimum mass that can collapse under self-gravity. For a H cloud it is defined as $M_{\rm J} = \frac{\pi^{5/2}}{6} \left(\frac{kT}{Gm_{\rm p}}\right)^{3/2} \rho^{-1/2}$, where ρ is the mass density.

electron density, cloud filling factor, column density, and velocity are in agreement with values for these quantities inferred from observations. Emmering et al. (1992) consider emission models with and without electron scattering and attempt to construct a typical C IV emission profile. Different blueshifts and line asymmetries are obtained by varying model parameters.

Murray et al. (1995) and later Murray & Chiang (1997, 1998) proposed a wind model motivated by the similarities between broad emission lines in AGNs and other astrophysical objects, such as cataclysmic variables, protostars and X-ray binaries. They made the assumption that the outflow is continuous instead of being composed of discrete clouds and showed that such a continuous, optically thick, radiatively driven wind launched from just above the accretion disc can account for both the single-peaked nature of AGN emission lines and their blueshifts with respect to the AGN systemic redshift, although not for the magnitude of these shifts.

In an accelerating wind, the wind opacity in a given direction depends on the velocity gradient in that direction. The larger radial gradient of velocity in a radially accelerating wind means that the opacity seen by radially-emitted photons will be lower than the opacity seen by photons emitted in other directions. Thus, photons will tend to escape radially and the resultant emission lines are single-peaked. Figure 2.1, taken from Hall et al. (unpublished), illustrates the effect. The diagram shows the line emission region above part of a face-on disc with a rotating, radially accelerated wind. The black dot at

the centre is the BH and the black arrows represent the radial and azimuthal components of the velocity vectors of the line-emitting gas at four selected points, A, B, C and D. The four coloured arrows (offset slightly for clarity) at each of these points show the velocity gradient in the radial and azimuthal directions. The large velocity gradient in the radial direction means that line photons emitted radially are less likely to encounter an ion with small LOSt velocity and be absorbed, so line photons can escape in those directions (green arrows). In the azimuthal directions, the velocity gradients are smaller, so line photons typically travel only a short distance before encountering an ion with a small LOS velocity and being absorbed (red arrows). As a result, Observer 1 (off bottom) sees more line emission from points C and D than from points A and B, and observer 2 (off right) sees more line emission from points A and B than from points C and D.

It is worth mentioning that the wind scenario offers the explanation least conflicting with the existence of a small group of AGN that show double-peaked line profiles (generally, Balmer lines) in their spectra and with the fact that some, among them, fluctuate between a double- and a single-peaked profile (e.g., Flohic et al. 2012, Eracleous & Halpern 2003).

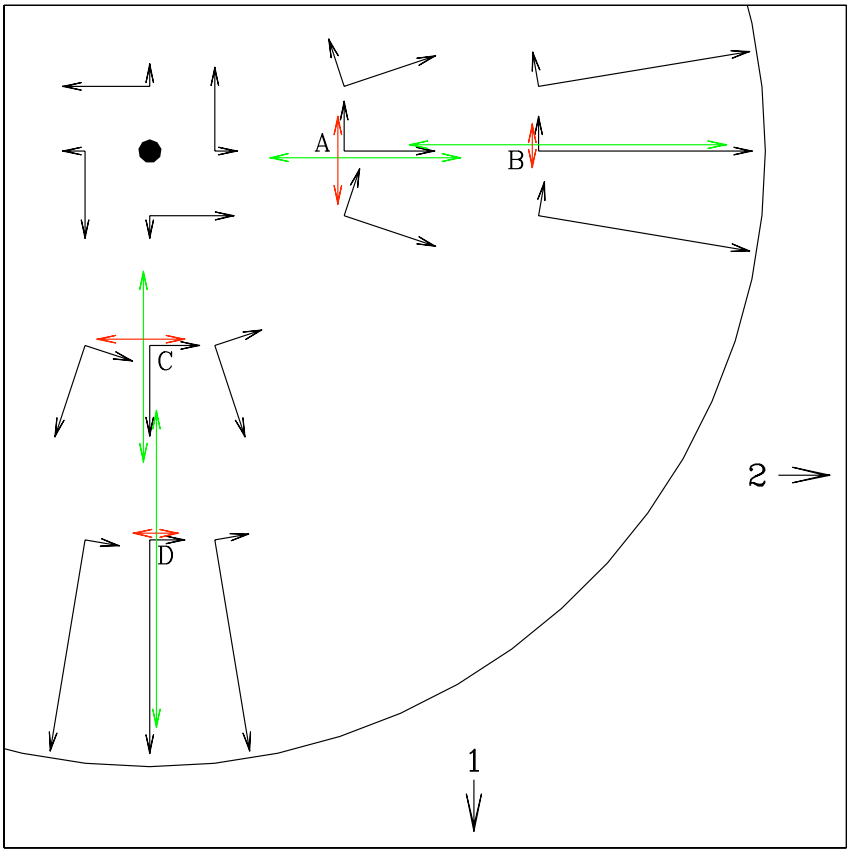

Figure 2.1: Diagram of the line emission region above part of a face-on disc with a rotating, radially accelerated wind. The black dot is the black hole. The black arrows show the radial and azimuthal velocity vectors of the line-emitting gas at selected points. At each point A, B, C and D, the four coloured arrows show the velocity gradient in the radial and azimuthal directions. Observer 1 sees more line emission from points C and D than from points A and B, and observer 2 sees more line emission from points A and B than from points C and D. Adopted from Hall et al. (unpublished).

In addition, the model high-velocity component of the wind naturally explains the existence of blueshifted broad absorption lines seen in an optically selected subset (15-20%) of the quasar population, known as broad absorption line (BAL) quasars.

In this chapter we discussed in some detail two alternative BLR descriptions, developed to explain the broad emission lines that characterize the spectra of type 1 AGN. From them, this work adopts the wind description of the structure and dynamics of the BLR. We combined an improved version of the Murray & Chiang (1997) and Emmering et al. (1992) models and analyse the dependence of the resulting emission line profiles on several parameters.

3 MHD

In this chapter we discuss the basics of ideal magnetohydrodynamics theory and then introduce its application to magnetically launched outflows from an accretion disc, relevant to the case of AGN. We further discuss the self-similar solutions, with an emphasis on the model of Blandford & Payne (1982) and on the related model of Emmmering et al. (1992), on which our final wind model is based.

In addition to he literature cited in the chapter, the following non-exhaustive list of books that have been consulted in writing this work can provide a broad view of the subject. "Lectures in Magnetohydrodynamics", (Schnack 2009), "The Physics of Fluids and Plasmas" (Choudhuri 1998), "MHD Flows in Compact Astrophysical Objects Accretion, Winds and Jets" (Beskin 2010), "Plasma Astrophysics, Part I" (Somov 2006).

3.1 Introduction

Magnetohydrodynamics (MHD) is the theoretical framework that describes the interaction between an electrically conducting fluid and magnetic fields. In fact, MHD is a

simplified treatment of the more complex subject of plasma physics. Despite being the simplest theory of plasma dynamics, MHD still consists of a set of partial differential equations (PDEs) and boundary conditions (BCs) that represent the interactions between the fluid and the electromagnetic (EM) field. When applicable, it represents an extraordinarily useful tool to study the processes in magnetized systems.

MHD is a macroscopic theory. The governing equations may, in principle, be derived from the Vlasov (sometimes referred to as collisionless Boltzmann) equation assuming space and time scales to be larger than all inherent length scales of the charged particles. Once the kinetic equations are solved the macroscopic variables can be derived by taking velocity-moments of the distribution functions. This approach has different levels of complexity in the approximations made, from multi-fluid, two-fluid theory and lastly, MHD that is a single-fluid theory.

A different approach is to obtain the MHD equations in a phenomenological way as the electromagnetic extension of the hydrodynamic equations of ordinary fluids, together with a series of simplifying assumptions. In the expression below, the subscripts "pl", "i" and "e", represent plasma, ion and electron, respectively.

- quasi-neutral fluid, that is, negligible charge density: $\rho_{\rm c} = e(Zn_{\rm i} - n_{\rm e}) \approx 0$, so $n_{\rm e} \approx Zn_{\rm i}$, where e is the electron charge, $n_{\rm i}$, $n_{\rm e}$ are the ion and electron number densities respectively.

- valid on time scales longer than the inverses of the plasma frequency and the relevant species cyclotron frequencies ($\tau \gg \omega_{\rm pl}^{-1}, \Omega_{\rm e}^{-1}, \Omega_{\rm i}^{-1}$), where $\omega_{\rm pl} = \left(\frac{4\pi e^2 n}{m_{\rm e}}\right)$ is the electron plasma frequency.

- if $\mathcal{U}$ is a characteristic fluid velocity and c is the speed of light in vacuum, the condition $\mathcal{U}^2/c^2 \ll 1$ must be satisfied.

- the above condition implies that the description will correspond to low-frequency and long-wavelength conditions. That corresponds to assuming an ordering of time scales. With $\mathcal{U} = \omega\mathcal{L}$, where $\mathcal{L}$ and ω are characteristic length-scale and frequency of the flow respectively, we have $\omega^2 \ll c^2/\mathcal{L}^2$, or $\tau = 1/\omega \gg \mathcal{L}/c = \tau_{\rm c}$. The characteristic time intervals for MHD are much longer than the time it takes a light wave to transit the macroscopic system.

- collisions are frequent enough for the particle distribution function to be Maxwellian with temperature $T = T_{\rm e} = T_{\rm i}$,

The validity of the fluid approach breaks down if $\tau \geqslant \tau_{\rm c}$ or if the mean free path between collisions, $\lambda_{\rm mfp} \approx c\tau$ is such that $\lambda_{\rm mfp} \geqslant \mathcal{L}$.

One notable characteristic of magnetized media is that, unlike unmagnetized fluids, they can support a shearing stress. That is, an electrically conducting fluid permeated by a magnetic field $\mathbf{B}$ can support the propagation of shear waves. This will be briefly discussed in Section 3.4.

In the astrophysical context, magnetic fields are ubiquitous (e.g., Silvers 2008), although their origin and evolution remain an open question and will not be discussed here. Many aspects of astrophysical magnetic fields problems are reviewed in Wielebinski & Beck (2005). Note that the presence of a magnetic field identifies a preferred direction in space, meaning that magnetized fluids are anisotropic media (e.g., Lorrain et al. 2006).

Magnetized winds have long been the subject of active research in relation to many astrophysical phenomena including, for example, the solar wind (Weber & Davis 1967), relativistic pulsar winds (Goldreich & Julian 1970), the collimation of relativistic jets near black holes (Phinney 1983), the structure of bipolar flows around YSOs (Pudritz & Norman 1986) and the confinement of clouds in BAL quasars (de Kool & Begelman 1995). Outflows are ubiquitous in astrophysical plasmas, observed in many environments ranging from stellar to galactic. Examples of such outflows are observed in young and evolved stars, and planetary nebula nuclei, symbiotic stars, black hole X-ray transients, low- and high-mass XRBs (e.g., Mirabel & Rodriguez 1996) and CVs (e.g., Livio 1997), AGNs (e.g Murray & Chiang 1997), and GRBs (e.g., Sari et al. 1999). These outflows manifest themselves as non-collimated winds (Parker 1958; Feldman et al. 1996), or as collimated jets (Blandford & Rees 1974; Biretta 1996).

In the remaining of this chapter we review the basic ideas and results developed to explain the dynamics of non-relativistic magnetically driven outflows and briefly discuss two popular MHD models. The chapter is organized as follows. Section 3.2 in-

troduces the non-relativistic MHD equations. Section 3.3 describes in more detail the time-independent case relevant to this work and introduces the set of quantities conserved along the flow that constrain its dynamics. Section 3.4 discusses the existence and location of the critical surfaces that separate different regimes along the flow and the associated characteristic speeds. Thus, sections 3.2 - 3.4 set the fundamentals and definitions that will be applied in the following sections. In section 3.5 we discuss the conditions under which a magnetized outflow can be launched. Self-similarity and its particularities within MHD problems are discussed in section 3.6. Section 3.7 presents the extensively applied Blandford & Payne (1982) radially self-similar solution and section 3.8 focuses on the model of Emmmering et al. (1992), which is the one that we adopted as the wind driver in our final model.

3.2 MHD Equations

The differential equations of non-relativistic MHD are the conservation laws derived from the coupling of Maxwell electromagnetic equations and general hydrodynamic

equations of fluid motion. Maxwell's equations describing the fields are:

$$\nabla \times \mathbf{B} = \frac{4\pi}{c}\mathbf{J} + \frac{1}{c}\frac{\partial \mathbf{E}}{\partial t}, \tag{3.1a}$$

$$\nabla \cdot \mathbf{B} = 0, \tag{3.1b}$$

$$\nabla \times \mathbf{E} = -\frac{1}{c}\frac{\partial \mathbf{B}}{\partial t}, \tag{3.1c}$$

$$\nabla \cdot \mathbf{E} = 4\pi\rho_{\mathrm{e}}, \tag{3.1d}$$

where ρ_{e} and $\mathbf{J}$ are the total charge density and the total electric current vector respectively.

We recall here that there are two formulations of fluid dynamics, Eulerian and Lagrangian. In the Eulerian description, the system is viewed from a fixed coordinate system and each fluid property is described as a function of $(\mathbf{r}, t)$. The Eulerian time derivative $\frac{\partial}{\partial t}$ describes how variables change in time, evaluated at the fixed position. This description is particularly useful in the case of steady flows, i.e. when $\frac{\partial}{\partial t} = 0$.

In the Lagrangian approach, on the other hand, the system evolution is described from the viewpoint of particles moving with the fluid. The Lagrangian time derivative (also known as material, substantial, or particle derivative) is then given by:

$$\frac{D}{Dt} = \frac{\partial}{\partial t} + \mathbf{v} \cdot \nabla, \tag{3.2}$$

where the second term, known as convective (or advective) derivative, is due to the motion of the fluid element.

In non-relativistic MHD the relevant field is the magnetic field $\mathbf{B}$. Non-relativistic means that the flow velocity satisfies $v \approx \mathcal{L}/\tau \ll c$ everywhere. Indeed, it can be shown by means of a scale analysis that in this regime $|\mathbf{E}| \ll |\mathbf{B}|$. In effect, τ^{-1} and $\mathcal{L}^{-1}$ can be used to obtain (crude) approximations to the temporal and spatial derivatives, using the following simple rules

$$\frac{\partial}{\partial t} \to \frac{1}{\tau}, \qquad \nabla \to \frac{1}{\mathcal{L}}.$$

Consider Equation (3.1c). By applying the approximations suggested above to its magnitude form, the relation becomes

$$\frac{E}{\mathcal{L}} \approx \frac{1}{c}\frac{B}{\tau}. \tag{3.3}$$

Rearranging the factors clearly shows

$$\frac{E}{B} \approx \frac{1}{c}\frac{\mathcal{L}}{\tau} \sim \frac{\mathcal{U}}{c} \ll 1. \tag{3.4}$$

Proceeding in an analogous way with the right-hand side of Equation (3.1a) it is also straightforward to show that its second term, known as the displacement current, may be ignored in this low-frequency regime.

$$\frac{\left|(4\pi/c)\mathbf{J} + (1/c)\left(\partial\mathbf{E}/\partial t\right)\right|}{|\nabla \times \mathbf{B}|} \leqslant \frac{\left|(4\pi/c)\mathbf{J}\right| + \left|(1/c)\left(\partial\mathbf{E}/\partial t\right)\right|}{|\nabla \times \mathbf{B}|} \approx \frac{(4\pi/c)J + (1/c)(E/\tau)}{B/\mathcal{L}}$$

Hence, using the approximation obtained in Eq (3.4):

$$\frac{\left|(4\pi/c)\mathbf{J} + (1/c)\left(\partial\mathbf{E}/\partial t\right)\right|}{|\nabla \times \mathbf{B}|} \lessapprox \frac{4\pi}{c} J\frac{\mathcal{L}}{B} + \frac{1}{c^2}\left(\frac{\mathcal{L}}{\tau}\right)^2.$$

The last term is proportional to $(v/c)^2$ and can be neglected and Ampère's law, Eq (3.1a) takes the simple form

$$\nabla \times \mathbf{B} = \frac{4\pi}{c}\mathbf{J}. \tag{3.5}$$

The Lorentz force is given by $\mathbf{F}_{\mathrm{L}} = \rho_{\mathrm{e}}\mathbf{E} + \frac{\mathbf{J}\times\mathbf{B}}{c}$. Taking into account the quasi-neutrality assumption, the expression then simplifies to

$$\mathbf{F}_{\mathrm{L}} \approx \frac{\mathbf{J}\times\mathbf{B}}{c} = \frac{1}{4\pi}\left(\nabla \times \mathbf{B}\right) \times \mathbf{B}, \tag{3.6}$$

where the second expression is obtained by replacing $\mathbf{J}$ by Equation (3.1a). To have a complete description of the fluid structure, these equations have to be completed with Ohm's equation and an equation of state, often adopted to be of polytropic form. In this regime, Ohm's law takes the form:

$$\mathbf{J} = \sigma_{\mathrm{e}}\left(\mathbf{E} + \frac{\mathbf{v}}{c} \times \mathbf{B}\right), \tag{3.7}$$

where σ_{e} is the electric conductivity of the plasma.

Combining Equations (3.5), (3.1c) and (3.7) gives the so called induction equation for the magnetic field:

$$\frac{\partial \mathbf{B}}{\partial t} = \nabla \times (\mathbf{v} \times \mathbf{B}) + \frac{c^2}{4\pi\sigma_{\mathrm{e}}}\nabla^2\mathbf{B}, \tag{3.8}$$

where the vector identity $\nabla \times (\nabla \times \mathbf{a}) = \nabla\left(\nabla \cdot \mathbf{a}\right) - \nabla^2\mathbf{a}$ has been applied.

The quantity $\nu_{\mathrm{m}} \equiv c^2/4\pi\sigma_{\mathrm{e}}$ is the magnetic-diffusion (or magnetic-viscosity) coefficient, and has dimensions of length^2/time. The first term on the right-hand side of the

induction equation corresponds to the advection of the magnetic field with the flow, while the second term corresponds to its diffusion. A further simplification is to treat the fluid as (near) perfectly conducting, i.e., ignoring resistive effects, an approximation known as ideal MHD. Then the diffusive term in Equation (3.8) can be neglected compared to the convective term. The relative importance of advection and diffusion is measured by the magnetic Reynolds number:

$$\mathrm{Re_m} = \frac{\mathcal{L}\mathcal{U}}{\nu_\mathrm{m}}. \tag{3.9}$$

An equivalent way to define the ideal MHD regime is by defining a characteristic magnetic diffusive timescale, equal to $\mathcal{L}^2/\nu_\mathrm{m}$, called the Ohmic timescale. In many contexts the Ohmic timescale is very much longer than other timescales of interest and it is possible to ignore the diffusive term in the inductive equation. The simplified form of this equation is, then,

$$\frac{\partial \mathbf{B}}{\partial t} = \nabla \times (\mathbf{v} \times \mathbf{B}). \tag{3.10}$$

Two more equations, for mass conservation and motion, are needed to complete the set of equations describing the MHD problem.

$$\frac{\partial \rho}{\partial t} + \nabla \cdot (\rho \mathbf{v}) = 0 \tag{3.11}$$

$$\rho \frac{\partial \mathbf{v}}{\partial t} + \rho(\mathbf{v} \cdot \nabla)\mathbf{v} = -\nabla p - \rho \nabla \Phi_\mathrm{g} + \frac{1}{4\pi}(\nabla \times \mathbf{B}) \times \mathbf{B}, \tag{3.12}$$

where ρ is the mass density, p is the thermal pressure and Φ_g is the gravitational potential. Equation (3.11), known as continuity equation, is written in conservative form. Equation

(3.12) is Newton's second law valid for fluids, that describes the fluid motion. This force equation (also referred to in the literature as momentum or Euler equation) can not be written in conservative form in the presence of an external gravitational potential, (e.g., Goedbloed & Poedts 2004).

An important result, known as Alfvén's theorem (Alfvén 1943), states that the magnetic flux through a co-moving surface remains constant [3] and the field lines move with the fluid. Because of that, the theorem is often stated as that the flux is frozen in to the fluid. To prove this result (e.g., Chiuderi & Velli 2012), consider a closed curve $\mathcal{C}$ within the fluid, co-moving with it and a surface A bounded by $\mathcal{C}$. Define the magnetic flux through A as

$$\Psi = \int_{\mathrm{A}} \mathbf{B} \cdot d\mathbf{A}. \tag{3.13}$$

The change of Ψ through that surface as $\mathcal{C}$ moves with the fluid consists of two parts:

$$\frac{D\Psi}{Dt} = \int_{\mathrm{A}} \frac{\partial \mathbf{B}}{\partial t} \cdot d\mathbf{A} + \oint_{\mathcal{C}} \mathbf{B} \cdot (\mathbf{v} \times d\boldsymbol{\ell}), \tag{3.14}$$

where $\boldsymbol{\ell}$ is a line element on the curve $\mathcal{C}$. The first term comes from the rate of change of flux through the surface, as if it were fixed in space, and the second comes from the motion of the surface and curve with the fluid velocity $\mathbf{v}$. Substituting Equation (3.10) into this equation and using Stokes' theorem, the first term becomes $\oint_{\mathcal{C}} \mathbf{v} \times \mathbf{B} \cdot d\boldsymbol{\ell}$. Using

[3] Some authors, e.g., Lorrain et al. (2006) adopt a clear distinction between *constant*, reserved for quantities that do not vary with time, and *uniform* that refers to quantities whose value within a given region is independent of the position. We have here followed the most common approach in the literature, and applied, in general, the qualification of "constant" for both cases.

the vector identity $(\mathbf{a} \times \mathbf{b}) \cdot \mathbf{c} = \mathbf{a} \cdot (\mathbf{b} \times \mathbf{c})$ the two terms cancel, showing that the flux through the co-moving surface is constant in time.

Another way to show this result (e.g., Goedbloed & Poedts 2004, Fleishman & Toptygin 2013) is to use the identity $\nabla \times (\mathbf{a} \times \mathbf{b}) = (\mathbf{b} \cdot \nabla)\mathbf{a} - (\mathbf{a} \cdot \nabla)\mathbf{b} + (\nabla \cdot \mathbf{b})\mathbf{a} - (\nabla \cdot \mathbf{a})\mathbf{b}$ to write the induction equation in the form

$$\frac{D\mathbf{B}}{Dt} = (\mathbf{B} \cdot \nabla)\mathbf{v} - \mathbf{B}(\nabla \cdot \mathbf{v}), \tag{3.15}$$

and use the equation of mass conservation in Lagrangian form, $D\rho/Dt + \rho\nabla \cdot \mathbf{v} = 0$, to obtain

$$\frac{D}{Dt}\left(\frac{\mathbf{B}}{\rho}\right) = \left(\frac{\mathbf{B}}{\rho} \cdot \nabla\right)\mathbf{v}. \tag{3.16}$$

This expression describes how the ratio of magnetic flux to mass density (i.e., the quantity $\mathbf{B}/\rho$) changes according to the variation of the fluid velocity along a field line. It can be shown that the equation satisfied by a material line element $\delta\mathbf{r}$ has the same form ($\frac{D}{Dt}\delta\mathbf{r} = (\delta\mathbf{r} \cdot \nabla)\,\mathbf{v}$). The physical interpretation is, as mentioned, that (in ideal MHD) the magnetic field lines are frozen in the fluid flow and thus advected by it in the same way as a fluid line (Meier 2012). That implies that reconnection is not possible in the ideal MHD regime.

Blackman (2013), and also Goedbloed & Poedts (2004), demonstrate the frozen-in result by direct differentiation of the flux integral, separately computing $D\mathbf{B}/dt$ and $Dd\mathbf{S}/dt$ by considering the infinitesimal evolution of these quantities.

3.3 Ideal stationary MHD outflow structure

The complete set of MHD equations consists of conservation laws of mass and momentum, the solenoidal nature of the magnetic field and its time evolution. The magnetic field is coupled to the fluid by the Lorentz force, Equation (3.6) in the equation of motion Equation (3.12). In total, the MHD equations thus consist of two vector and two scalar partial differential equations (or eight scalar equations) that are to be solved simultaneously.

However, many astrophysical problems can be treated as stationary and axisymmetric (e.g., pulsars; rotating stars, accretion discs and black holes; winds and jets). These assumptions lead to a single equation for the two-dimensional distribution of electromagnetic fields in the (r, z) plane that is the generalization of an equation independently derived by Grad, Schlüter and Shafranov to study equilibrium behaviour of a tokamak plasma (Grad & Rubin 1958, Lust & Schlüter 1957, Shafranov 1958, 1960). The Grad-Schlüter-Shafranov (GSS hereafter, also referred to as transfield) equation is a two-dimensional, non-linear, partial differential equation that has been intensively utilized in MHD flow studies both for non-relativistic and relativistic outflows in different environments (Beskin & Kuznetsova 2000 and references therein) and is one of the two basic equations of the problem, together with Bernoulli's (e.g.,, Rosso & Pelletier 1994).

In what follows, we will review the theory that describes non-relativistic, steady state

(i.e., when $\partial/\partial t = 0$) MHD winds. For clarity, all the relevant expressions are written together below:

$$\nabla \cdot (\rho \mathbf{v}) = 0 \tag{3.17a}$$

$$\rho(\mathbf{v} \cdot \nabla)\mathbf{v} = -\nabla p - \rho \nabla \Phi_{\rm g} + \frac{1}{4\pi}(\nabla \times \mathbf{B}) \times \mathbf{B} \tag{3.17b}$$

$$\nabla \times (\mathbf{v} \times \mathbf{B}) = 0 \tag{3.17c}$$

$$\nabla \cdot \mathbf{B} = 0, \tag{3.17d}$$

$$\mathbf{E} + \frac{\mathbf{v}}{c} \times \mathbf{B} = 0. \tag{3.17e}$$

As it will be shown below, in steady state the solutions have a number of conserved quantities along each magnetic field line (e.g., Mestel 1968), that impose constraints to the flow dynamics. Figure 3.1, adopted from Kudoh & Shibata (1997), shows an schematic representation of a magnetic outflow emerging from an accretion disc. For winds from an accretion disc, due to the azimuthal symmetry of the problem, it is natural and more convenient to work in a cylindrical co-ordinate system. Due to this axisymmetry, the vector fields can be separated into their poloidal and azimuthal components: $\mathbf{v} = \mathbf{v}_p + \mathbf{v}_\phi$ and $\mathbf{B} = \mathbf{B}_p + \mathbf{B}_\phi$. As it is known, the solenoidal condition Equation (3.17d) implies that the magnetic field can be written as the curl of a vector potential $\mathbf{A}$. Com-

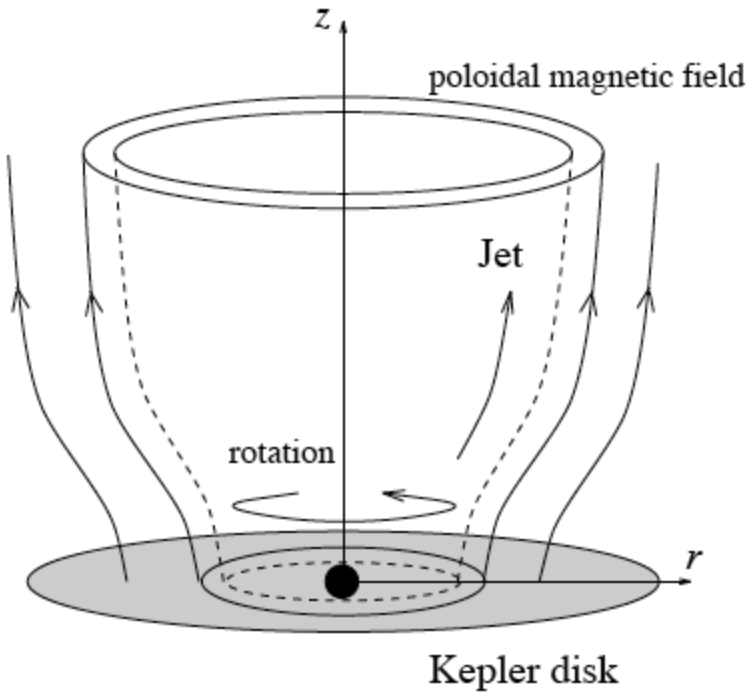

Figure 3.1: Schematic view of the magnetically driven outflow from an accretion disc. The disc rotational energy is converted to the Poynting flux, which accelerates the jet along the poloidal field lines. Adopted from Kudoh & Shibata (1997).

bining this with the axisymmetry assumption implies that

$$\mathbf{B} = \nabla \times (A_\phi \, \mathbf{e}_\phi) + \left(\frac{\partial A_r}{\partial z} - \frac{\partial A_z}{\partial r} \right) \mathbf{e}_\phi \, , \tag{3.18}$$

where $\mathbf{e}_\phi$ is a unit vector in the azimuthal direction. Then, writing the flux function introduced in Equation (3.13) as

$$\Psi(r, z) = - \, r \, A_\phi, \tag{3.19}$$

the poloidal component of the magnetic field can be written as

$$\mathbf{B}_p = \frac{1}{r}\nabla\Psi \times \mathbf{e}_\phi. \tag{3.20}$$

The physical interpretation of Equation (3.20) is that the magnetic flux through a circular cross section of radius r in a plane perpendicular to the axis at altitude z is $2\pi\Psi(r,z)$ (e.g., Pelletier & Pudritz 1992). The magnetic surfaces are generated by rotating the poloidal projection of field lines around the z-axis, such that $\Psi(r,z) = \text{const.}$ and satisfy

$$\mathbf{B}\cdot\nabla\Psi(r,z) = \mathbf{B}_\mathrm{p}\cdot\nabla\Psi(r,z) = 0. \tag{3.21}$$

The induction Equation (3.17c) implies that

$$\mathbf{v}\times\mathbf{B} = \nabla\varkappa \tag{3.22}$$

for some function $\varkappa$. Note that since $\mathbf{E} = -(\mathbf{v}/c)\times\mathbf{B}$, then $\mathbf{E} = -\nabla\varkappa/c$; the function $\varkappa$ is therefore the scalar potential of electromagnetism. In addition, the axisymmetric condition, $\partial_\phi\varkappa = 0$, implies $E_\phi = 0$. Therefore,

$$E_\phi\,\mathbf{e}_\phi = \mathbf{v}_\mathrm{p}\times\mathbf{B}_\mathrm{p} = 0, \tag{3.23}$$

which means that the poloidal velocity is parallel to the poloidal magnetic field. This condition, together with the conservation of mass and magnetic flux implies

$$\mathbf{v}_\mathrm{p} = \frac{k}{4\pi\,\rho}\,\mathbf{B}_\mathrm{p}, \tag{3.24}$$

for some scalar function $k(\Psi)$, that is constant on each magnetic surface and that can be interpreted as the mass load of the outflow. The role of this function is critical in jet dynamics and it controls the rotation, collimation, and angular momentum extraction of the outflow (Pudritz et al. 2012). Physical insight can be gained by expressing this function in terms of the wind mass-loss rate per unit magnetic flux (e.g., Pelletier & Pudritz 1992).

$$\frac{k}{4\pi} = \frac{\rho\, v_{\rm p}}{B_{\rm p}} = \frac{d\dot{M}_{\rm w}}{d\Psi}, \tag{3.25}$$

where $d\dot{M}_{\rm w} = \rho\, v_{\rm p}\, dA$ is the wind mass flow rate through a circle of cross section area $dA = 2\pi\, r\, dr$ between radii r and $r + dr$, $d\Psi = B_{\rm p}\, dA$ is the magnetic flux across the same annulus.

A relation between the toroidal components of the velocity and magnetic fields can be obtained by analysing the poloidal component of Equation (3.22) (note that $\nabla\varkappa|_{\rm p} = (\mathbf{v}\times\mathbf{B})_{\rm p} = \mathbf{v}\times\mathbf{B} = \nabla\varkappa$). Thus,

$$\mathbf{v}\times\mathbf{B} = \mathbf{v}_{\rm p}\times B_\phi\,\mathbf{e}_\phi + v_\phi\,\mathbf{e}_\phi\times\mathbf{B}_{\rm p}. \tag{3.26}$$

Replacing $\mathbf{B}_{\rm p}$ from Equation (3.20) and $\mathbf{v}_{\rm p}$ from Equation (3.24) and using the axisymmetric condition, the above equation can be rearranged to obtain

$$\mathbf{v}\times\mathbf{B} = \frac{1}{r}\left(v_\phi - \frac{k}{4\pi\rho}B_\phi\right)\nabla\Psi. \tag{3.27}$$

According to the induction equation, the curl of the above expression is zero. Thus,

$$0 = \nabla\left(\frac{1}{r}\left(v_\phi - \frac{k}{4\pi\rho}B_\phi\right)\right)\times\nabla\Psi, \tag{3.28}$$

where the $\nabla \times (f\mathbf{a}) = (\nabla f) \times \mathbf{a} + f\,(\nabla \times \mathbf{a})$ and $\nabla \times \nabla f = 0$ vector identities, valid for arbitrary vector $\mathbf{a}$ and scalar f functions, have been applied. Therefore, the quantity $\frac{1}{r}\left(v_\phi - kB_\phi\right)$ is constant on magnetic surfaces:

$$\frac{1}{r}\left(v_\phi - \frac{k}{4\pi\rho}B_\phi\right) = \Omega(\Psi). \tag{3.29}$$

Physically, $\Omega = \Omega(\Psi)$ can be interpreted as the angular velocity of the magnetic surface, different for each of them. This result, known as Ferraro's isorotation law (Ferraro 1937), is a necessary condition for a stationary equilibrium. From Equation (3.29), the toroidal component of the velocity is given by:

$$v_\phi = r\Omega(\Psi) + \frac{k}{4\pi\rho}B_\phi. \tag{3.30}$$

As stressed by Heyvaerts (1996), $\Omega(\Psi)$ is not the angular velocity of the fluid, which should be defined as v_ϕ/r and, according to Equation (3.30), $v_\phi/r \neq \Omega(\Psi)$. Close to the wind source, where the density may be very large, and the field-aligned velocity is very small, it could be $v_\phi/r \approx \Omega$. An alternative way to express Ferraro's isorotation is

$$(\mathbf{B}\cdot\nabla)\,\Omega = 0.$$

Combining Eqs (3.24) and (3.30), the complete velocity field may be written in the form

$$\mathbf{v} = r\,\Omega\,\mathbf{e}_\phi + \frac{k}{4\pi\rho}\mathbf{B}, \tag{3.31}$$

i.e., the total velocity is parallel to the total magnetic field in a reference frame rotating with angular velocity Ω. Since Ω depends only on Ψ, this indicates that this rotation is

like a solid body rotation of the magnetic surface. This is often interpreted as the fluid being constrained to move along the field line like a bead on a rotating wire.

The azimuthal component of the Euler equation (3.17b) is

$$\rho\left((\mathbf{v}_{\rm p}\cdot\nabla)v_\phi+\frac{v_{\rm r}v_\phi}{r}\right)=\frac{1}{4\pi}\left((\mathbf{B}_{\rm p}\cdot\nabla)B_\phi+\frac{B_{\rm r}v_\phi}{r}\right), \tag{3.32}$$

where the vector identity $\mathbf{a}\times(\nabla\times\mathbf{b})=(\nabla\mathbf{b})\cdot\mathbf{a}-(\mathbf{a}\cdot\nabla)$ has been applied, together with the axisymmetric condition. This can be written as

$$\frac{\rho}{r}\,\mathbf{v}_{\rm p}\cdot\nabla\left(rv_\phi\right)=\frac{1}{4\pi r}\,\mathbf{B}_{\rm p}\cdot\nabla\left(rB_\phi\right) \tag{3.33}$$

and, finally, using the relation Equation (3.24), as

$$\mathbf{B}_{\rm p}\cdot\nabla\left(r\,v_\phi-r\,\frac{B_\phi}{k}\right)=0. \tag{3.34}$$

Then, the quantity in brackets,

$$r\,v_\phi-r\,\frac{B_\phi}{k}=l(\Psi) \tag{3.35}$$

is conserved along poloidal field lines and is only a function of Ψ, and represents the specific angular momentum in the outflow. The first term is the matter contribution and the second term is the fraction of the angular momentum removed by the magnetic field. Note that the mass load k controls the relative proportion of total angular momentum that is carried by matter and the field (Pudritz et al. 2012).

An important quantity defined for magnetized fluids is the so-called Alfvén Mach

number, $\mathcal{M}$. The square of this quantity is defined as

$$m = \mathcal{M}^2 \equiv \frac{v_{\rm p}^2}{v_{\rm Ap}^2}, \tag{3.36}$$

where $v_{\rm Ap}$ is the poloidal component of the Alfvén velocity

$$\mathbf{v}_{\rm A} = \frac{\mathbf{B}}{\sqrt{4\pi\,\rho}}, \tag{3.37}$$

which is the characteristic velocity of the propagation of magnetic signals in an MHD fluid.

The Alfvén radius $r_{\rm A}$ is the point on each poloidal field line where $m = 1$; the loci of all $r_{\rm A}$ define the Alfvén surface. The subscript "A" refers, hereafter, to quantities evaluated at the Alfvén point. From the definition of m, and using the expressions (3.24) and (3.37), it is easy to see that

$$m = \frac{4\pi\rho\, v_{\rm p}^2}{B_{\rm p}^2} = \frac{k^2}{4\pi\rho}, \tag{3.38}$$

such that $m \propto \rho^{-1}$ on each magnetic surface. From Equation (3.38) it also follows that the mass density at the Alfvén radius on each poloidal field line is $\rho_{\rm A} = k^2/4\pi$.

Solving for v_ϕ and B_ϕ between Equations (3.30) and (3.35) and combining with Equation (3.38), the toroidal components of the outflow velocity and the magnetic fields may be written in terms of the Alfvén number and conserved quantities,

$$r\, v_\phi = \left(\frac{m\, l - r^2\Omega}{m-1}\right), \tag{3.39}$$

$$r B_\phi = k\left(\frac{l - r^2\Omega}{m-1}\right). \tag{3.40}$$

The numerators of both above expressions must vanish at $r = r_{\rm A}$ in order to avoid unphysical solutions there. This fixes the value of the angular momentum on each field line,

$$l(\Psi) = r_{\rm A}^2\,\Omega(\Psi) = \left(\frac{r_{\rm A}}{r_0}\right)^2 l_0, \tag{3.41}$$

where $l_0 = v_{\rm K,0} r_0 = \Omega_0 r_0^2$ is the specific angular momentum on a Keplerian disc. For a field line starting at a point $r = r_0$ (its footpoint) on the disc, the ratio $r_{\rm A}(r_0)/r_0$ can be interpreted as a magnetic lever arm, that brakes down the disc (Ferreira 2006). The larger the ratio $r_{\rm A}/r_0$, the larger the magnetic torque acting on the disc at the radius r_0 (Pelletier et al. 2012). In other words, if the Alfvén radius is large compared to the footpoint radius, removal of angular momentum is highly efficient.

The toroidal components in Equations (3.39) and (3.40) can be written in terms of quantities at the Alfvén radius

$$v_\phi = \Omega r\,\frac{1-\rho_{\rm A} r_{\rm A}^2/\rho r^2}{1-\rho_{\rm A}/\rho}, \tag{3.42}$$

$$B_\phi = \Omega r^2\,\sqrt{4\pi\rho_{\rm A}}\,\frac{1-r_{\rm A}^2/r^2}{1-\rho_{\rm A}/\rho}. \tag{3.43}$$

There is a change in the behaviour of the solutions when the Alfvénic surface is crossed. For $m \ll 1$ ($r \ll r_{\rm A}$), $v_\phi \approx \Omega r$, i.e., the fluid is in uniform rotation, corotating with the magnetic surface. Therefore Ω can be identified as the angular velocity $v_\phi/r = \Omega_0$ of the footpoint $r = r_0$ of the magnetic field line at the source of the outflow. It will then accelerate smoothly through an Alfvén surface and become super-Alfvénic

($m > 1$). If mass is lost at a rate $\dot{M}_{\rm w}$ in the outflow, angular momentum is lost at a rate $\dot{M}l = \dot{M}r_{\rm A}^2\Omega_0$. The asymptotic behaviour of the ratio

$$\frac{B_\phi}{B_{\rm p}} = \frac{v_\phi - \Omega r}{v_{\rm p}}, \tag{3.44}$$

obtained from Equations (3.25) and (3.31), shows that in this regime the magnetic field is dominated by the poloidal component, $B_\phi \ll B_{\rm p}$.

For $m \gg 1$ ($r \gg r_{\rm A}$), i.e., far from the Alfvén surface, $v_\phi \approx 0$, that is, the velocity is predominantly poloidal in this region, while the magnetic field becomes dominantly toroidal. The density, on the other hand, decreases, $\rho < \rho_{\rm A}$, but the quantities ρr^2 and $v_{\rm p}$ remain finite (Heyvaerts & Norman 1989). Thus, from Equations (3.24) and (3.37), (Ustyugova et al. 1999)

$$v_{\rm p}^2 = \left(\frac{\rho_{\rm A}}{\rho}\right) v_{\rm Ap}^2 > v_{\rm Ap}^2. \tag{3.45}$$

A generalized version of Bernoulli's theorem, i.e., the equation for the specific energy, may be derived by projecting the equation of motion, Equation (3.17b), on the poloidal direction, yielding

$$e(\Psi) = \frac{1}{2}v^2 + h + \Phi - \frac{r\Omega B_\phi}{4\pi k}. \tag{3.46}$$

This equation expresses the conservation of energy per unit mass along a poloidal field line, i.e., the conversion of magnetic energy and enthalpy into kinetic energy. The function $h = \epsilon + p/\rho$ is the specific enthalpy of the plasma. For a polytropic equation of

state $p = K\rho^{\gamma}$, where $K(\Psi)$ is constant on magnetic surfaces, with $\gamma \neq 1$, it is given by $h = \gamma\, c_{\rm s}^2/(\gamma - 1)$, where $c_{\rm s} = (\gamma p/\rho)^{1/2}$ is the speed of sound in the medium.

The last term on the right-hand side of Equation (3.46) is related to the poloidal component of electromagnetic energy flux (the Poynting vector flux). In effect, the Poynting vector is defined by:

$$\mathbf{s} = \frac{c}{4\pi}\,(\mathbf{E}\times\mathbf{B}) = -\frac{1}{4\pi}\,(\mathbf{v}\times\mathbf{B})\times\mathbf{B}, \tag{3.47}$$

where the last expression results from replacing $\mathbf{E}$ from Equation (3.17e). Then, replacing $\mathbf{v}$ by Eq (3.31), it follows that

$$\mathbf{s} = -\frac{1}{4\pi}\left[\left(r\Omega\mathbf{e}_{\phi} + k\mathbf{B}\right)\times\mathbf{B}\right]\times\mathbf{B} = \frac{r\Omega}{4\pi}\left(\mathbf{B}_{\rm p}^2\mathbf{e}_{\phi} - B_{\phi}\mathbf{B}_{\rm p}\right). \tag{3.48}$$

Thus, the flux of electromagnetic energy through a surface element perpendicular to the poloidal field, $d\mathbf{S} = dS(\mathbf{B}_{\rm p}/B_{\rm p})$, is

$$dw = \mathbf{s}\cdot dS\left(\frac{\mathbf{B}_{\rm p}}{B_{\rm p}}\right) = -dS\,\frac{r\Omega B_{\phi}B_{\rm p}}{4\pi}. \tag{3.49}$$

Dividing this by the mass flux dm through the same surface element gives an expression for the equivalent specific energy of the electromagnetic energy flux. The mass element is evaluated from Equation (3.25)

$$\frac{dw}{dm} = -\frac{r\Omega B_{\phi}B_{\rm p}}{4\pi\rho B_{\rm p}} = -\frac{r\Omega B_{\phi}}{4\pi k}, \tag{3.50}$$

that is the last term in Equation (3.46), as mentioned above.

The Grad-Schlüter-Shafranov or transfield equation mentioned above can be obtained by taking the dot product of the poloidal component of the equation of motion (3.17b) with $\nabla\Psi$. The resulting expression is a differential equation for the flux function $\Psi(r,z)$ in terms of the mass density and conserved quantities. Following Ferreira (2002), the GSS equation valid for an adiabatic wind can be written as:

$$\nabla\cdot\left[(m-1)\,\frac{\nabla\Psi}{4\pi r^2}\right]-\frac{B_\phi^2+mB_{\rm p}^2}{4\pi}\,\frac{d\ln k}{d\Psi}= \rho\left[\frac{de}{d\Psi}-\Omega\frac{d\Omega_{\rm m}r_{\rm A}^2}{d\Psi}+(\Omega r^2-\Omega_{\rm m}r_{\rm A}^2)\frac{d\Omega}{d\Psi}-\frac{c_{\rm s}^2}{\gamma(\gamma-1)}\,\frac{d\ln K}{d\Psi}\right], \tag{3.51}$$

where $\Omega r_{\rm m}=v_\phi/r$. Note that in the literature can be found several alternative ways to write it.

The Bernoulli and the GSS equations (Equations (3.46) and (3.51) respectively) form a system of two coupled, non-linear differential equations. This is a complicated system that can not be analytically solved in the general case but only under some simplifying assumptions such as self-similarity (e.g., Blandford & Payne 1982; Li et al. 1992; Vlahakis & Tsinganos 1998), or in some asymptotic regime (e.g., Begelman & Li 1994; Heyvaerts & Norman 2003a; Lyubarsky 2009). A different approach is to assume *a priori* that the functional form of the poloidal magnetic field is known. For instance, Weber & Davis (1967) assumed conical magnetic surfaces to model the solar wind flow. This is a connected to a broader class of possible choices, known as the split monopole configuration (e.g., (Blandford & Znajek 1977, Beskin et al. 1992a, 1998), in which the poloidal magnetic field is radial and has opposite polarity on both sides of the equatorial plane.

The integrals of motion $e(\Psi)$, $l(\Psi)$, $\Omega(\Psi)$, $k(\Psi)$, and $K(\Psi)$, in Bernoulli's and GSS equations (Equations (3.46) and (3.51) respectively) must be prescribed or fixed from the boundary conditions. In addition, regularity conditions on the separatrix surfaces [4] impose further restrictions, reducing the number of independent constant of motion. We will return to this when we discuss specifically the Blandford & Payne (1982) model.

3.4 Critical Surfaces

Waves are the mechanism by which information in a medium may be communicated from one region to another. Unlike unmagnetized fluids, where the ordinary sound is the only normal mode that can propagate, magnetized media can sustain more than one normal mode. Here we will consider only the non-relativistic case. In ideal MHD the density, velocity and magnetic field evolve according to Equations (3.11), (3.12) and (3.8) (without the diffusive term). Analogously, the pressure evolves according to

$$\frac{\partial p}{\partial t} = -\mathbf{v} \cdot \nabla p - \gamma p \nabla \cdot \mathbf{v}. \tag{3.52}$$

Consider a magnetostatic equilibrium in which the density, pressure, velocity and magnetic field are $\rho_0(\mathbf{r})$, $p_0(\mathbf{r})$, $\mathbf{v}_0(\mathbf{r})$ and $\mathbf{B}_0(\mathbf{r})$. Now consider small perturbations from equilibrium, such that $q(\mathbf{r}, t) = q_0(\mathbf{r}) + \delta q(\mathbf{r}, t)$ with $|\delta q| \ll q_0$, where q represents any

[4] Defined in Section 3.4, paragraph Magnetoacoustic Waves

of the quantities of interest and q_0 is the unperturbed state. The linearized equations are

$$\begin{aligned}
\frac{\partial \delta\rho}{\partial t} &= -\delta\mathbf{v}\cdot\nabla\rho_0 - \rho_0\nabla\cdot\delta\mathbf{v}, \\
\frac{\partial \delta p}{\partial t} &= -\delta\mathbf{v}\cdot\nabla p_0 - \gamma p_0\nabla\cdot\delta\mathbf{v}, \\
\frac{\partial \delta\mathbf{B}}{\partial t} &= \nabla\times(\delta\mathbf{v}\times\mathbf{B}_0).
\end{aligned} \tag{3.53}$$

Because of the assumption that the perturbations are small compared to the unperturbed quantities, the former can be considered constant, such that Equations (3.53) constitute a set of linear differential equations with constant coefficients. Therefore, the solution can be sought as a superposition of plane monochromatic waves of the form $\delta q(\mathbf{r},t) \sim \exp[i(\mathbf{k}\cdot\mathbf{r}-\omega t)]$, where ω is the wave frequency and $\mathbf{k}$ is the wave vector. That is, all the disturbed quantities are assumed to depend only on the time t and the position. The system of Equations (3.53) is reduced to a set of linear algebraic equations in the perturbed quantities δq, with respect to which the system is closed, linear and homogeneous. The system has nontrivial solutions only if its determinant is identically null.

The determinant is derived (e.g., Somov 2006) in a reference frame with one of the axes along the wave vector $\mathbf{k}$. In such evaluation it was used the frequency in the comoving system, $\omega_0 = \omega - \mathbf{k}\cdot\mathbf{v}$. Setting the determinant equal to zero yields the dispersion relation, i.e., the relation between the frequency and the wave number:

$$\left[\omega_0^2 - (\mathbf{k}\cdot\mathbf{v})^2\right]\left[\omega_0^4 - |\mathbf{k}|^2\omega_0^2 c_{\rm ms}^2 + (\mathbf{k}\cdot\mathbf{v})^2\,|\mathbf{k}|^2 c_{\rm s}^2\right] = 0, \tag{3.54}$$

where $c_{\rm s} = \sqrt{(\partial P/\partial\rho)_0}$ is the unperturbed sound speed and $c_{\rm ms} = c_{\rm s} + v$ is the speed of the magneto-acoustic mode, that will be discussed below.

The above equation has three roots, that correspond to different perturbation modes, each characterized by its own propagation velocity (phase velocity)

$$\omega_0 = \mathbf{v}_{\rm pha} \cdot \mathbf{k} \tag{3.55}$$

and group velocity

$$d\omega_0 \equiv \mathbf{v}_{\rm gr} \cdot d\mathbf{k}. \tag{3.56}$$

Alfvén Waves The first factor in Equation (3.54) comes from considering transverse waves: $\omega_0^2 = (\mathbf{k}\cdot\mathbf{v})^2$ (or $\omega_0 = \pm\,\mathbf{k}\cdot\mathbf{v}$) and is the Alfvén wave branch, that corresponds to waves with phase velocity

$$v_{\rm A} = \pm\,\frac{B}{\sqrt{4\pi\rho}}\,\cos\theta, \tag{3.57}$$

where $v_{\rm A} = |\mathbf{v}_{\rm A}|$ and $\mathbf{v}_{\rm A}$ is the Alfvén velocity vector, θ is the angle between the direction of wave propagation $\mathbf{k}/k$ and the ambient field vector $\mathbf{B}_0$, $B = |\mathbf{B}_0|$ and $\rho = \rho_0$.

Thus, the Alfvén waves represent the displacements of plasma together with the magnetic field frozen into it. Note that these waves do not change the density of the medium where they propagate. They are transversal with respect to both the field direction and the wave vector. This means that they behave as waves on stretched strings, where the restoring force is provided by the magnetic tension $(\mathbf{B}\cdot\nabla\mathbf{B}/4\pi)$. The group velocity of

the Alfvén waves is

$$\mathbf{v}_{\mathrm{A}} = \pm \frac{\mathbf{B}}{\sqrt{4\pi\rho}}, \tag{3.58}$$

This shows that unlike other MHD waves that tend to be dispersive (i.e., their group and phase velocities differ), the Alfvén group speed coincides with the Alfvén speed, propagating either parallel or anti-parallel to the magnetic field.

Magnetoacoustic Waves There are two other branches in the dispersion equation, defined by the solutions to the quartic equation

$$\omega_0^4 - k^2\omega_0^2 c_{\mathrm{ms}}^2 + (\mathbf{k}\cdot\mathbf{v})^2 k^2 c_{\mathrm{s}}^2 = 0.$$

The solutions are two values of ω_0^2, which differ in absolute magnitude, corresponding to two different waves with the phase velocities

$$v_{\mathrm{FM,\,SM}}^2 = \frac{1}{2}\left[v^2 + c_{\mathrm{s}}^2 \pm \sqrt{\left(v^2 + c_{\mathrm{s}}^2\right)^2 - 4v^2 c_{\mathrm{s}}^2 \cos^2\theta}\right]. \tag{3.59}$$

These waves are the fast (v_{FM}) and the slow (v_{SM}) magneto-acoustic waves, respectively (van de Hulst 1951). The entropy of the medium does not change in such waves, analogous to the usual sound wave case (Somov 2006). Also analogous to the ordinary sound waves, and unlike the Alfvén waves, these two modes are compressible MHD waves. The group velocities of the two magneto-acoustic branches are more complex than that of the Alfvén wave. Studying their limiting cases, $\theta = 0, \pi/2$, shows that for $\theta = 0$, the group velocity of the slow mode is different from the corresponding phase velocity. That

defines a new velocity, called cusp velocity:

$$v_{\rm C} = \frac{c_{\rm s} v_{\rm A}}{c_{\rm s}^2 + v_{\rm A}}. \tag{3.60}$$

This is the smallest of all the characteristic speeds of the problem, including the speed of sound. Although $v_{\rm C}$ does not correspond to the phase speed of any wave in the problem, information is transported normally to $\mathbf{k}$ and $\mathbf{B}$ by the wave packet of the standing slow mode wave.

The slow- and fast-magnetosonic solutions define two additional critical points, of saddle type, within the flow domain, in addition to the Alfvén critical point. The flow changes its regime when it crosses each of these three critical surfaces, *separatrices*, which are not *a priori* known and have to be found simultaneously with the solution (Contopoulos & Lovelace 1994). The cusp velocity defines yet another critical surface of the flow, hence its importance in MHD flows. Demanding that the solution be regular at these points imposes two constraints on the integrals of motion.

The GSS equation, one of the expressions that define the flow solutions, is a second-order ODE of mixed type that becomes either elliptical or hyperbolic according to the region analysed (that determines the sign of the associated discriminant, D). The GSS equation is (e.g., CL94):

- elliptic for $v_{\rm p} < v_{\rm C}$.
- hyperbolic for $v_{\rm C} < v_{\rm p} < v_{\rm FM}$

- elliptic for $v_{\rm SM} < v_{\rm p} < v_{\rm FM}$
- hyperbolic $v_{\rm p} > v_{\rm FM}$.

These regime changes make more difficult the numerical resolution of the problem.

3.5 Wind launching

The presence of an ordered, large-scale magnetic field threading an AGN accretion disc has been suggested by several authors (e.g., Blandford & Payne 1982, Contopoulos & Lovelace 1994, Königl & Kartje 1994) as a mechanism able to either confine the BLR clouds (as in Emmering et al. 1992) or direct the outflow velocity field (e.g., Everett 2005). Here we will not discuss the origin of such magnetic fields, and will just assume that the field is present and study its effects within the postulated framework.

One important question is to study the conditions under which the outflow can be launched. In particular, it is important to realize that the geometry of the magnetic field responsible for launching such an outflow field can not be arbitrary. Here we just outline the general approach to this problem. A detailed discussion on it can be found in Spruit (1996).

Geometrical constraints on the field lines that allow an outflow can be obtained studying the shape of the effective potential $\Phi_{\rm eff}$ near the disc surface (Blandford & Payne 1982). The effective potential per unit mass has two contributions: the gravitational

potential and a centrifugal term

$$\Phi_{\text{eff}} = -\frac{GM_{\text{BH}}}{\left(r^2+z^2\right)^{1/2}} - \frac{1}{2}\Omega_{\text{m}}^2 r^2, \tag{3.61}$$

where Ω_{m} is the angular velocity of the matter at radius r.

According to Ferraro's isorotation law, matter at $r \leq r_{\text{A}}$ is approximately in co-rotation with the magnetic field lines at angular velocity Ω. Thus, since the footpoints of the lines are anchored to the disc, it is justified to adopt $\Omega = \Omega_{\text{K}}(r_0)$, where the disc was assumed to be geometrically thin, such that the rotation velocity would be Keplerian, and r_0 is the radius of the footpoint of the field line. Then, Equation (3.61) may be rewritten as

$$\Phi_{\text{eff}} = -\frac{GM_{\text{BH}}}{r_0}\left[\frac{1}{2}\left(\frac{r}{r_0}\right)^2 + \frac{r_0}{\left(r^2+z^2\right)^{1/2}}\right] = \text{const.} \tag{3.62}$$

The equipotential surfaces of Φ_{eff} are shown in Figure 3.2.

The first derivatives of Φ_{eff} vanish at $(r_0, 0)$. The condition for unstable equilibrium with respect to a small displacement along the field line is that the second derivative of the effective potential along the field line at $(r_0, 0)$ be negative. This yields the constraint

$$\frac{\partial^2 \Phi_{\text{eff}}}{\partial s^2}(r_0, 0) = -\frac{GM_{\text{BH}}}{r_0^3}\left(\sin^2\vartheta - 3\cos^2\vartheta\right) < 0, \tag{3.63}$$

where $\partial_s \equiv \mathbf{s}\cdot\nabla$ is the derivative along the field line and ϑ is the angle between the field line and the r-axis at $(r_0, 0)$ and thus $r = s\cos\vartheta$ and $z = \sin\vartheta$. This defines a critical angle $\vartheta_{\text{c}} = 60^\circ$, such that only field lines that start at $\theta < \theta_{\text{c}}$ can successfully accelerate

matter outwards from the surface of the disc. Note that this critical angle is independent of r_0.

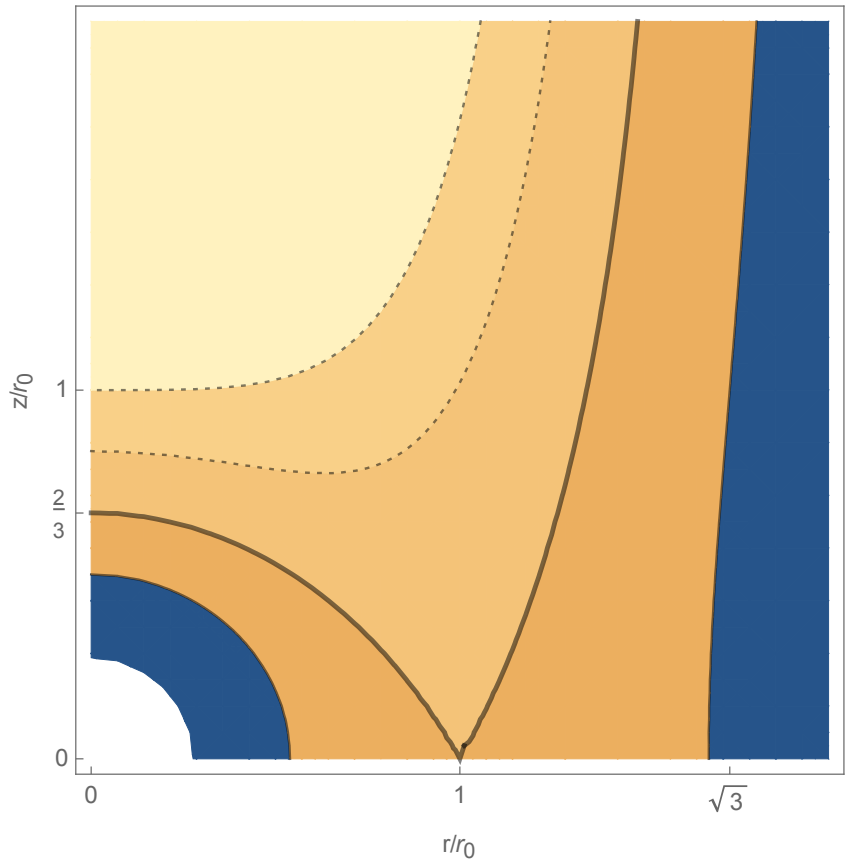

Figure 3.2: Equipotential surfaces of $\Phi_{\rm eff}$, Equation (3.62). The thick solid line is the surface of marginal stability $\Phi_{\rm eff} = -\frac{3}{2}GM_{\rm BH}/r_0$. The region above it corresponds to stable configurations (increasing potential, shown with dotted lines). For field lines in that region, small perturbations would make the matter fall along the line back to the disc. For field lines in the unstable region (decreasing potential), a small perturbation would make the fluid move outward, if the line is favourably inclined (see text).

3.6 Self-similar solutions

There is an important class of physical phenomena in which scale symmetry allows us to reduce the number of independent variables of the problem. This happens because the solution is similar to itself (self similar) if the variables are conveniently scaled. In this way a considerable simplification is achieved, that frequently allows the analytical treatment of the problem. Examples can be found in many fields of physics (e.g., fluid dynamics, the physics of waves) as well as in astrophysics (e.g., supernovæ, jets). Much more detailed and general discussion on the subject can be found in the book by Barenblatt (1996). See also (e.g.) Carter & Henriksen (1991), Gratton (1991).

Physical self-similar phenomena are characterized by their reproduction at any time (temporally self-similar) or position (spatially self-similar) from a previous state via an appropriate self-similar mechanism (Lery 2007). Therefore, the full phenomenon can be reduced to the study of the properties of the system for only a specific time or location. Mathematically, it implies a reduction of the system of PDEs that describe the system, to ODEs, which most of the time makes their investigation simpler. In a steady problem, spatial self-similarity may be viewed as a method of nonlinear separation of the variables in the set of the relevant equations, that enables acquisition of analytical solutions (Tsinganos 2010).

In the context of MHD problems, the properties of the self-similar solutions have

been extensively studied in numerous works both in the non-relativistic (e.g., Bisnovatyi-Kogan et al., 1979; Blandford & Payne, 1982; Tsinganos & Sauty, 1992; Contopoulos & Lovelace, 1994; Sauty & Tsinganos, 1994; Tsinganos et al., 1996; Ostriker, 1997; Sauty et al., 1999) and the relativistic (e.g., Li et al. 1992) cases. It is worth noting that there are some caveats and restrictions to this approach when attempting to use it to describe the real two-dimensional flows. For instance, the model cannot admit general boundary conditions in this simplified reformulation, and sometimes it cannot satisfy *a priori* imposed thermodynamics (Heyvaerts 1996).

In this context there are two main types of spatial self-similarity that can been found in the literature: meridional and radial. The latter is more appropriate to describe winds from accretion discs (e.g., Blandford & Payne, 1982; Lovelace et al., 1991; Contopoulos & Lovelace, 1994; Li, 1995; Ferreira & Pelletier, 1995; Ferreira, 1997; Casse & Ferreira, 2000a,b; Vlahakis et al., 2000). However, these solutions fail close to the rotation axis, a region for which meridional models are best suited (Tsinganos & Trussoni, 1990, 1991; Tsinganos & Sauty, 1992a,b; Trussoni & Tsinganos, 1993; Sauty & Tsinganos, 1994; Trussoni et al., 1997). A schematic representation of the two possibilities of self-similar field line structure, adopted from Tsinganos (2007), is shown in Figure 3.3.

Vlahakis & Tsinganos (1998) unified all existing cases of self-similar outflow exact MHD solutions by means of a systematic analytical treatment, such that all known examples of exact solutions represent special cases of a general formulation. Any physical

quantity $q(r, z)$ in the problem is described as $q(r, z) = G_{\rm q}(r) f_{\rm q}(x)$, where x is the self-similar variable. Depending on the choice for x, one of the above categories is recovered. Thus, $x = \theta$ corresponds to radially self-similar models with conical singular surfaces, while $x = r$ corresponds to meridionally self-similar models with spherical singular surfaces. This category includes the classical Parker (1963) description of a stellar wind; it also contains the prescribed field line models of Tsinganos & Trussoni (1991).

We will next discuss first the (radially) self-similar approach to solving the MHD wind equations in a general way and then will focus in the particular case of the Blandford & Payne (1982) work.

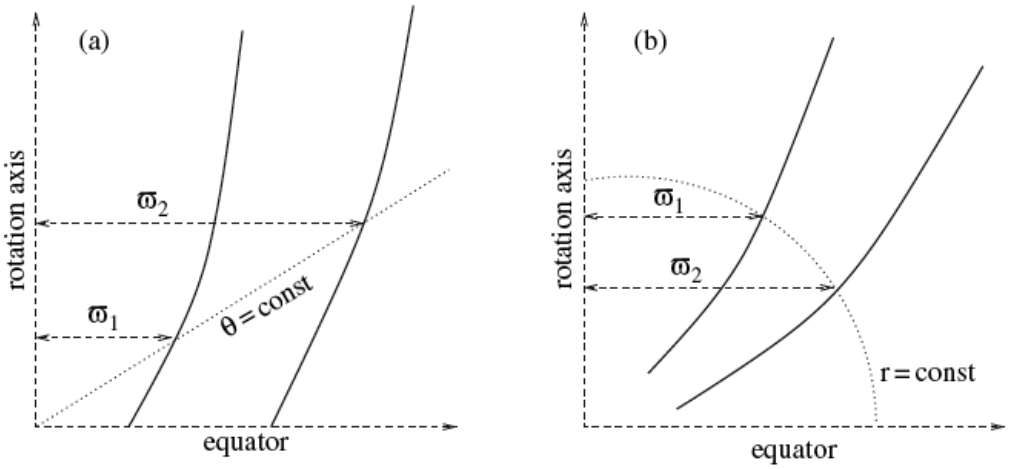

Figure 3.3: Schematic of the two possibilities of self-similar field-line structure. The thick lines represent two arbitrary field lines. Left panel shows the case of radial self-similarity, wherein the ratio ϖ_1/ϖ_2 for the intersection of any poloidal line with a cone is the same for any value of θ. The right panel illustrates the meridional self-similar case. From Tsinganos (2007).

The adoption of a self-similar *Ansatz* in the disc outflow context is based on the realization that stationary axisymmetric magnetic field configurations are characterized by a set of nested magnetic flux surfaces $\Psi(r,z) = \text{const.}$ (Contopoulos & Lovelace 1994). Based on the bijection that exists between the value of $\Psi(r,z)$ and the footpoint r_0, a possible general form for the equation describing the flux surface is

$$r = r_0\,\xi(z/r_0) \equiv r_0\,\xi(\chi), \tag{3.64}$$

where $\chi = z/r_0$ is the renormalized (self-similar) z variable.

The above scaling and a suitable choice of boundary conditions along the disc suggest looking for solutions of the form $q(r,z) = G_{\rm Q}(r_0) f_{\rm Q}(z/r_0)$ for any physical quantity $q(r,z)$, separating the dependences on the two variables. This effectively reduces the problem from the original set of PDEs to a second-order ODE in the self-similar variable χ.

The basis for the construction of the self-similar solution is the power dependence on the radius r of the gravitational potential, that, in cylindrical coordinates, is

$$\Phi_{\rm g} = -\frac{GM}{\left(r^2+z^2\right)^{1/2}} = -\frac{GM}{r}\left(1+\frac{z^2}{r^2}\right)^{-1/2}. \tag{3.65}$$

The last expression shows explicitly the gravitational potential as a power law of the disc radius. By adopting the same scaling for any physical quantity $q(r,z)$ and using the self-similar *Ansatz* the function $G_{\rm Q}(r_0)$ is written as $G_{\rm Q}(r_0) = r_0^{\alpha_{\rm Q}}$, where the exponent $\alpha_{\rm Q}$ has to be obtained by dimensional analysis. This returns a set of equations in the radial

self-similar variable that provides algebraic relations between all the different exponents and can be trivially solved (Ferreira 2002).

If, as done by (e.g.) Contopoulos & Lovelace (1994), an indeterminate power b is chosen for the exponent in the self-similar substitution of the magnetic flux, we can then write

$$\Psi(r,\theta) = r^b\,\mathcal{X}(\chi), \tag{3.66}$$

which requires the magnetic field to scale as

$$\mathbf{B} \propto r^{b-2}\mathbf{B}(\chi), \tag{3.67}$$

where the definition of the poloidal field is given in Equation (3.20). Note that it is also implicitly assumed that the field azimuthal component follows the same scaling as the poloidal component. As discussed by Heyvaerts (1996), this is a natural assumption, because it extends to the full vector magnetic field the spherical self-similarity adopted for the other fields in the problem.

Because all terms in each equation must have the same dependence on the self-similar radial variable, it is also straightforward to get the other dependences from the relevant equations. From Bernoulli's equation (3.46), it follows $e \propto r_0^{-1}$. From the momentum (Euler's) equation (3.17b): $v \propto r_0^{-1/2}$, such that the Keplerian angular velocity dependence $\Omega_{\rm K} \propto r_0^{-3/2}$ is satisfied. The first term in the equation of the conserved angular momentum (3.35) gives $l \propto r_0^{1/2}$. Applying this result to the second term of the same

equation provides $k \propto r_0^{b-3/2}$. The exponent for the mass density can be obtained through the equation that defines the conserved mass load (3.25), that shows that $\rho \propto r^{2b-3}$.

Note that the square of the Alfvén Mach number $m = \mathcal{M}^2$ is independent of the radius r_0. As it can be seen, the solutions are a family that depends on the free parameter b. Each particular choice of that parameter represents a different case within the family. For instance, Blandford & Payne (1982) chose $b = 3/4$ to specify the radial scaling of their model, such that $\Psi \propto r_0^{3/4}$. Therefore, within this model, the magnetic flux diverges for $r_0 \to \infty$.

3.7 The Blandford-Payne MHD Wind Solution

Solutions of the steady, axisymmetric, non-relativistic ideal MHD equations assuming a spherically self-similar scaling were obtained by, e.g., Blandford & Payne (1982, BP82 hereafter) for the cold plasma outflow from the surface of a Keplerian disc. This solution for the field can be written in terms of variables χ, $\xi(\chi)$, ϕ, and r_0, which are related to the cylindrical coordinates via

$$\mathbf{r} \equiv [r, \phi, z] = \left[r_0 \xi(\chi), \phi, r_0 \chi\right], \tag{3.68}$$

such that the adopted independent variables (r_0, χ) are a pair of spatial coordinates analogous to (r, z). The function $\xi(\chi)$ describes the shape of the field lines and, in the general case, is not *a priori* known, but found as part of a self-consistent solution to the MHD

equations. The flow velocity components are given by

$$\mathbf{v} = \left[\xi'(\chi) f(\chi), g(\chi), f(\chi)\right] \sqrt{\frac{GM}{r_0}}, \tag{3.69}$$

where $\xi' = d\xi/d\chi$ and M is the mass of the central black hole. The parameter r_0 is the field line footpoint, so that $\xi(0) = 1$.

Another important dimensionless parameter for ideal MHD is the ratio of thermal to magnetic pressure,

$$\beta_{\rm pl} = \frac{p}{B^2/8\pi}, \tag{3.70}$$

where p is the thermal pressure. In low $\beta_{\rm pl}$ plasmas the dynamics is dominated by the magnetic field. Conversely, in high $\beta_{\rm pl}$ the standard hydrodynamical terms are more important. Thus, the cold plasma assumption means that a low $\beta_{\rm pl}$ is assumed, such that the plasma pressure forces can be ignored in the wind. Another way to state it is by saying that this assumption imposes that the basic launching mechanism is magneto-centrifugal, based on the force balance between gravity and centrifugal effects on the plasma along field lines. Other authors showed that relaxing this assumption, i.e., if the flow started up hot and created a geometrically thick disc or torus, the launching mechanism need not to be magneto-centrifugal. Examples of influential works on the theory of warm jets and winds from accretion discs are Vlahakis et al. (2000) and Vlahakis & Königl (2003) for the non-relativistic and relativistic cases respectively.

Although the cold plasma assumption is not valid close to and inside the disc itself,

where pressure dominates, such that the wind velocity will be subsonic ($v < c_{\rm s}$), BP82 ignored the dense part of the flow entirely and assumed $c_{\rm s} \ll v \ll v_{\rm A}$, where $v_{\rm A}$ is the Alfvén speed, Equation (3.37).

The magnetic field and density are also written in terms of the self-similar coordinates:

$$\mathbf{B} = B_0(r_0) \left[b(\chi)\xi'(\chi), B_\phi(\chi), b(\chi) \right], \tag{3.71}$$

and

$$\rho = \rho_0(r_0)\varrho(\chi), \tag{3.72}$$

respectively, where $B_0 = |\mathbf{B}_{\rm p}(\chi = 0)|$ and $\varrho(\chi = 0) = 1$ if $\rho_0(r_0)$ is the density at the equator.

Thus, the GSS equation (3.51) is rewritten as

$$\xi f^2 T(m-1)^2(t-1)J^{-1}S^{-2}\xi'' + H(\chi, \xi, \xi') = 0, \tag{3.73}$$

where

$$\begin{aligned} H(\chi, \xi, \xi') = {} & (m-1)^2 \left[\xi T + (n-m-1)f^2 J \right] T \\ & + m(m-1)[(t-1)\xi T S \\ & - \xi f^2(\chi + \xi\xi')(\xi\xi' - \xi\xi' S^3 - \chi S^3)] \\ & + (m-1) \left[m\xi^2(\xi T - m f^2 J) - 5/4(n-1)\xi T^2 \right] \\ & + 2m^2(\xi^2 - \lambda)(m f^2 J - \xi T), \end{aligned} \tag{3.74}$$

where $\xi'' = d\xi^2/d\chi^2$, and

$$T = \xi^2 + \frac{2}{\sqrt{\xi^2 + \chi^2}} - 3, \tag{3.75}$$

$$S = (\xi^2 + \chi^2)^{-1/2}, \tag{3.76}$$

$$J(\chi) = \xi(\chi) - \chi\,\xi'(\chi). \tag{3.77}$$

In the above expression, T is related to the effective gravitational potential, $T \equiv -2[\Phi(r,z) - \Phi(r_0,0)] = \xi^2 + 2S - 3$, S is related to the true gravitational potential and J is the determinant of the Jacobian matrix of the transformation $(r,z) \rightarrow (r_0,\chi)$. The remaining quantities appearing in Equation (3.73) are defined according to

$$m(\chi) = \frac{4\pi\rho\, v_{\rm p}^2}{B_{\rm p}^2} = \kappa\, f\, \xi\, J, \tag{3.78}$$

$$n(\chi) = \frac{4\pi\rho\, v_{\rm p}^2}{B^2} = \frac{\kappa\, \xi\, f^3 J(1+\xi'^2)}{T}, \tag{3.79}$$

$$t(\chi) = \frac{4\pi\rho\, v_\theta^2}{B^2} = \frac{\kappa\xi f^3 J^3 S^2}{T}. \tag{3.80}$$

The square of the Alfvén Mach number at each position, m, has been introduced in Equation (3.36). The other two quantities correspond to the square of the Mach number relative to the fast magnetosonic wave speed (n), and the ratio of the square of the θ-component of the velocity in spherical geometry to the fast magnetosonic wave speed (t).

Following BP82, we introduce the dimensionless expressions of the integrals of motion defined in Equations (3.25)-(3.46), in terms of which the solutions are defined:

$$\kappa = k(1+\xi_0'^2)^{1/2}\frac{(GM/r_0)^{1/2}}{B_0} \tag{3.81}$$

$$\lambda = \frac{l}{(GMr_0)^{1/2}} \tag{3.82}$$

$$\epsilon = \frac{e}{(GM/r_0)}. \tag{3.83}$$

The parameters of the model are ϵ, λ and κ and $\xi_0' = \cot\vartheta_0$, where ϑ_0 is the angle that the poloidal field makes with the disc. However, due to the regularity conditions that must be satisfied, these parameters are not independent. Combining Equations (3.82) and (3.83) gives $\epsilon = \lambda - \frac{3}{2}$.

The value of $\xi_0' \equiv \xi'(\chi = 0)$ must be chosen to ensure the regularity of the solution at the Alfvén point. The solutions are therefore parametrized only by two numbers, which can be chosen to be κ and λ (e.g., BP82).

The function $g(\chi)$ in the azimuthal component of the velocity can be expressed in terms of the function m and the specific angular momentum, λ:

$$g(\chi) = \frac{\xi^2(\chi) - \lambda\, m(\chi)}{\xi(\chi)\left[1 - m(\chi)\right]}. \tag{3.84}$$

From this expression we can see again (cf. Equation (3.39)), that the point corresponding to $m = 1$ is a singular point of the problem. In particular, to avoid unphysical solutions there, the condition $\xi_{\rm A} = \xi(\chi_{\rm A}) = \lambda^{1/2}$ must be satisfied.

The dimensionless angular momentum and energy equations can be combined with the ϕ-component of the velocity equation to obtain a quartic equation for $f(\chi)$. In effect,

expressing f and g by Eqs (3.78) and (3.84) in terms of the Alfvén Mach number and of the function $\xi(\chi)$ and its derivatives, Equation (3.46) is transformed into such a fourth degree equation for the function $f(\chi)$:

$$T - f^2(1+\xi'^2) = \left[\frac{(\lambda-\xi^2)\,m}{\xi(1-m)}\right]^2. \tag{3.85}$$

Next, instead of using the complete GSS equation, BP82 adopted a slightly different approach and obtained a second-order differential equation for $\xi(\chi)$ by combining the differential form of Equation (3.85) with a component (chosen to be the z-component) of the momentum equation, Equation (3.17b). The flow is then fully specified by that equation and Equation (3.85), plus the boundary conditions, $\xi(0) = 1$ and $\xi'(0) = \xi'_0$. Later on, Contopoulos & Lovelace (1994), who employed the complete GSS equation, showed that both treatments were equivalent.

The result yielded an equation for the cold, non-relativistic case,

$$m' = \frac{dm}{d\chi} = \frac{\mathcal{N}}{\mathcal{D}}, \tag{3.86}$$

where the denominator is simple, given by

$$\mathcal{D} = \xi T(m-1)(t-1), \tag{3.87}$$

while the numerator has a complicated form

$$\mathcal{N} = mS^2\Big\{2m^2\chi\left(\xi^2-\lambda\right)J- \\ (m-1)\left[\frac{5}{4}T+\xi^2-S\right]\xi\left(\chi+\xi\xi'\right)- \tag{3.88}$$

$$(m-1)^2\left[\chi\left(\xi^2+T\right)-f^2\left(\chi+\xi\xi'\right)\right]J\Big\}, \tag{3.89}$$

where all the intervening functions and the dimensionless constant of motion λ have been defined above.

BP82 studied outflows that become super-Alfvénic (i.e., $m > 1$) at a finite height above the disc. The asymptotic conditions for such flows admit two kind of solutions that depend on the location of the fast-mode Mach number above the disc. For a cold flow, the square of the Mach number for the fast magnetosonic mode for an arbitrary scaling of density, magnetic field (and all relevant quantities of the problem) is given by Equation (3.79).

The two types of solutions are those that asymptotically approach $n = 1$ as $\chi \to \infty$, and those that attain $n > 1$ at a finite height from the disc.

3.7.1 Asymptotic solutions in BP82 model

We are interested in the first kind of solutions, for which the set of super-Alfvénic solutions are represented, according to BP82, by the following expressions:

$$\xi = c_1\,\chi^{\alpha}, \tag{3.90}$$

$$m = \frac{3\,c_1^2}{2\lambda - 3}, \tag{3.91}$$

with

$$\alpha = 1 - \frac{3^{3/2}}{\beta_1}, \tag{3.92a}$$

$$\beta_1 \equiv \kappa\,(2\lambda - 3)^{3/2} \gg 1, \tag{3.92b}$$

where the parameter β_1 controls the behaviour of the solutions far from the disc. The asymptotic value of the function f is given by

$$f_\infty = \left(\frac{2\lambda - 3}{3}\right)^{1/2}. \tag{3.93}$$

Although κ can have larger values, BP82 (and, e.g., Königl & Kartje 1994) considered only solutions with $\kappa < 1$, that represent winds that are magnetically dominated in the vicinity of the disc. The region in the κ - λ plane where the solutions remain everywhere sub-Alfvénic is bounded by the line $\lambda_{\rm min}(\kappa)$, given by $\kappa\lambda_{\rm min}(2\lambda_{\rm min} - 3)^{1/2} = 1$.

3.8 Emmering et al. (1992) model

The model of Emmering et al. (1992, hereafter EBS92) represents a simplified version of BP82 solution. The EBS92 solution corresponds to the case in which the solution asymptotically approaches $n = 1$ as $\chi \to \infty$, where $n(\chi)$ is the fast magnetosonic mode, defined in Equation (3.79).

While BP82 found their solutions by integrating a second-order differential equation, EBS92 impose *a priori* the functional form of the solution so that it will asymptotically tend to the BP82 solution. In their Equation (3.19), EBS92 give an explicit form for the function $\xi(\chi)$:

$$\xi = \left(\frac{\chi}{c_2} + 1\right)^{1/2}, \tag{3.94}$$

where $c_2 = \frac{1}{2}\tan\vartheta_0$ was chosen to ensure that the field lines make an initial angle ϑ_0 with the disc plane, so that $\cot\vartheta_0 = \xi_0' = \frac{d\xi(\chi)}{d\chi}|_{\chi=0}$ and the subscript 0 means, as before, that the quantities are evaluated at the disc plane. As shown in Equation (3.63), (see also e.g., BP82, Heyvaerts 1996), there is an upper limit for this angle, and it has to satisfy $\vartheta_0 < 60°$.

For the solution form proposed by EBS92, $\alpha = 1/2$ in Equations (3.90) and (3.92), so the only possible value of the parameter β_1 defined in Equation (3.92b) is $2 \times 3\sqrt{3} \approx 10$. Replacing this value in Equation (3.92b) gives that, as shown by EBS92, for this kind of solution and for this choice of the parameter α, the parameters κ and λ must be related by:

$$\kappa = 2\left(\frac{3}{2\lambda - 3}\right)^{3/2}. \tag{3.95}$$

Thus, in this model the solutions depend on λ and ϑ_0.

As in the framework of the BP82 model *for fixed* β_1, once either λ or κ is chosen, the other parameter is fixed. This can be seen in Figure 3.4 (similar to Figure 2 in BP82), that depicts the contours of $\beta_1 =$ const. for three different values of the parameter. Similarly,

Königl & Kartje (1994) found that, in practice, it was more convenient to adopt κ and ξ_0' as the independent wind parameters and then solve for λ rather than use λ and κ to describe the flow.

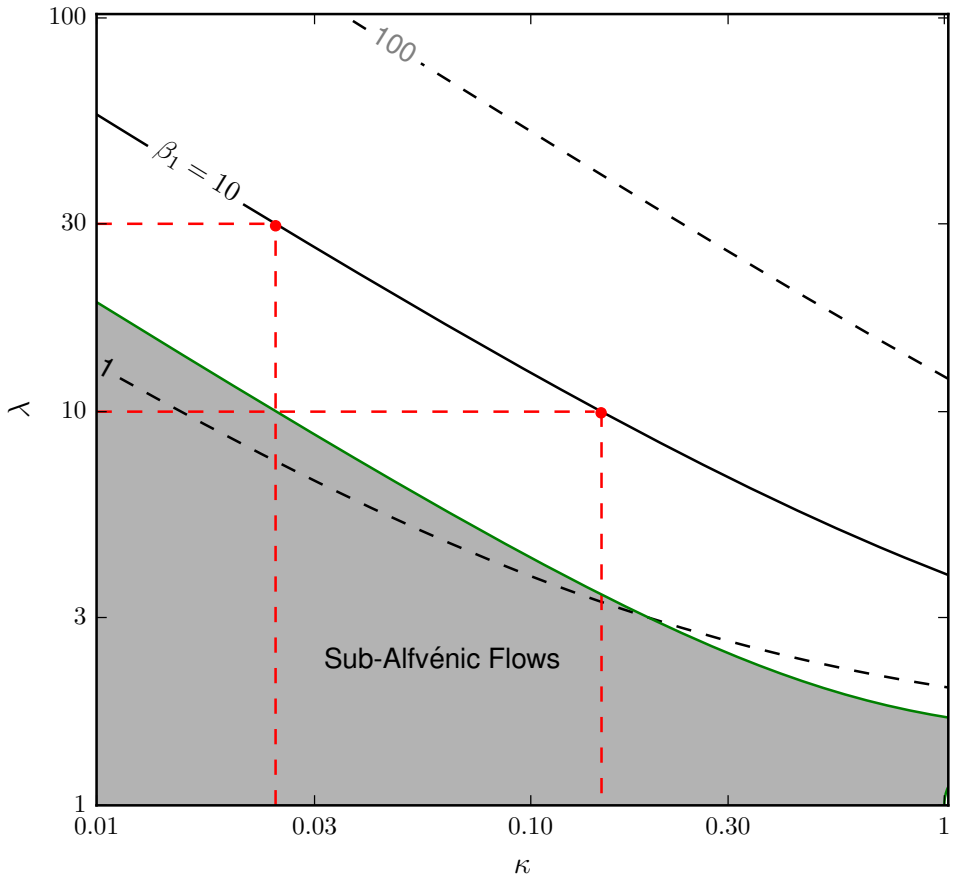

Figure 3.4: Contour plot analogous to Figure 2 of Blandford & Payne (1982). Each contour corresponds to a value of the quantity β_1, defined in Equation (3.92b), that is fixed for a given problem. The solid contour corresponds to $\beta_1 = 10$ and the possible (κ, λ) pairs for our problem, set by the condition (3.95) imposed by the Emmering et al. (1992) choice of parameters. The dashed red lines lead to the two points that we have explored in this work. Flows in the grey-shadowed region satisfy the condition $\kappa\lambda_{\rm min}(2\lambda_{\rm min} - 3)^{1/2} < 1$, and will never become super-Alfvénic ($4\pi\rho v_{\rm p}^2 > B_{\rm p}^2$).

In their paper, EBS92 proposed a then new interpretation of AGN BEL regions, by associating them with MHD winds launched from the accretion disc. The work was intended to support the cloud scenario of that region, and thus the authors proposed that small dense clouds of cool, predominantly molecular gas from the outer parts of an accretion disc are flung outward and away from the disc by magnetic stress. Once lifted, the clouds are exposed to the UV flux from the inner parts of the accretion disc, and quickly photoionized, starting to emit line photons. The velocity field of the line-emitting clouds will therefore combine the rotational motion of the disc with the outflow of the wind. As the disc is likely to be opaque and extend beyond the wind radius, only the nearer hemisphere will be seen, and so a broad, partly blueshifted line profile should be observed, with the central cusp originating from the outer parts of the disc. Another problem of the cloud scenario that was solved by this model is the confinement, necessary to avoid the disintegration of the clouds. In effect, without a magnetic field, it is necessary to invoke the existence of a dense and hot inter-cloud medium, coexistent with the cool clouds, to avoid their destruction.

Although we did not include such modification in our models, it is worth mentioning that EBS92 also explored the question of line broadening through Thomson scattering by hot, $T \sim 10^6$ K, electrons.

3.9 Chapter Summary

This chapter introduces a detailed description of the basics of non-relativistic MHD wind launch and driving theory, focused on steady state systems. These time-independent flows are characterized by a set of quantities conserved along the flow that constrain the dynamics of the system. We also discussed here the existence and location of the separatrices, i.e., the critical surfaces that are the boundaries between different regimes along the flow, each with its associated characteristic speed. We further discussed the conditions under which a magnetized outflow can be launched.

After setting the fundamentals and definitions, and discussed the general aspects of the problem at hand we described, in the second part of the chapter, and also in general, the self-similar *Ansatz* for solving the problem. The complexity of the governing system of PDEs imposes the need of making some assumptions in order to find solutions. Technically, the adoption of the self-similar *Ansatz* reduces the mathematical difficulty of finding steady wind solutions by transforming PDEs in the original MHD variables to ODEs in the single coordinate χ. We then presented the Blandford & Payne (1982) radially self-similar solution and ended the chapter with the model of Emmmering et al. (1992), that, as mentioned before, is the one we adopted as the wind driver in our final model.

4 The Modified Wind Model

Hall et al. (unpublished) extended the disc-wind model of Murray & Chiang (1997, MC97 hereafter) to the case of non-negligible radial and vertical velocities. The new treatment retains a number of factors neglected in MC97 and introduces the 'local inclination angle' to account for the different effective inclinations to the LOS of different portions of the emitting region. The geometry of this concept is shown in Figure 4.1, where we included two different choices of the tilt of the base of the emission region, β (see below), to enhance the appreciation of the effect of the newly introduced quantity on the observations. Below we summarize the modifications introduced by Hall et al.

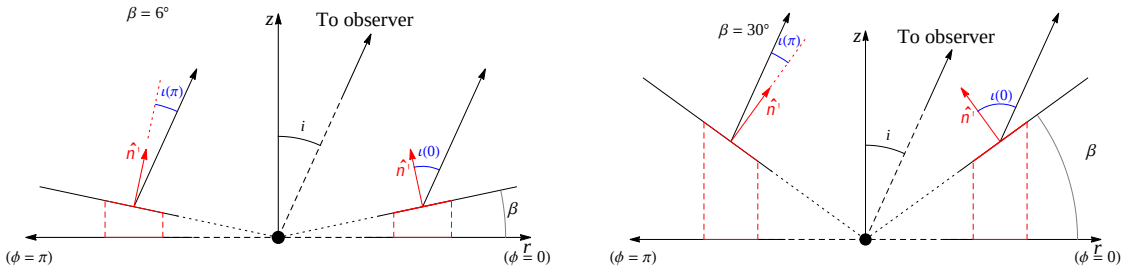

Figure 4.1: Cross-section of the local inclination angle concept geometry. The disc and the height of the emission region are not shown in this cartoon. The emission region is modelled as a conical surface described by the locus of points $z = Xr$, for all azimuthal angles ϕ and whwre $X = \tan(\beta)$, and β is the half-opening angle of the emission region. If X is small (e.g., $X = \tan(6^\circ) \sim 0.1$, as we assumed in this work), the difference between the disc and the emission region normals is small enough and can be safely ignored. However, for larger X values (e.g., $X = \tan(30^\circ) \sim 0.577$), that assumption is not longer valid. In effect, for such values of X and i, the half of the emission region nearest to us ($\phi \sim 0$) will have smaller projection on the LOS than the far half ($\phi \sim \pi$), that will be closer to face-on. The local inclination angle, defined through $\cos\iota = \cos i \cos\beta(r) - \cos\phi \sin i \sin\beta(r)$ is, then, the angle between the local normal to the interior surface of a cone (shown as the $\hat{\mathbf{n}}'$ red arrows in the diagram) and a line making an angle i with the axis of the cone in the $\phi = 0$ plane.

We assume the SMBH is at the origin of a cylindrical coordinate system (r, ϕ, z) with the z axis normal to the accretion disc and the observer, in the xz plane, making an angle i with the disc axis. At any r, the azimuthally symmetric emitting surface has its base at $z_{\rm em} = r \tan \beta(r)$ above the disc plane and has a thickness that satisfies $l_{\rm em}(r) \ll r$; thus, the source function S_ν [5] can be approximated as a function of radius only. The wind streamlines make an angle of $\vartheta_0(r, z)$ relative to the disc plane. Figure 4.2 depicts the system geometry and shows streamlines for two different launching angles.

[5] A brief discussion on the topic can be found in Appendix A. In chapter 5, section 5.1.1 we discuss the source function for our specific problem.

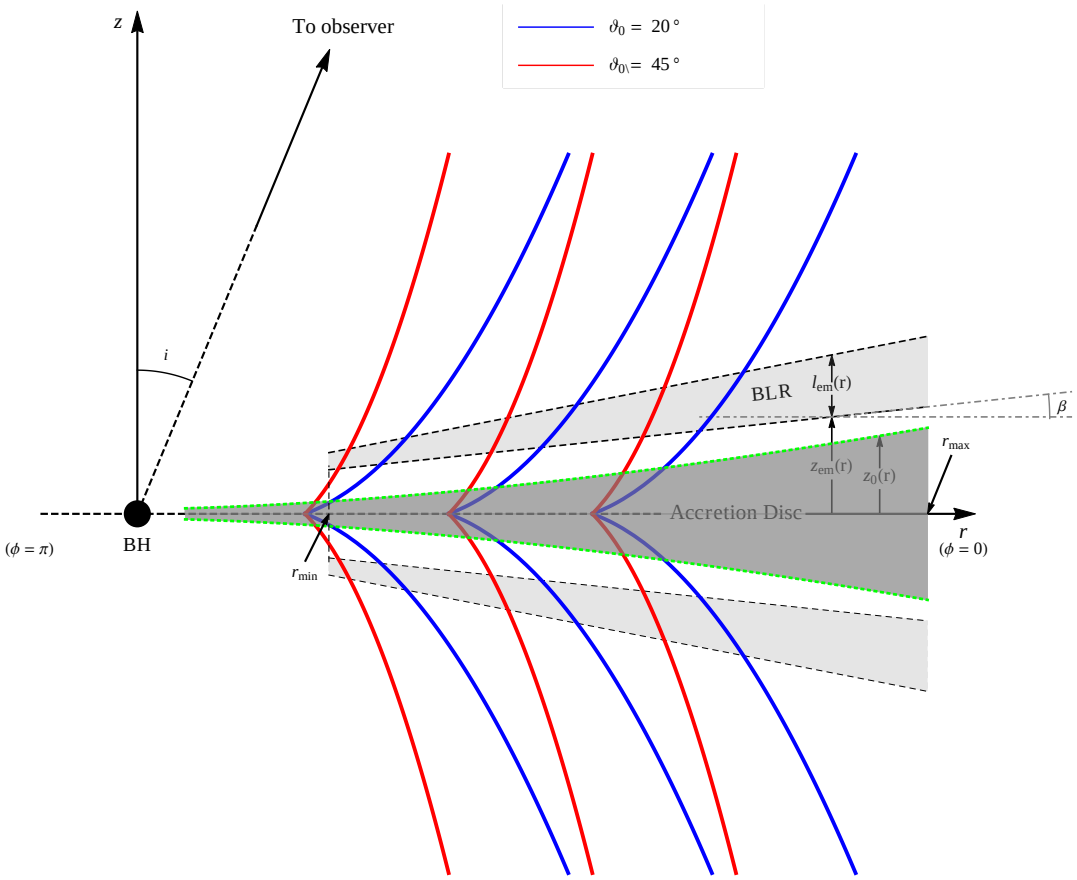

Figure 4.2: Streamlines for two different launching angles: $\vartheta_0 = 20°, 45°$. The disc midplane is assumed to lie in the $z = 0$ plane and the disc is assumed to be opaque, such that the observer, at an angle i from the $+z$ axis, sees only the upper quadrants. The lower dashed line represents the base of the emitting region, tilted by an angle β with respect to the disc plane. The BLR is a layer of thickness $l_{\rm em}(r)$ beginning a distance $z_{\rm em}(r)$ above the disc midplane and spanning radii $r_{\rm min} < r < r_{\rm max}$. The height of the disc continuum photosphere is $z_0(r)$, where r is the cylindrical radial coordinate. The disc wind lies at $z(r) > z_{\rm em}(r)$, and the emitting region for a given line is near the base of the wind, at $z_{\rm em}(r) < z < z_{\rm em}(r) + l_{\rm em}(r)$ above the disc midplane.

Under these assumptions, the monochromatic specific luminosity for a given line in the direction of the observer, $L_\nu(\hat{\mathbf{n}})$, is given by

$$L_\nu(\hat{\mathbf{n}}) = \int_{r_{\rm min}}^{r_{\rm max}} S_\nu(r)\ a(r)\ r\ dr \int_0^{2\pi} [1 - e^{-\tau_\nu(r,\phi,\hat{\mathbf{n}})}] \cos\iota(r,\phi,\hat{\mathbf{n}})\ d\phi \tag{4.1}$$

where $I_\nu = S_\nu(r)[1 - e^{-\tau_\nu}]$ is the specific intensity, $a(r)\ r\ dr d\phi$ is the area of the emitting surface between cylindrical radii r and $r + dr$, τ_ν is the optical depth from $z_{\rm em}(r) = r\tan\beta(r)$ to infinity along the direction $\hat{\mathbf{n}}$ from the location (r,ϕ), and $\iota(r,\phi,\hat{\mathbf{n}})$ is the local inclination angle between $\hat{\mathbf{n}}$ and the local normal to the surface at radius r and azimuthal angle ϕ. For $i < 90^\circ - \beta(r)$, the area factor and the local inclination angle are given by

$$a(r) = \frac{1}{\cos\beta(r)} \tag{4.2}$$

and

$$\cos\iota = \cos i\cos\beta(r) - \cos\phi\sin i\sin\beta(r)\,, \tag{4.3}$$

respectively. Note that for an emitting surface which can be approximated as a flat disc, $\beta(r) = 0$ and so $a(r) = 1$ and $\cos\iota = \cos i$, in which case Equation (4.1) reduces to Equation (4) of MC97. Also note that for $i = 0$, $\cos\iota = \cos\beta(r)$. We will primarily consider the case of constant β, independent of r, which corresponds to a conical emitting surface.

To calculate the optical depth, we use the fact that the path element through the emitting region along the LOS to the observer is $d\ell = dz\cos\beta/\cos\iota$ and convert the

integral along ℓ to an integral along z. Thus, τ_ν is given by

$$\tau_\nu(r,\phi,\hat{\mathbf{n}}) = \frac{\cos\beta(r)}{\cos\iota(r,\phi,\hat{\mathbf{n}})}\int_{z_{em}}^{\infty} k_0(r,z)\varphi_\nu(r,\phi,z)dz, \tag{4.4}$$

where φ_ν is the line profile function at the cylindrical coordinates (r,ϕ,z) and the line opacity k_0 is assumed to be a function of r and z only. That is,

$$k_0(r,z) = \frac{\pi e^2}{m_e c} f\ \chi_i\ \eta_i\ n(r,z), \tag{4.5}$$

where e is the electric charge in esu, f is the transition's oscillator strength, χ_i is the abundance of the element in question, η_i is the ionization fraction of the ion in question, and $n(r,z)$ is the hydrogen number density. To simplify some later algebra we assume $n(r,z)$ drops off as a half-Gaussian in the emission region ($z > z_{\rm em}$):

$$n(r,z) = n_0(r)\exp\left[-\frac{1}{2}\left(\frac{z-z_{\rm em}}{l_{\rm em}}\right)^2\right]. \tag{4.6}$$

For the radial dependence of the density, MC97 adopted $n_0(r) = n_0(r_{\rm min}/r)^{1/2}$, but MC98 adopted $n_0(r) = n_0(r_{\rm min}/r)^2$. We adopted the latter as a benchmark because it more closely approximates the radial density dependence of a Shakura & Sunyaev (1973) accretion disc.

For a given ion, we assume a characteristic speed $v_{\rm tt}$ (incorporating both thermal and turbulent motions), so that its line profile function is a Gaussian:

$$\varphi_\nu(r,\phi,z) = \frac{1}{\sqrt{2\pi}\Delta\nu_{\rm tt}}\exp\left[-\frac{1}{2}\left(\frac{\nu-\nu_0(1+\hat{\mathbf{n}}\cdot\tilde{\mathbf{v}}(r,\phi,z)/c)}{\Delta\nu_{\rm tt}}\right)^2\right], \tag{4.7}$$

where $\tilde{\mathbf{v}}(r, \phi, z)$ is the bulk velocity of the gas at (r, ϕ, z) and $\Delta\nu_{\rm tt} = \nu_0 v_{tt}/c$.

Evaluating the optical depth thus requires finding $\tilde{\mathbf{v}} \cdot \hat{\mathbf{n}}$, the projected velocity along $\hat{\mathbf{n}}$, at all (r, ϕ, z). To evaluate the optical depth τ_ν, MC97 expanded the projection of the wind velocity along the LOS, $\tilde{\mathbf{v}} \cdot \hat{\mathbf{n}}$, in terms of $z - z_{\rm em}$ to first order to obtain (their Equation (12))

$$\begin{aligned} \hat{\mathbf{n}} \cdot \tilde{\mathbf{v}}(r, \phi, z) &\cong \hat{\mathbf{n}} \cdot \tilde{\mathbf{v}}(r, \phi, z_{\rm em}) + \hat{\mathbf{n}} \cdot \mathbf{\Lambda} \cdot \hat{\mathbf{n}} \, \frac{(z - z_{\rm em})}{\cos\iota/\cos\beta} \\ &\equiv v_{\rm D}(r, \phi, z_{\rm em}) + \frac{(z - z_{\rm em})}{l_{\rm em}} \, v_{\rm sh}(r, \phi, z_{\rm em}), \end{aligned} \tag{4.8}$$

where $\mathbf{\Lambda}$ is the strain tensor, that will be described below.

The zeroth order term in Equation (4.8) is the Doppler velocity $v_{\rm D}$:

$$v_{\rm D} = -v_\phi \sin\phi \sin i + v_{\rm p} \cos\phi \cos\vartheta \sin i + v_{\rm p} \sin\vartheta \cos i, \tag{4.9}$$

where v_ϕ and $v_{\rm p}$ are the azimuthal and poloidal velocities of the wind, respectively.

The first order term in Equation (4.8) involves the shear velocity $v_{\rm sh}$, defined as $v_{\rm sh} = l_{\rm em} Q \cos\beta/\cos\iota$, where Q (Rybicki & Hummer 1978, 1983) is the line-of-sight gradient of the line-of-sight wind velocity:

$$Q \equiv \hat{\mathbf{n}} \cdot \mathbf{\Lambda} \cdot \hat{\mathbf{n}}, \tag{4.10}$$

where $\hat{\mathbf{n}}$ is the unit vector in the LOS direction. The entries of the strain tensor Λ consist of spatial derivatives of velocity components. It is symmetric ($\Lambda_{ij} = \Lambda_{ji}$) and its

elements are given in cylindrical coordinates by (see e.g., Batchelor 1967):

$$\Lambda_{r\phi} = \frac{1}{2}\left(\frac{1}{r}\frac{\partial v_r}{\partial \phi} - \frac{v_\phi}{r} + \frac{\partial v_\phi}{\partial r}\right), \quad \Lambda_{rz} = \frac{1}{2}\left(\frac{\partial v_r}{\partial z} + \frac{\partial v_z}{\partial r}\right),$$
$$\Lambda_{\phi z} = \frac{1}{2}\left(\frac{\partial v_\phi}{\partial z} + \frac{1}{r}\frac{\partial v_z}{\partial \phi}\right),$$
$$\Lambda_{rr} = \frac{\partial v_r}{\partial r}, \quad \Lambda_{\phi\phi} = \frac{1}{r}\frac{\partial v_\phi}{\partial \phi} + \frac{v_r}{r}, \quad \Lambda_{zz} = \frac{\partial v_z}{\partial z}. \tag{4.11}$$

In terms of these Λ_{ji}, the quantity Q is:

$$Q = \sin^2 i \left[\Lambda_{rr}\cos^2\phi + \Lambda_{\phi\phi}\sin^2\phi - 2\Lambda_{r\phi}\sin\phi\cos\phi\right] + \cos i \left[2\Lambda_{rz}\sin i\cos\phi + \Lambda_{zz}\cos i - 2\Lambda_{\phi z}\sin i\sin\phi\right]. \tag{4.12}$$

Note that Hall et al. (unpublished) corrected the sign error in front of the term multiplied by $\cos i$ in the Murray & Chiang (1997) definition of Q. This error was independently found and corrected by Flohic et al. (2012).

Assuming azimuthal symmetry, all the $\partial/\partial\phi = 0$ and the simplified expressions for the different Λ_{ij} are:

$$\Lambda_{r\phi} = \frac{1}{2}\left(\frac{\partial v_\phi}{\partial r} - \frac{v_\phi}{r}\right), \quad \Lambda_{rz} = \frac{1}{2}\left(\frac{\partial v_r}{\partial z} + \frac{\partial v_z}{\partial r}\right),$$
$$\Lambda_{\phi z} = \frac{1}{2}\frac{\partial v_\phi}{\partial z}, \quad \Lambda_{rr} = \frac{\partial v_r}{\partial r}, \quad \Lambda_{\phi\phi} = \frac{v_r}{r}, \quad \Lambda_{zz} = \frac{\partial v_z}{\partial z}. \tag{4.13}$$

In the above, the novel element introduced in Hall et al. (unpublished) is the dropping of the assumption of $v_r \ll v_\phi$, thus allowing for non-negligible radial and vertical velocities.

Including that and several factors that have been omitted or considered negligible in the original MC97 work, the final expression for the specific luminosity in a line of

central frequency ν_0 emitted from a disc with a disc wind is given by

$$L_\nu(i) = \int_{r_{\min}}^{r_{\max}} S_\nu(r)\, a(r)\, r\, dr \int_0^{2\pi} \cos\iota(r,\phi,i) \times \\ (1 - \exp[-\tau(r,\phi,i) \times e_\nu(r,\phi,i) \times e^{-x_\nu^2(r,\phi,i)}])\, d\phi \tag{4.14}$$

where

$$\tau(r,\phi,i) \equiv \frac{ck_0(r)/2\nu_0}{\sqrt{Q^2(r,\phi,i) + q_{\rm tt}^2(r,\phi,i)}} \tag{4.15}$$

$$e_\nu(r,\phi,i) \equiv \text{ erfc}\left(-\frac{\nu - \nu_{\rm D}(r,\phi,i)}{\sqrt{2}\Delta\nu_{\rm tt}\sqrt{1 + q_{\rm tt}^2(r,\phi,i)/Q^2(r,\phi,i)}}\right) \tag{4.16}$$

$$x_\nu^2(r,\phi,i) \equiv \frac{1}{2}\left(\frac{\nu - \nu_{\rm D}(r,\phi,i)}{\Delta\nu_{\rm tt}\sqrt{1 + Q^2(r,\phi,i)/q_{\rm tt}^2(r,\phi,i)}}\right)^2 \tag{4.17}$$

and erfc is the complementary error function. The quantity $k_0(r)$ in expression (4.15) is the integrated line opacity (in units of Hz/cm) at $z_{\rm em}$. The two additional quantities included in expressions (4.15)-(4.17) are the Doppler-shifted central frequency of the line emitted towards the observer from location (r,ϕ) on the emitting surface, defined by $\nu_{\rm D} = \nu_0(1 + v_{\rm D}/c)$, and the 'thermal Q', the ratio of the characteristic thermal plus turbulent velocity of the ion to the thickness of the emitting layer along the LOS, $q_{\rm tt}(r,\phi,i) = v_{\rm tt}\cos\iota(r,\phi,i)/l_{\rm em}(r)\cos\beta(r)$, with $v_{\rm tt}^2 \equiv v_{\rm th}^2 + v_{\rm turb}^2$. The z-dependent quantities are evaluated at $z = z_{\rm em}$ where applicable. The emission region thickness is

assumed to be

$$l_{\rm em}(r) = 0.1\, z_{\rm em} \left[\frac{v_{\rm tt} + v_{\rm p}(r, z_{\rm em})}{v_{\rm tt} + v_{\infty}(r, z_{\rm em})} \right]. \tag{4.18}$$

The above expression differs slightly from that given in MC97, which lacked the factor of 0.1 in front and the $v_{\rm tt}$ terms in the quotient. Our expression ensures that the thickness $l_{\rm em}$ of the emission region is appreciably less than its height $z_{\rm em}$ even when ϑ is large or when the wind has finished accelerating before reaching the emission region ($v_{\infty} = v_{\rm p}$). Our expression also ensures that the thickness can shrink dramatically in a rapidly accelerating wind with $v_{\infty} \gg v_{\rm p} \gg v_{\rm tt}$. A rapidly accelerating wind will have a rapid drop-off in density, decreasing the size of the region in which line emission is efficient.

Even in the ideal MHD case that we consider in this work, the flow variables that represent the solution of the problem are found, in the general case, by solving a second-order differential equation $\xi'' = \xi''(\chi, \xi, \xi', f(\chi))$, with $f(\chi)$ given implicitly by Equation (3.85). However, by using the EBS92 model we could evaluate f', m and g' from an analytic estimate for f. The point of having used an analytical functional form for $f(\chi)$ has to do with the inclusion of the velocity field in the MC97 model. The opacity depends on the projection of the LOS component of the gradient of the LOS velocity through the quantity Q (Equation (4.12)), which involves the spatial derivatives of velocity components. Combining the EBS92 functional form for $\xi(\chi)$ and $\xi_{\rm A} = \lambda^{0.5}$ it is straightforward to obtain $\chi_{\rm A} = (\lambda - 1)c_2$. In the general case this quantity must be found numerically as part of the solution. However, in the adopted framework, all related

quantities at the Alfvén point are easily found (because $m_{\rm A} = 1$). In particular,

$$f_{\rm A} = \frac{1}{\kappa\sqrt{\lambda}J_{\rm A}} = \frac{1}{\kappa\sqrt{\lambda}[\xi(\chi_{\rm A}) - \chi_{\rm A}\xi'(\chi_{\rm A})]}. \tag{4.19}$$

The derivative of $f(\chi)$ at $\chi = 0$, $f'(\chi = 0) = f'_0$, is given by BP82 (their Equation (2.23c)), reproduced here:

$$f'_0 = \frac{(3\xi'^2_0 - 1)^{1/2}}{\kappa^2\left[(\lambda-1)^2 + (1+\xi'^2_0)\right]^{1/2}}\ . \tag{4.20}$$

We thus adopt

$$f(\chi) = f_\infty \frac{e^{k_1\chi} - 1}{e^{k_1\chi} + k_2} \tag{4.21}$$

and look for k_1 and k_2 such that the conditions for $f_{\rm A}$ and f'_0 are satisfied. Once $f(\chi)$ is found, $m(\chi)$ and thus $g(\chi)$ are obtained. We then have the three wind velocity components expressed in analytical form.

Note that, as already mentioned, the EBS92 model postulates that the emission lines arise in clouds confined by a MHD flow. However, we follow MC97 and Murray & Chiang (1998, MC98 hereafter) in assuming that the lines form in a continuous medium. As will be discussed in section 5.1, we consider line emissivity obtained by the CLOUDY photoionization model, that differs from either of the emissivity laws adopted by EBS92. Two of those emissivity models include electron scattering, which is not currenlty considered in our model. In EBS92 the dimensionless angular momentum λ and the launch angle are fixed, while in our work the former is still fixed but the latter is varied to study

its effect on the profiles. It is important to note that, while EBS92 obtain the line luminosity integrating in the two poloidal variables, we include the z-integral in the optical depth expression.

4.1 Determination of Q for self-similar MHD winds

For self-similar solutions of MHD winds, the derivatives needed to obtain the different Λ_{ij} that appear in the quantity Q have to be evaluated using the rules for changing variables (e.g., Königl 1989)

$$\frac{\partial}{\partial r} = \frac{1}{J}\frac{\partial}{\partial r_0} - \frac{\chi}{r_0 J}\frac{\partial}{\partial \chi}, \tag{4.22}$$

$$\frac{\partial}{\partial z} = -\frac{\xi'}{J}\frac{\partial}{\partial r_0} + \frac{\xi}{r_0 J}\frac{\partial}{\partial \chi}, \tag{4.23}$$

where $J(\chi)$ has been defined in Equation ((3.77)). Thus, we have the following expressions, where for clarity we omit the functional dependence of the dependent variables:

$$\Lambda_{rr} = -\frac{1}{J}\sqrt{\frac{GM}{r_0^3}}\left(\frac{\xi' f}{2} + \chi\left(\xi'' f + \xi' f'\right)\right) \tag{4.24}$$

$$\Lambda_{\phi\phi} = \sqrt{\frac{GM}{r_0^3}}\,\frac{\xi' f}{\xi} \tag{4.25}$$

$$\Lambda_{zz} = \frac{1}{J}\sqrt{\frac{GM}{r_0^3}}\left(\frac{\xi' f}{2} + \xi f'\right) \tag{4.26}$$

$$\Lambda_{rz} = \frac{1}{2J}\sqrt{\frac{GM}{r_0^3}}\left[\left(\frac{\xi'^2}{2} + \xi\xi'' - \frac{1}{2}\right) f + \left(\xi\xi' - \chi\right) f'\right] \tag{4.27}$$

$$\Lambda_{r\phi} = \frac{1}{2}\sqrt{\frac{GM}{r_0^3}}\left[-\frac{1}{J}\left(\frac{g}{2} + \chi g'\right) + \frac{g}{\xi}\right] \tag{4.28}$$

$$\Lambda_{\phi z} = \frac{1}{2J}\sqrt{\frac{GM}{r_0^3}}\left(\frac{\xi' g}{2} + \xi g'\right) \tag{4.29}$$

For the particular form of $\xi(\chi)$ given by EBS92 the corresponding expressions for the strain tensor entries are:

$$\Lambda_{rr} = -\sqrt{\frac{GM}{r_0^3}}\ \left[\frac{f c_2 + 2\chi^2 f' + 2\chi f' c_2}{2\left(\chi + c_2\right)\left(\chi + 2c_2\right)}\right] \tag{4.30}$$

$$\Lambda_{\phi\phi} = \sqrt{\frac{GM}{r_0^3}}\ \left[\frac{f}{2(\chi + c_2)}\right] \tag{4.31}$$

$$\Lambda_{zz} = \sqrt{\frac{GM}{r_0^3}}\ \left[\frac{f + 4f'\left(\chi + c_2\right)}{2(\chi + 2c_2)}\right] \tag{4.32}$$

$$\Lambda_{rz} = \sqrt{\frac{GM}{r_0^3}}\left[\frac{4\left(\chi + c_2 - 2c_2\chi^2 - 2c_2^2\chi\right)f' - \left(1 + 4c_2\chi + 4c_2^2\right) f}{8\sqrt{c_2}\left(\chi + 2c_2\right)\sqrt{\chi + c_2}}\right] \tag{4.33}$$

$$\Lambda_{r\phi} = -\sqrt{\frac{GM}{r_0^3}}\sqrt{c_2}\left[\frac{(2\chi + 3c_2)g + 2\chi(\chi + c_2)g'}{2\left(\chi + 2c_2\right)\sqrt{\chi + c_2}}\right] \tag{4.34}$$

$$\Lambda_{\phi z} = -\sqrt{\frac{GM}{r_0^3}} \left[\frac{g + 4g'\chi + 4g'c_2}{4\left(\chi + 2c_2\right)} \right] \tag{4.35}$$

4.2 Chapter Summary

This chapter describes in detail the final model that we used to evaluate the line emission profiles, that is a combination of two preexistent models. Here we presented the modifications made by Hall et al. (unpublished) to the original MC97 model, in particular the concepts of local inclination angle and thermal Q. The first is a geometrical feature that accounts for the different effective inclinations to the LOS of different portions of the emitting region. The thermal Q is defined as the ratio of the characteristic (i.e., thermal plus turbulent) velocity of the ion of interest to the thickness of the emitting layer along the LOS.

We presented an analytical functional form to describe the MHD velocity field included in the model and showed detailed evaluation of $Q \equiv \hat{\mathbf{n}} \cdot \mathbf{\Lambda} \cdot \hat{\mathbf{n}}$ (LOS gradient of the LOS projection of the wind velocity) specific for that velocity field. The elements defined in this chapter were applied to implement the code that built the line profiles shown in the next chapters.

5 Fiducial Case

In this chapter we apply the formalism shown in the previous chapter to evaluate the C IV λ 1549 line luminosity assuming a set of fiducial parameters, summarized in Table 5.2. Furthermore, following the approach of Fine et al. (2008, 2010) and observational data from the latter, we use the scatter of our line-width distribution to obtain constraints on the obscuring structure geometry that surrounds the central engine in AGN unification paradigm. We considered three different possibilities for this obscuring structure: smooth and clumpy torii and a warped accretion disc.

The transition considered, due to $^2P^{\rm o}$-^2S transitions of the the Li-like ion C^{3+}, is one of the most prominent features in AGN spectra, together with many other doublet resonance lines of the Li isoelectronic series, such as O VI λ 1035, N V λ 1240, Si IV λ 1400, etc (e.g., Netzer 2013).

Table 5.1 summarizes some data of the C IV λ 1549 transition: wavelengths, excitation potential of the upper level E_k (k = 2, 3), spontaneous-transition probabilities A_{k1},

λ	$E_{\rm k}$	$A_{\rm k1}$	$f_{\rm 1k}$
Å	eV	10^8 s^{-1}	
1548.20	8.008	2.65	0.190
1550.77	7.995	2.64	0.095

Table 5.1: C IV λ 1549 transition data.

and oscillator strength f_{1k}, taken from the NIST [6] database:

`http://physics.nist.gov/asd`

5.1 Line Profiles

We evaluated the line luminosity (Equation (4.14)) using the EBS92 solution to estimate the quantities included there and in the associated equations (4.15) and (4.17). In summary, $v_{\rm D}$ and Q are computed as functions of position (r, ϕ, z) from the velocity field given by the EBS92 model. Then, these two quantities and the 'thermal Q', $q_{\rm tt}$, are used to evaluate the optical depth $\tau(r, \phi, i)$ (Equation (4.15)) and the quantities $e_\nu(r, \phi, i)$ (Equation (4.16)) and $x_\nu(r, \phi, i)$ (Equation (4.17)). We emphasize again that the integral in the z direction is included in the optical depth expression. We then calculate $L_\nu(\hat{\mathbf{n}})$ by integrating over all (r, ϕ) (Equation (4.14)). The process is repeated for different ν values

[6] National Institute of Standards and Technology

to build up the profile of the given emission line for the given input parameters. In the numerical integrations we tested for numerical convergence by increasing the number of azimuthal and radial bins until the change between a realization and the next was smaller than a pre-specified value.

We computed the C IV line profile for different combinations of inclination angle, i and initial angle, ϑ_0. We also studied the results of changing the initial density (i.e., the density at the disc plane) and the exponent of the power law that governs the radial behaviour of the density. The specific luminosity from each component of the C IV doublet is computed separately, and then the results added together. In Table 5.2 we list the meaning and adopted values of the main parameters in the model. The BH mass is expressed in units of solar masses (1 $M_{\odot} = 1.9891 \times 10^{33}$ g). The fiducial values adopted for the density, density power-law exponent and thermal plus turbulent velocity are $n_0 = 10^{11}$ cm^{-3}, $b = 2$ and $v_{\rm tt} = 10^7$ cm s^{-1}, respectively.

Most of the work shown in this chapter has been published in Chajet & Hall (2013). However, in continuing to work on the model after publication, it was realized that there was a mistake in the points considered in the interpolation routine of the source function and the new results reflect that fix. Although the old results showed the right trend, many of the limits inferred from them were too stringent and were slightly in tension with other works.

Variable	Value	Explanation
$M_{\rm BH}$	$10^8\ M_\odot$	Black hole mass
$L_{\rm UV}$	10^{46} erg s^{-1}	Quasar ionizing luminosity
$S_\nu(r)$	CLOUDY results	Source function
$r_{\rm min}$	$2\sqrt{\frac{L_{\rm UV}}{10^{46}\text{erg s}^{-1}}} \times 10^{15}$ cm	Inner BELR radius
$r_{\rm max}$	$2\sqrt{\frac{L_{\rm UV}}{10^{46}\text{erg s}^{-1}}} \times 10^{19}$ cm	Outer BELR radius
n_0	$10^6 - 10^{13}$ cm^{-3}	Hydrogen number density at $r_{\rm min}$
b	0.5, 1, 2	Exponent in $n(r) \propto r^{-b}$
i	$5^\circ - 75^\circ$	Observer inclination angle
ϑ_0	5°, 10°, 15°, 30°, 45°, 57°	Streamline launch angle
$\tan\beta(r)$	0.1051	$z_{\rm em} = r\tan\beta(r) = r\tan(6^\circ)$
$v_{\rm tt}$	$10^6 - 10^7$ cm s^{-1}	Thermal+turbulent speed of ion.
χ_i	solar	Abundance of element, see Equation (4.5)
η_i	1	Ionization fraction of ion, see Equation (4.5)
λ	10	Specific angular momentum

Table 5.2: Set of parameters used in the simulations. In Chapter 6, where we evaluate the line luminosity for a set of different mass and luminosity combinations, we present scaling of the inner and outer radii that takes into account both parameters.

5.1.1 Source Function

The source function is defined as $S_\nu = j_\nu/k_\nu$, where j_ν and k_ν are the emission and absorption coefficients respectively. As in the case of many other bound-bound transitions, the coefficients j_ν and k_ν corresponding to the C IV transition have similar frequency dependences, such that $S_\nu(r)$ can be considered independent of frequency, i.e., $S_\nu(r) = S(r)$.

We determine the source function for our simulations by applying the RM results of Kaspi et al. (2007) to the radial line luminosity function $L(r)$ calculated by MC98 for a quasar with L_{1350}[7] $\equiv \nu L_\nu(1350\ ) = 10^{46}\,\mathrm{erg\,s^{-1}}$ and shown in their Figure 5b. According to that figure, the peak C IV emission is reached at $R_{\rm CIV} = 10^{18}\,\mathrm{cm}$, but the Kaspi et al. (2007) results show that $R_{\rm CIV}$ is smaller for a quasar of that luminosity. Their Equation (3) gives

$$R_{\rm CIV} = 6.216 \times 10^{15}\ \mathrm{cm} \left(\frac{L_{1350}}{10^{43}\ \mathrm{erg\,s^{-1}}} \right)^{\alpha}, \tag{5.1}$$

where $\alpha = 0.55 \pm 0.04$ in the original formulation and for simplicity we have adopted $\alpha = 0.5$. Equation (5.1) gives $R_{\rm CIV} = 2 \times 10^{17}$ cm for a quasar with $L_{1350} = 10^{46}\,\mathrm{erg\,s^{-1}}$. We therefore empirically adjust all the radii in the MC98 Figure 5b line luminosity function down by a factor of five. Each point in the line luminosity function now gives the line luminosity $L(r_i)$ in a logarithmic bin spanning a factor of $\sqrt{10}$ in radius centred on

[7] In what follows we will use $L_{\rm UV}$ and L_{1350} interchangeably.

adjusted radius r_i for a quasar with $L_{1350} = 10^{46}\,\mathrm{erg\,s^{-1}}$. The RM-corrected data points were interpolated by means of a cubic spline function, as shown in Figure 5.1.

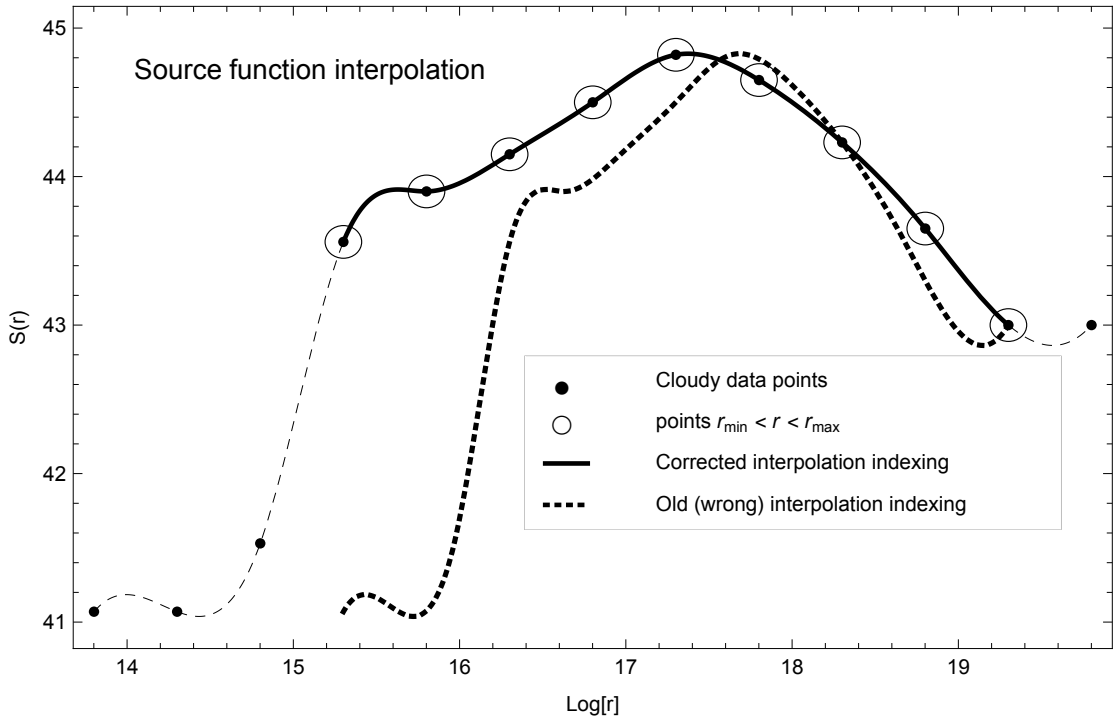

Figure 5.1: Source function $S(r)$ versus radius. The black line shows the cubic spline interpolation through all data points (shown also in black) taken from the MC98 CLOUDY (Ferland 1993) simulations. The points that lie within the range $r_{\min} \leq r \leq r_{\max}$ are encircled and the solid line represents the region of the interpolation within those limits, which is the region used in the simulations. The dotted line shows the interpolation based on the original (wrong) interpolating point indexing, whereby the point corresponding to $r_{\min}$ was linked to the first data point.

5.1.2 Optical Depth Effects

In Chapter 2 we mentioned that a disc wind model accounts for the BEL single peaked signature because the opacity of the outflowing gas is anisotropic. In Chapter 4 we described our model, that incorporates the modificatons to the MC97 model introduced by Hall et al. (unpublished). The line luminosity is given by Equation (4.14). We can study the behaviour of the azimuthal integrand $1 - e^{-\tau_\nu}$, with $\tau_\nu = \tau\ e_\nu\ e^{-x_\nu^2}$, where $\tau = \tau(r, \phi, i)$ and $x_\nu^2(r, \phi, i)$ are defined in Equations (4.15) and (4.17) espectively. Note that τ is independent of ν, while x_ν depends on the frequency. The integral involving the complementary error function that is part of the definition of τ_ν above, Equation (4.16), can be approximated as being from 0 to ∞, which yields $\sqrt{\pi}/2 \approx 1$ (e.g., MC97).

Three zones can be identified: $\tau_\nu \ll 1$, $\tau_\nu \sim 1$ and $\tau_\nu \gg 1$. In the first and last cases, the resulting emission is independent of the azimuth, with $L \sim 0$ when $\tau_\nu \ll 1$, and $L \propto S$ when $\tau_\nu \gg 1$. In the intermediate zone the emission is azimutally anisotropic. The condition there is equivalent to $\ln \tau \sim x_\nu^2$. Note that it imposes that the line should be optically thick, i.e., $\tau \geqslant 1$, as $x^2 \geqslant 0\ \forall\ x$.

For a given set of r, i, ϑ_0 and ν, the azimuthal integrand would then be nonegligible in a small range around the angles that are the two solutions in ϕ to the equation

$$\ln \tau^2 = \left[\frac{\nu - \nu_0(1 + v_\mathrm{D}/c)}{\Delta\nu_\mathrm{tt}\sqrt{1 + Q^2/q_\mathrm{tt}^2}} \right]^2 . \tag{5.2}$$

Thus, at a given frequency, only certain regions of a rotating disc wind can contribute to

the disc emissivity, and the line emission will predominantly arise from azimuthal angles within a narrow range around the solutions of the equation (5.2).

Figure 5.2 shows how the quantity $\tau(i, r, \phi)$ varies on the BLR region for different combinations of viewing and launching angles.

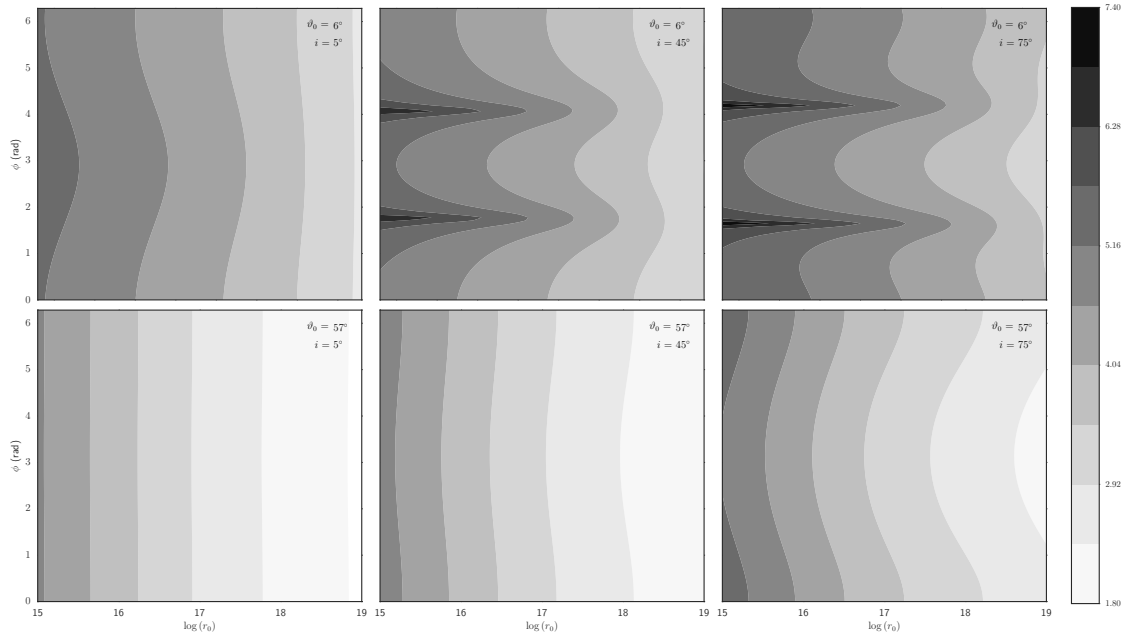

Figure 5.2: Contour map of $\tau(r, \phi, i)$ for different combinations of viewing and wind launching angle. These maps represent the frequency-independent part of the total optical depth. As discussed in the text, for a given ν, the total disc emissivity of a model with a wind will have contributions from a narrow azimuthal range around each of the ϕ values that satisfy Equation (5.2).

5.1.3 Different v_{th}

For a thermal velocity of $v_{\rm th} = 10^6$ cm s^{-1} and no turbulence, the profiles of the individual components of the doublet are very narrow, (FWHM [8] < inter-component separation) for small inclination angles. As a result, the combined profiles are double- (or multiple-) peaked. The effect is less pronounced for higher ($\gtrsim 45°$) i values.

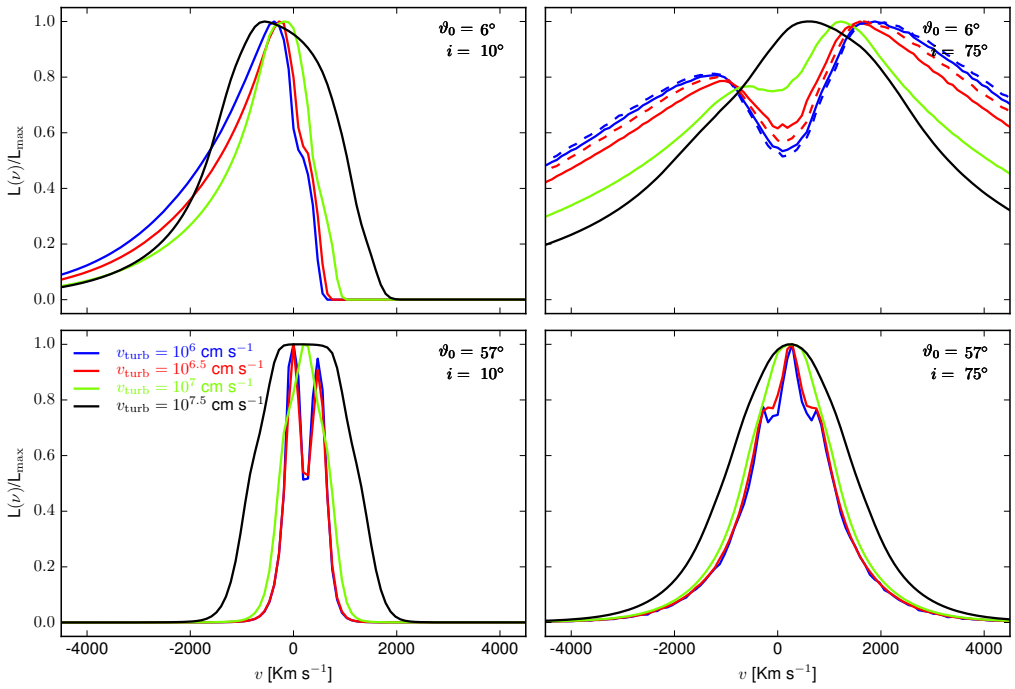

Figure 5.3: $L_\nu/L_{\rm max}$ versus velocity for four different values of the thermal plus turbulent velocity: $v_{\rm turb} = 10^6, 10^{6.5}, 10^7, 10^{7.5}$ cm s^{-1} and two different inclination angles: $i = 10°$ (left panels) and $i = 75°$ (right panels). Upper panels correspond to $\vartheta_0 = 6°$ and lower panels, to $\vartheta_0 = 57°$. The initial density is $n_0 = 10^{11}$ cm^{-3} in all cases. The two extra curves shown in the upper right panel correspond to $v_{\rm turb} = 10^{5.8}$ cm s^{-1} (dashed blue) and $10^{6.2}$ cm s^{-1} (dashed red).

[8] FWHM: Full Width at Half-Maximum

These results suggested considering different velocities by incorporating the effect of turbulence. Bottorff & Ferland (2000) studied how microturbulence can affect the lines and showed that it affects more the far UV lines. Figure 5.3 shows the lines corresponding to four different values of $v_{\rm turb}$, for two different inclination angles, $i = 10^{\circ}$ (left panels) and $i = 75^{\circ}$ (right panels). The profiles in the upper row correspond to $\vartheta_0 = 6^{\circ}$ and in the lower row, to $\vartheta_0 = 57^{\circ}$. In general, the lines become smoother and more symmetric with increasing $v_{\rm turb}$. A much higher $v_{\rm turb}$ does make a noticeable difference, as expected. However, note that the upper right panel seems to represent an anomalous situation, as the profiles become narrower as the turbulent velocity increases.

To investigate the apparently anomalous situation, in the upper right corner of Fig. 5.4 we plotted the same profiles as above, but normalized to the values corresponding to our fiducial turbulent velocity (10^7 cm s^{-1}). Note that in all cases, even in the apparently deviant case, the flux increases when the turbulent velocity does. The fact, as shown in the upper right plot, that in the low-ϑ_0-high i combination the line profile becomes stronger but narrows as the total velocity (thermal plus turbulent) increases might be consistent with a photon escape probability increase larger in the radial direction than in the tangential. And the reason that only that particular launch and viewing angle combination is affected is related to the fact that, under this condition, the streamlines intersect the base of the emission region at larger radii (due to the small ϑ_0) and the

projection onto the LOS is mostly radial (because of the large i). Another way to explore the narrowing of the line profile when the turbulent velocity is increased could be to analyse annuli of increasing radii (and, therefore, increasing emitting area), to trace how different portions of the emission region contribute to the line formation.

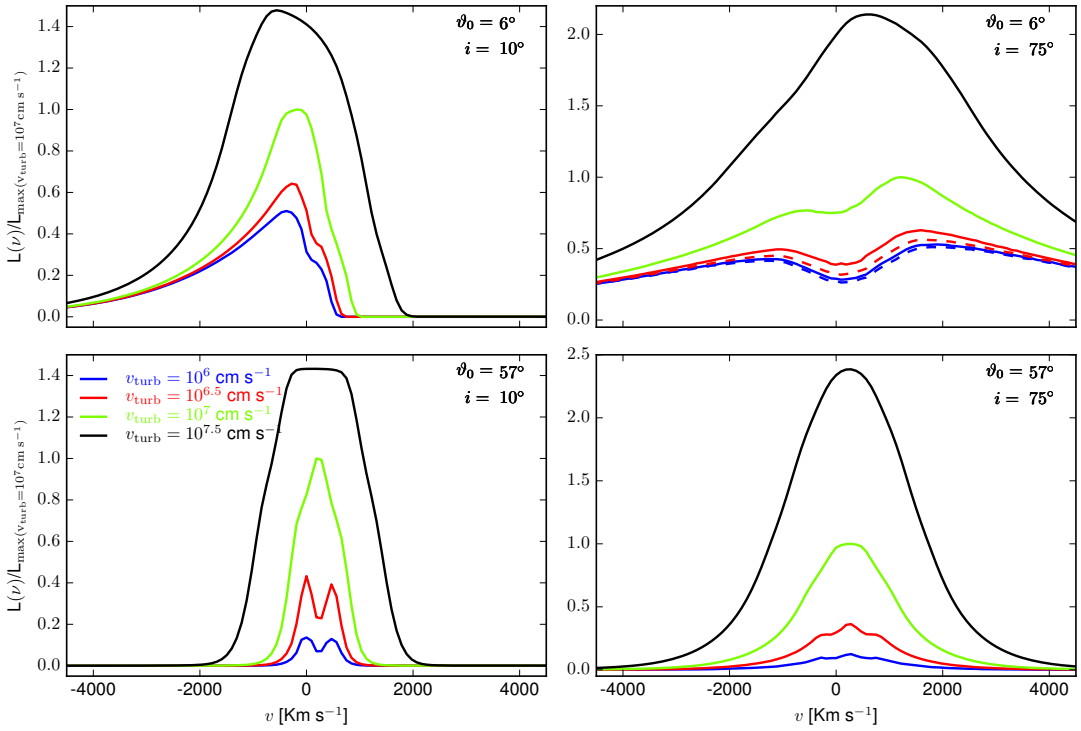

Figure 5.4: $L_\nu / L_{\rm max}(v_{\rm turb} = 10^7$ cm s$^{-1})$ versus velocity for four different values of the thermal plus turbulent velocity: $v_{\rm turb} = 10^6, 10^{6.5}, 10^7, 10^{7.5}$ cm s^{-1} and two different inclination angles: $i = 10°$ (left panels) and $i = 75°$ (right panels). Upper panels correspond to $\vartheta_0 = 6°$ and lower panels, to $\vartheta_0 = 57°$.

5.1.4 Changing inclination angle at fixed launch angle

For the fiducial values of density ($n_0 = 10^{11}$ cm^{-3}) and turbulent velocity ($v_{\rm turb} = 10^7$ cm s^{-1}), we studied the effect(s) of changing the launch and viewing angles, in the ranges $\vartheta_0 = 5^\circ$- 57° and $i = 10^\circ$- 75°, respectively. The results are shown in Figures 5.5 and 5.6.

In each panel of Figure 5.5 the profiles are plotted versus velocity for a given launch angle, to enhance the effect of changing the viewing angle. Zero velocity is the average of the two doublet wavelengths. The velocities plotted represent velocities from the observer's point of view, therefore negative velocities correspond to blueshifts. In all cases the profiles are slightly asymmetric, with increasing degree of asymmetry with decreasing inclination. The blue wings change less than the red wings, so that as the inclination angle approaches smaller values, the red wings are increasingly weaker. In Figure 5.5, the effect is hard to notice for the lowest ϑ_0 (the two upper panels), due to the shift to the red in the peak of the profiles when the inclination increases. We will discuss the effect of launch angle dependency below.

A way to see this is by noting that, for a given launch angle, when the object is seen face-on, the projection of the velocity into the LOS is towards the observer for any azimuthal angle, while for objects seen edge-on, that projection is towards the observer for part of the emitting region, and receding from them for the rest. For intermediate

cases, the closer the object's LOS is to the face-on case, the more the red wing of its profile is weakened, explaining why the lines are less symmetric for smaller inclination angles.

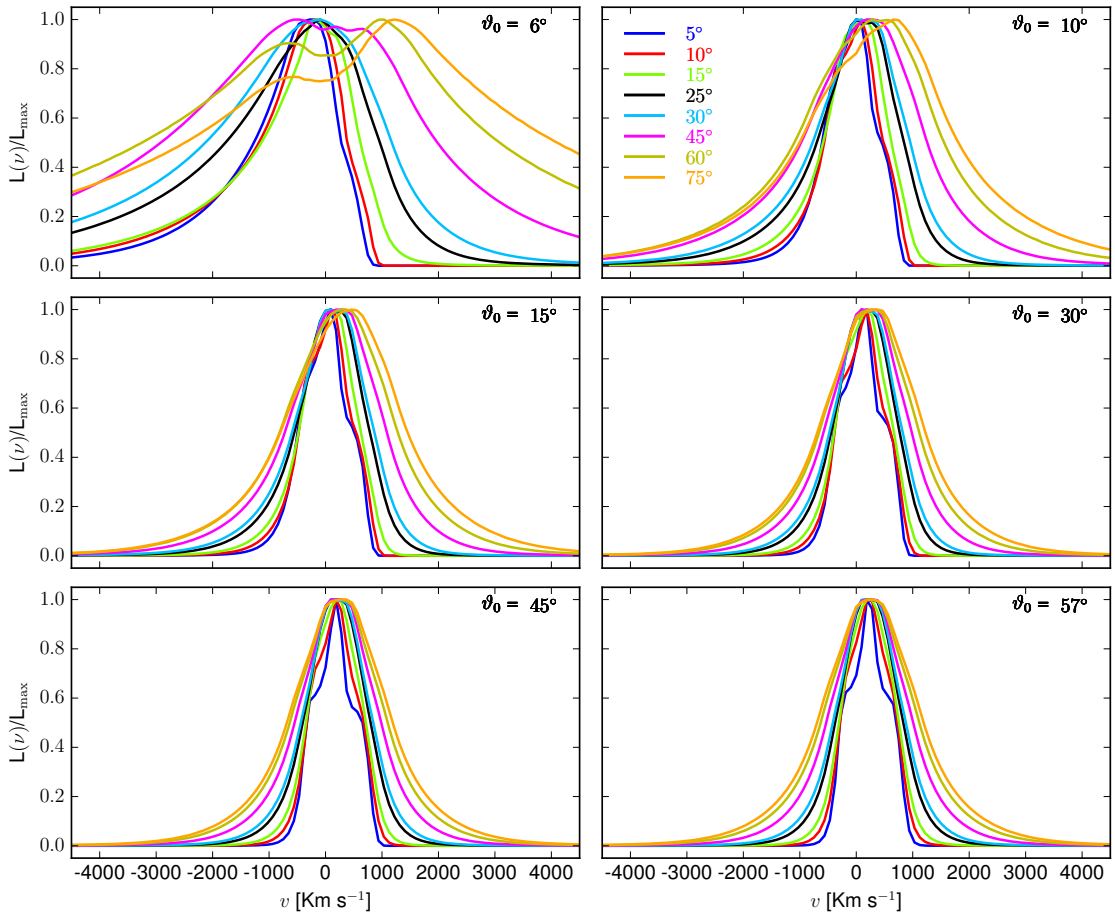

Figure 5.5: $L_\nu/L_{\max}$ versus velocity for $i = 5° - 75°$. Looking clockwise from the upper left: $\vartheta_0 = 6°, 10°, 15°, 30°, 45°, 57°$. The last two cases do not differ significantly.

5.1.5 Changing launch angle at fixed inclination angle

The effects of changing the launch angle ϑ_0 are shown in Figure 5.6, where in each panel we have plotted the profiles for a given inclination angle and different launch angles. The actual angle to be considered is the angle ϑ at which a line launched with some ϑ_0 crosses the base of the emitting region (when ϑ_0 increases, so does ϑ). For instance, for our chosen value of $\tan\beta$, for $\vartheta_0 = 20°$, $\vartheta \sim 25.82°$ and for $\vartheta_0 = 45°$, $\vartheta = 48°$

When ϑ_0 increases, the projection of the wind velocity onto the LOS is towards the observer in a portion of the emission region (i.e., for some azimuths) and is also towards the observer in the rest of the region as long as $\vartheta > i$. In the cases $\vartheta < i$, that projection is receding from the observer.

As the wind velocity decreases with increasing ϑ_0, so does the magnitude of its projection for given i, and thus the blueshift decreases for increasing ϑ_0. However, it is the Doppler velocity, including a contribution from the rotational velocity, which is the velocity relevant for producing the observed line profiles. Thus, as the wind velocity decreases with increasing ϑ, then not only is the blueshift reduced, but the rotational velocity is increasingly dominant and the profiles become more symmetric. For any launch angle, the relative importance of the receding term with respect to the approaching term increases with increasing viewing angle, but the effect is larger for smaller ϑ_0.

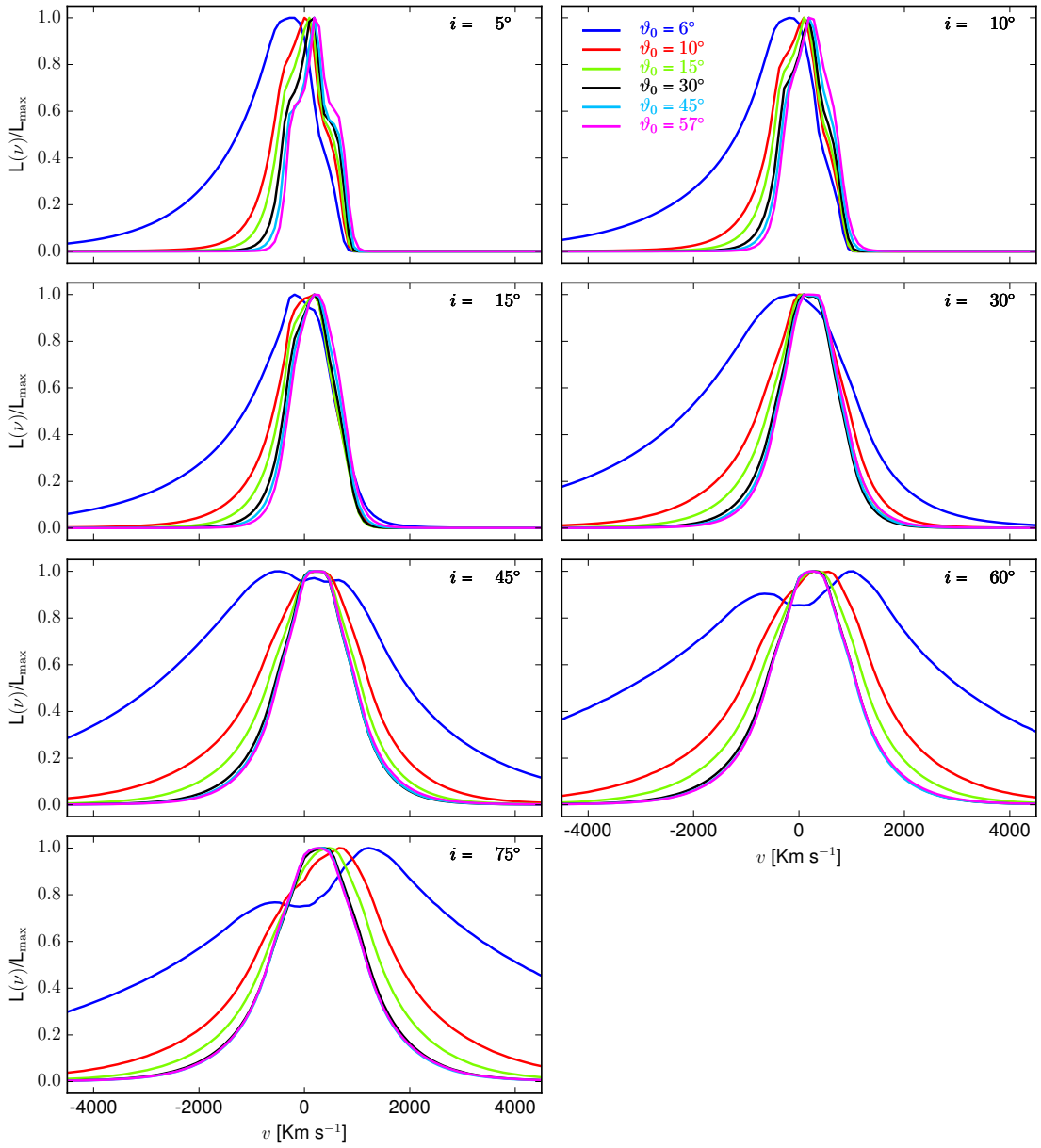

Figure 5.6: $L_\nu/L_{\max}$ versus velocity. In each panel, we have plotted the profiles corresponding to i from 5° to 75° for $\vartheta_0 = 6^\circ - 57^\circ$. For given i, those profiles for which $\vartheta > i$ are bluer, while those corresponding to $\vartheta < i$ are redder. Here, $\vartheta > \vartheta_0$ is the angle between a line launched with some ϑ_0 and the base of the emitting region.

We also analysed how strongly the broadening of the line profile with decreasing ϑ_0 depends on the density profile. Note that, in principle, the smaller ϑ_0 is, the larger the radii at which the streamlines intersect the base of the emission region, that is, these lines will form at radii where the density (that goes as $\sim r^{-b}$) is smaller, affecting the optical depth. To that end, we compared the inverse square power-law to other (less steep) density power-laws ($b = 0.5, 1$) for different launch angles, and found that the dependence is negligible. That is, the broadening found in the small ϑ_0 cases depends mainly on the velocity projection.

In summary, the relevant quantity is a combination of the two angles and not either of them individually. This can also be seen by considering the expression of the optical depth (Equation (4.15)) where the frequency dependence is encompassed in the exponent x_ν, dependent on the Doppler velocity $v_{\rm D}$. The latter includes the wind contribution, which ranges from $v_{\rm p}\sin(\vartheta + i)$ when $\phi = 0$, to $v_{\rm p}\sin(\vartheta - i)$ when $\phi = \pi$. Note also that the FWHM increases with increasing inclination angle (see Fig. 5.5). In the smaller ϑ_0 cases, the broadening and subsequent decrement is accompanied by a shift in the peak, from bluer (at smaller inclinations) to redder velocities (at larger inclinations). This is due to the fact that the observer sees the base of the conical emission region from an almost edge-on perspective, so that the part of the cone with $\phi \simeq 0^\circ$ (which produces blueshifted emission) has a very small projected surface area.

5.1.6 Changing density

We also looked at the effects of varying the initial density. The lower and upper limits for electron density in the BLR are usually estimated on the basis of the absence or presence of some forbidden or semi-forbidden lines. The absence of [O III] $\lambda\lambda$4363, 4959, 5007 lines provides a lower limit to the density in this region. The critical density for collisional de-excitation needed for the transition is $\sim 10^8$ cm^{-3}. On the other hand, the presence of the semi-forbidden line C III] λ1909 provides an upper limit $\sim 10^{11}$ cm^{-3} (e.g., Baldwin et al. 2003, Sulentic et al. 2000). This result is based in RM observations, while previous estimates adopted a smaller value ($\sim 10^{9-9.5}$ cm^{-3}) for this upper limit (e.g., Osterbrock 1989).

Although we adopted $n_0 \sim 10^{11}$ cm^{-3} as the "standard density", we also chose to check the effect of even lower and higher densities. In principle, one would expect broader profiles for smaller initial density. In fact, that is what is found when running simulations that do not include the terms and factors introduced in Hall et al. (unpublished). In that case, the results showed that the profiles become broader as the initial density decreases. In effect, as the density decreases, so does the opacity and, in that case there will be fewer photons absorbed in the line wings and this translates into broader lines. However, the inclusion of these previously neglected terms and factors modifies the behaviour of the profiles, in such a way that the effect of changing the initial den-

sity is much less important (negligible, in some cases). In the current model, the velocity field (which depends on both inclination and launch angles) dictates the optical depth behaviour. This is somewhat similar to the broadening of the low-ϑ_0 case that we discussed above.

Figure 5.7 shows the profiles obtained for a fixed inclination $i = 10^\circ$ (left panels) and $i = 75^\circ$ (right panels) and launch angles $\vartheta_0 = 10^\circ$ (upper panels) and $\vartheta_0 = 57^\circ$ (lower panels) when the initial density, which declines radially according to $n \sim r^{-2}$, is varied. The results of the density analysis also show that for given ϑ_0, the smaller the inclination angle, the bluer the maximum.

The effect of changing the density at the base of the wind was investigated by Everett (2005) for his hybrid model, showing that for density $n_0 < 10^9$ cm^{-3} the continuum was the dominant driving mechanism while for $n_0 = 10^{11}$ cm^{-3} (the highest density tested in that work), line driving dominates over continuum driving at any position in the wind.

5.1.7 Smaller launch angles

The effect of even smaller launch angles is shown in Figure 5.8 for the cases $i = 5^\circ, 30^\circ, 75^\circ$. Included, for comparison, are the profiles for the same inclination angles, but with $\vartheta_0 = 10^\circ$. In the left panel, each profile is normalized with respect to the maximum of the $i = 5^\circ$ profile for each launch angle, whereas in the right panel the

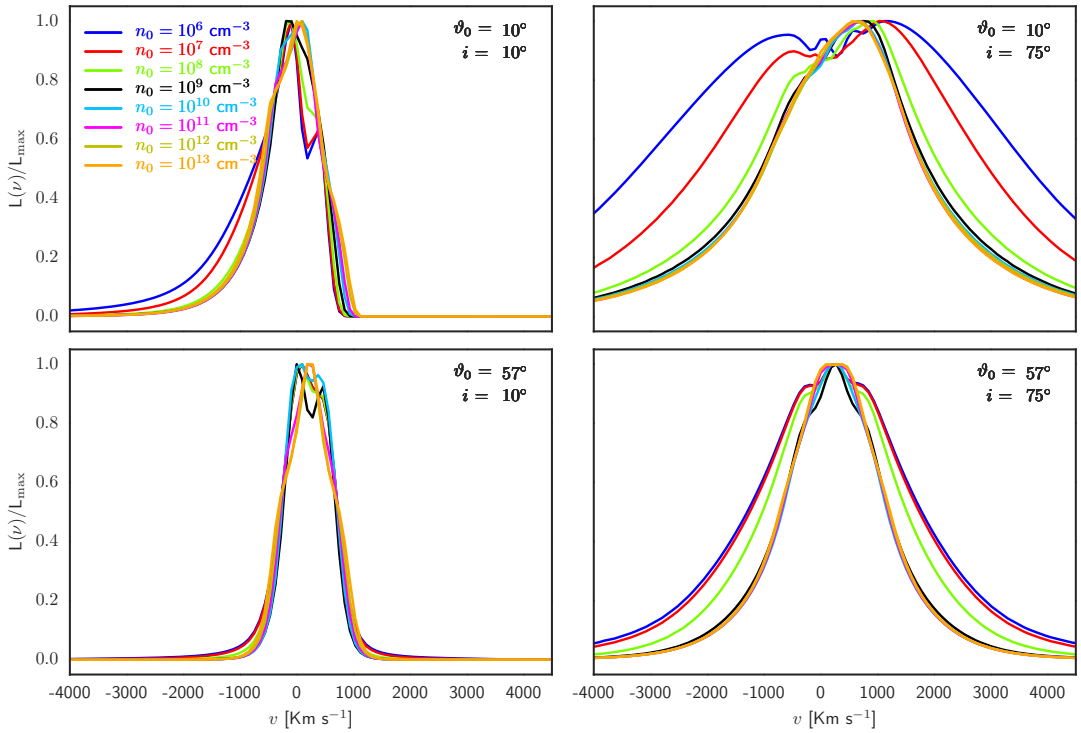

Figure 5.7: $L_\nu/L_{\rm max}$ versus velocity. Here, the profiles correspond to fixed $i \sim 10°$ (left panels) and $i \sim 75°$ (right panels) and $\vartheta_0 = 10°$ (upper panels) and $\vartheta_0 = 57°$ (bottom panels) but different initial densities: $n_0 = 10^6$ cm^{-3} (blue), $n_0 = 10^7$ cm^{-3} (red), $n_0 = 10^8$ cm^{-3} (green), $n_0 = 10^9$ cm^{-3} (black), $n_0 = 10^{10}$ cm^{-3} (cyan), $n_0 = 10^{11}$ cm^{-3} (magenta), $n_0 = 10^{12}$ cm^{-3} (gold) and $n_0 = 10^{13}$ cm^{-3} (orange). The effect of a lower density on the opacity, and thus on the line broadness, is surpassed by the effect of the velocity field, leaving a dependence on density that is a function of i and ϑ_0. For fixed ϑ_0 (i.e., looking along rows) the spread is larger for higher inclination angles, while for fixed i (i.e, looking along columns), it is larger for smaller launch angle, with the trend being more pronounced with decreasing n_0.

normalization is with respect to its own maximum. It can be noticed from the figure that, when the viewing angle is large and $\vartheta_0 = 5°$, the profile is double-peaked, which is not observed in C IV lines.

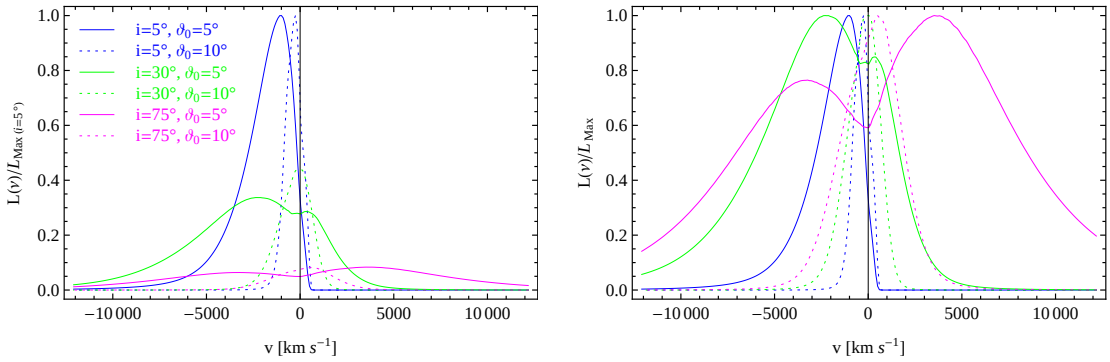

Figure 5.8: Two different normalizations of the profiles for $\vartheta_0 = 5°, 10°$ and $i = 5°, 30°, 75°$. In the left panel, the profiles are normalized to the maximum of the $i = 5°$ profile for the corresponding launch angle. In the right panel, the normalization is with respect to each profile's own maximum.

To study this issue we analysed the evolution of the profiles, for two different inclination angles ($i = 5°, 75°$), when the launch angle changes between $\vartheta_0 = 5°$ and $10°$. Figure 5.9 shows that in both cases, as the launch angle increases the profiles become increasingly narrower. Here we see the same trend shown in Figure 5.6 and discussed in subsection 5.1.5: for smaller launch and viewing angles (left panel), most of the flux is due to motion towards the observer and the blueshift decreases with increasing ϑ_0. For larger i (right panel) the contribution of the receding term of the Doppler velocity dominates but also decreases with increasing ϑ_0, leading to an emission peak that approaches the systemic redshift with increasing ϑ_0. The dashed blue line profile corresponds to $\vartheta_0 = 5°$, $i = 75°$ (i.e., the same launch angle as the solid blue line), obtained with the

original interpolation setting. The fact that this profile has a double-peaked feature suggested that we could impose an empirical restriction on ϑ_0 and consider only those that satisfy the condition $\vartheta_0 \geq 6°$. Note that when using the corrected interpolation region the double peak characteristic is much less noticeable. However, we kept the same minimum launch angle, that is also equal to the adopted tilt of the emission region.

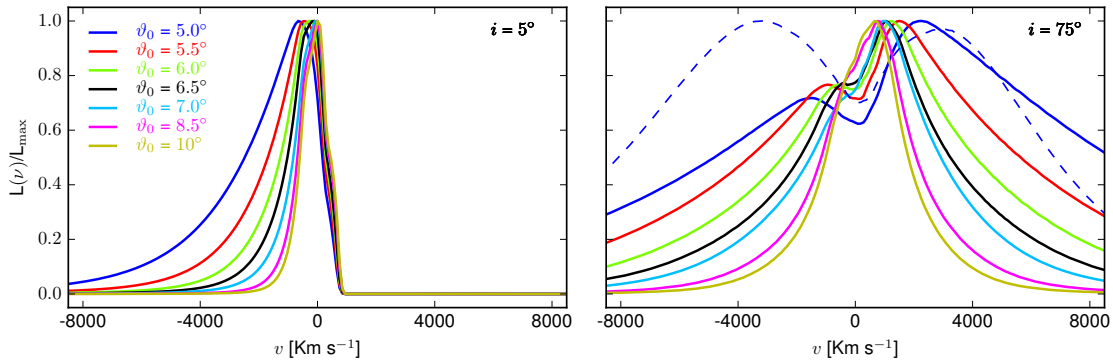

Figure 5.9: Normalized profiles for $\vartheta_0 = 5°$-$10°$ and $i = 5°$ (left panel), $75°$ (right panel). For comparison purposes we included (shown as a dashed blue line) the $\vartheta_0 = 5°$-$i = 75°$ combination line profile obtained with the original (now corrected) interpolation setting.

5.2 Line-Width Measures

From a set of profiles obtained for different inclination angles i and launch angles ϑ_0 we study how the FWHMs are distributed as a function of the angles i at which quasars are visible. To do so, we use an approach similar to that of Fine et al. (2008), who

constrained the range of possible AGN viewing angles by using geometrical models for the BLR and comparing the expected dispersion in linewidths at each viewing angle to their observational data. Figure 5.10 sketches the assumed geometry.

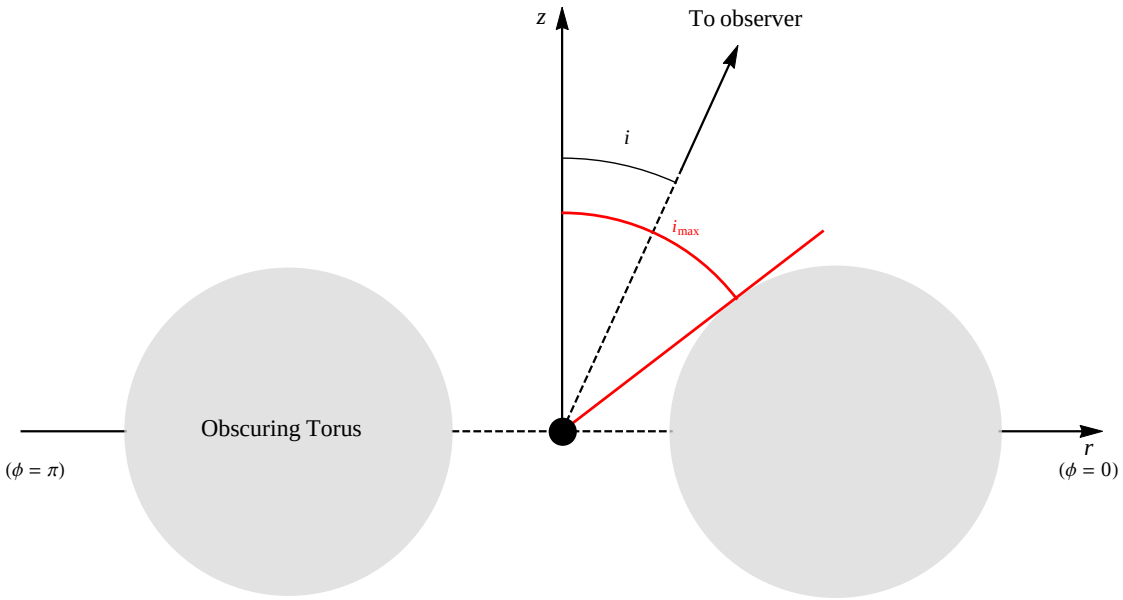

Figure 5.10: AGN geometry. The angle i is the observing angle to the AGN and the opening angle $i_{\rm max}$ is assumed to be constrained by an obscuring torus. Observers whose viewing angle is $< i_{\rm max}$ would be able to detect broad lines and would classify the object as Type 1.

We extended the Fine et al. (2008, 2010) analysis by also considering the clumpy torus model of Nenkova et al. (2008a, 2008b; hereafter N08), as constrained by Mor et al. (2009) using infrared observations of luminous AGN. Figure 5.11 compares this escape probability to the clumpy torus model (e.g., N08) for $i_{\rm max} = 50°$.

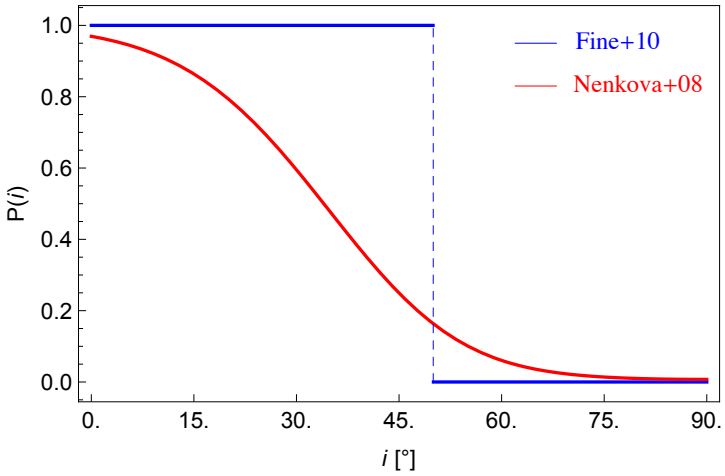

Figure 5.11: Escape probability, evaluated for a given $i_{\max}$, according to the prescriptions adopted by Fine et al. (2008, 2010) (blue) and Nenkova et al. (2008) (red), for $i_{\max} = 50°$.

Fine et al. (2008) measured the linewidth of the Mg II line in 32214 quasar spectra from the Sloan Digital Sky Survey (SDSS) Data Release Five, 2dF QSO [9] Redshift survey (2QZ) and 2dF-SDSS LRG and QSO (2SLAQ) survey and found that the dispersion in linewidths strongly correlates with the optical luminosity of QSOs. Fine et al. (2010) used 13776 quasars from the same surveys to study the dispersion in the distribution of C IV linewidths. In contrast to their findings for Mg II, they found that the dispersion in C IV linewidths is essentially independent of both redshift and luminosity. Figure 5.12 from Fine et al. (2010) shows the comparison between both results.

[9] 2dF: 2-degree Field, QSO: Quasi-Stellar Object or quasar.

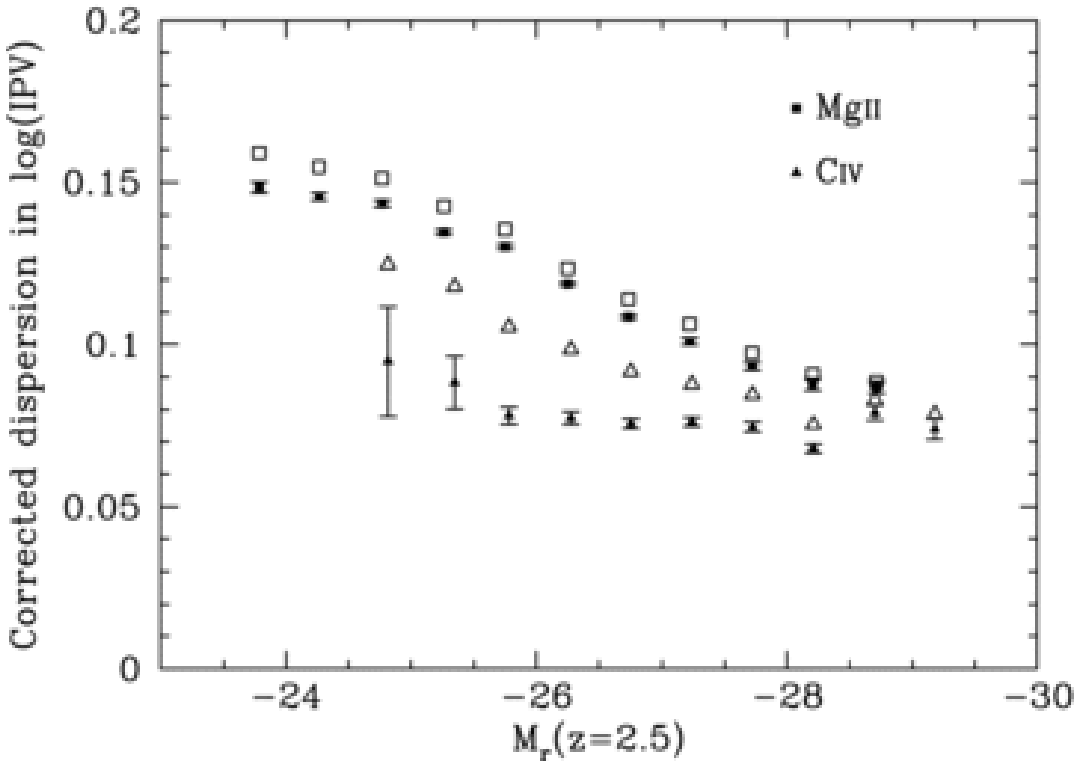

Figure 5.12: Figure 12 from Fine et al. (2010), showing the comparison between the dispersion in Mg II (squares) and C IV (triangles) linewidths, plotted against the absolute r-band magnitude K-corrected to $z = 2.5$. For the K-correction, an adjustment made to the photometric magnitudes and colours of distant objects that accounts for the effect of the redshift on their spectra, the authors used the SDSS quasar composite of Vanden Berk et al. (2001). Open symbols show the raw dispersion in the data calculated as the rms of the linewidth distribution. Solid symbols give the intrinsic dispersions, obtained after correcting by the mean of the errors on the IPV width measurements. We describe the IPV line-width measurement in the next subsection.

Fine et al. (2008, 2010) used the fact that if the linewidth measured from a spectrum depends on the viewing angle to the object, the linewidth dispersion for a model for the BLR can be calculated by 'observing' that model over different ranges of viewing angles. Combinations of models and viewing angle ranges that give dispersions larger than the observed dispersion can be rejected. Fine et al. assumed a coplanar obscuring torus surrounding the central SMBH and BLR with an opening angle $i_{\max}$ (measured from the vertical axis), so that the viewing angle i should satisfy $i \leq i_{\max}$. If the FWHM of a BEL varies with i, the dispersion in the FWHM distribution of that BEL should vary with $i_{\max}$.

5.2.1 Fine et al. test

Following Fine et al. (2008), we compare the dispersion of observed $\log(\text{FWHM})$ values with the dispersion of our simulated $\log(\text{FWHM})$ as a function of $i_{\max}$ and launch angle ϑ_0 to see if we can constrain $i_{\max}$ or ϑ_0.

Using the launch angle as a parameter, we evaluate the dispersion of the function $f(i) = \log(\text{FWHM}(i))$. As all the variables are, in fact, continuous, we interpolated each set of FWHMs to obtain the corresponding continuous functions. For *a given* $i_{\min}$,

the mean and the variance of the FWHMs are functions of $i_{\rm max}$, according to

$$\bar{f}(i_{\rm max}) = \frac{\int_{i_{\rm min}}^{i_{\rm max}} \sin i \; P(i) \; f(i) \, di}{\int_{i_{\rm min}}^{i_{\rm max}} \sin i \; P(i) \, di} \, , \tag{5.3}$$

$$\sigma_f^2(i_{\rm max}) = \frac{\int_{i_{\rm min}}^{i_{\rm max}} \sin i \; P(i) \; \left[f(i) - \bar{f}(i_{\rm max}) \right]^2 \, di}{\int_{i_{\rm min}}^{i_{\rm max}} \sin i \; P(i) \, di} \, , \tag{5.4}$$

where $P(i)$ is a weighting factor, equal to 1 in the Fine et al. (2008) approach, that measures the probability of not having obscuration in the LOS direction. We first present results using $P(i) = 1$ and then turn to a more complex case. Both Fine et al. (2008) and Mor et al. (2009) have $i_{\rm max} = 90^\circ$ as the upper limit for that angle. However, we have an extra limitation, set by the inclination of the base of the emitting region, chosen to be $\beta = 6^\circ$. Therefore, our upper limit is $i_{\rm max} = 84^\circ$. The lower integration limit was chosen as $i_{\rm max} = 2.5^\circ$, smaller than the smallest viewing angle adopted in the simulations.

Noting that Fine et al. (2008, 2010) have employed inter-percentile values (IPVs) rather than FWHMs to characterize the line widths, we also investigated the behaviour of this line measure from our results.

For a given percentage p, the definition of IPVp suggested by Whittle (1985) is the separation between the median (where the integrated profile reaches 50% of the total flux) and the positions where $p\%$ and $(100 - p)\%$ of the total flux are reached. Thus, calling d_1 and d_2 the distances between the median and p and $(100 - p)$ respectively, IPV$p = d_1 + d_2$. Figure 5.13, adapted from Rice et al. (2006), shows the definition of

this profile measure. In the cases shown there, $d_1 = a$ and $d_2 = b$ for $p = 10$. Similarly, $d_1 = c$ and $d_2 = d$ for $p = 20$. According to Rice et al. (2006), $IPV10$ characterizes the base and wings of the profile, while $IPV20$ (and any other % higher areas) characterize the line core. Also shown in the figure are two additional derived quantities, $A10$ and $A20$, that represent the interpercentile asymmetries.

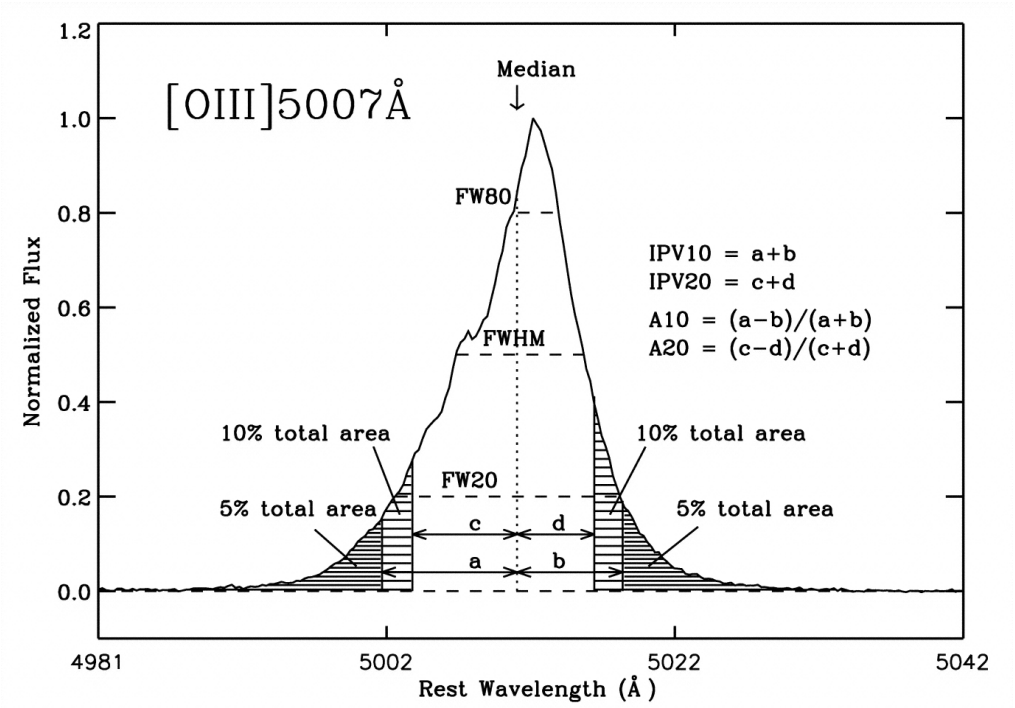

Figure 5.13: IPV definition, from Rice et al. (2006). The lengths a, b, c, d measure the separation between the median and the profile's 10%, 90%, 20%, and 80% area values, respectively. The derived quantities $IPV10$ and $IPV20$ are the interpercentile velocity widths. The other derived quantities, $A10$ and $A20$, represent the interpercentile asymmetries.

Figure 5.14 shows the averages (top panel) and dispersions (bottom panel) obtained for $\vartheta_0 = 6^\circ, 10^\circ, 15^\circ, 30^\circ, 45^\circ, 57^\circ$ for different $i = i_{\max}$ ranging from 5° to 84° when $i_{\min} = 2.5^\circ$. Solid lines correspond to FWHM and dashed lines to IPV line-width measurements. For most maximum inclination angles, for fixed $i_{\max}$, the dispersion of the FWHMs decreases with increasing ϑ_0. In particular, the dispersion of FWHM for the smallest launch angle is systematically larger than for all others. We can see that the general trend is lower dispersion for higher ϑ_0, except for the smaller $i_{\max}$, where $\sigma_{\vartheta_0=45^\circ}$ departs from it. [10]

We also compared these results to a simple model which assumes $g(i) = \text{FWHM}(i) = i(\,1000$ km s$^{-1})$, merely to see how the dispersion in log(FWHM) behaves for a model with known variation of FWHM with i. The dotted line in Figure 5.14 corresponds to this simple model. For the $i_{\min}$ considered in the Figure, this model departs from the observational results at any ϑ_0. We found that when $i_{\min} = 7.5^\circ$, the model approximately matches the result for $\vartheta_0 = 6^\circ$ in the range $35^\circ \lesssim i_{\max} \lesssim 60^\circ$. In the general case, it can be inferred that a more sophisticated model is needed. Such a model probably has to include information about the launch angle.

The dispersions obtained for the FWHMs are increasing functions of the parameter $i_{\max}$, although they show a mild decreasing trend at $i_{\max} \gtrsim 60^\circ$. Similarly, the dispersions of the IPVs are increasing functions of $i_{\max}$. Also included in Figure 5.14 is the

[10] We denote $\sigma_{\text{FWHM}(\vartheta_0=x^\circ)}$ by $\sigma_{\vartheta_0=x^\circ}$.

0.08 dex dispersion line reported by Fine et al. (2010) as the observational upper limit on the dispersion measured from their sample. We can see that as the torus half-opening angle (measured from the polar axis, and represented by $i_{\max}$) increases above about 18°, the wind launch angles required to match the Fine et al. (2010) constraints are increasingly larger.

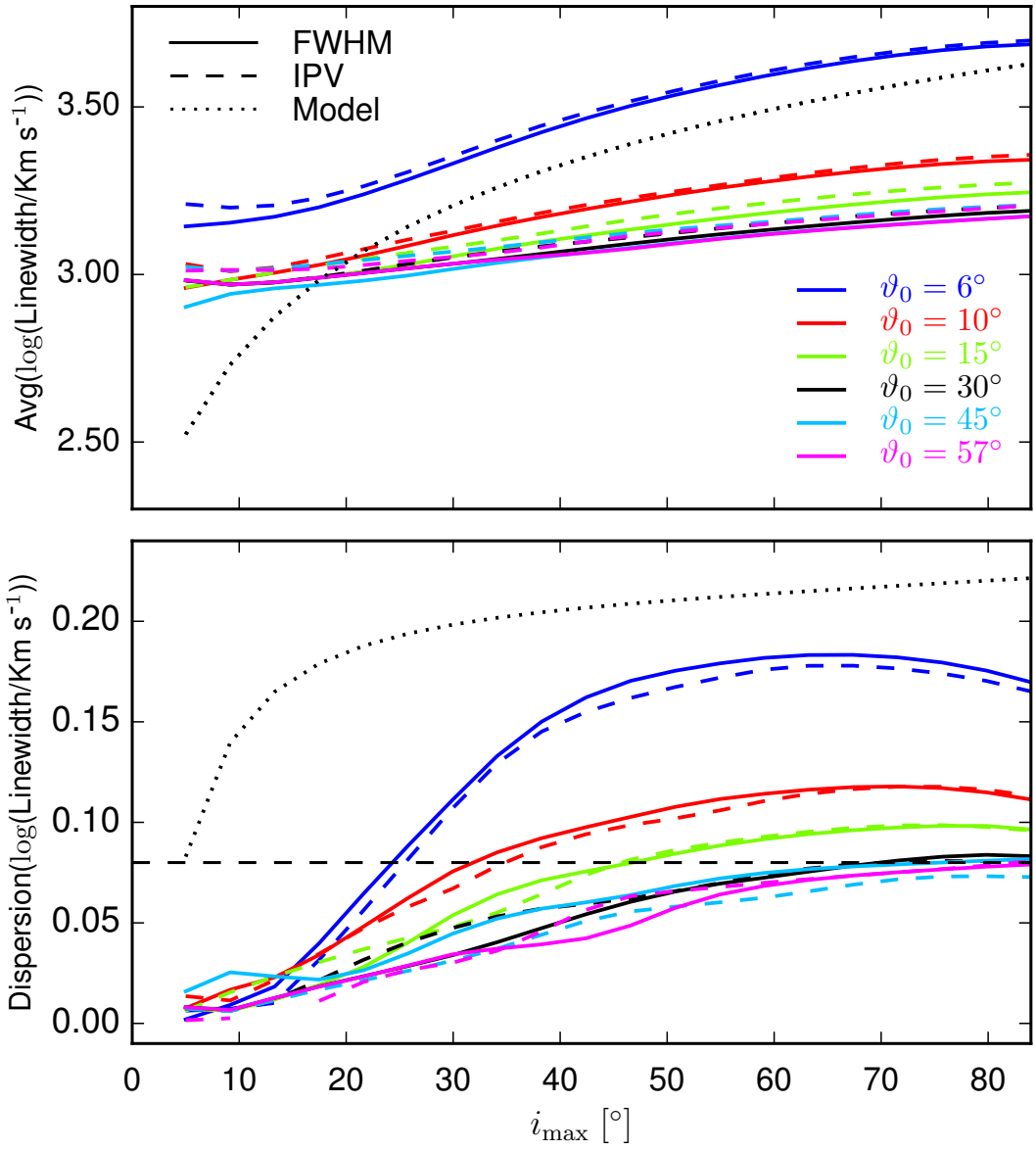

Figure 5.14: Averages (top panel) and dispersions (bottom panel) of $\log(\text{FWHM})$ (solid lines) and $\log(\text{IPV25})$ (dashed lines) evaluated for different launch angles, using $P(i) = 1$. The minimum viewing angle is $i_{\min} = 2.5°$. Included is the plot (dotted curve) of the dispersion for a model of the form $g(i) = \text{FWHM}(i) = i(1000 \text{ km s}^{-1})$ (see text). The dashed horizontal line plotted together with the dispersions corresponds to the Fine et al. (2010) results, the meaning of which is described in the text.

Figure 5.15 shows the allowed region in the i-ϑ_0 plane when analysing the dispersion of FWHMs (left panel) and of IPV25s (right panel). In both cases, $i_{\min} = 2.5^\circ$. Our results give, within the $\vartheta_0 < 60^\circ$ range allowed by the MHD solutions, a maximum half-opening angle of about 75°. For $\vartheta_0 \lesssim 30^\circ$, the region has a boundary that is a steep function of $i_{\max}$ and for $\vartheta_0 \gtrsim 30^\circ$ the maximum allowed half-opening angle is found at any ϑ_0. This maximum torus half-opening angle has a slightly different behaviour if the IPVs are considered, more apparent for lower value contours than for the one defining the region boundary. The original results on FWHM, reported in Chajet & Hall (2013), showed a smaller allowed region, with a maximum torus half-opening angle compatible with the observations of about 47°. The dispersion of IPVs led to a somewhat different region. The boundary reached its maximum at $\vartheta_0 \sim 30^\circ$ and declined for larger ϑ_0. However, the "absolute" maxima were similar in both cases.

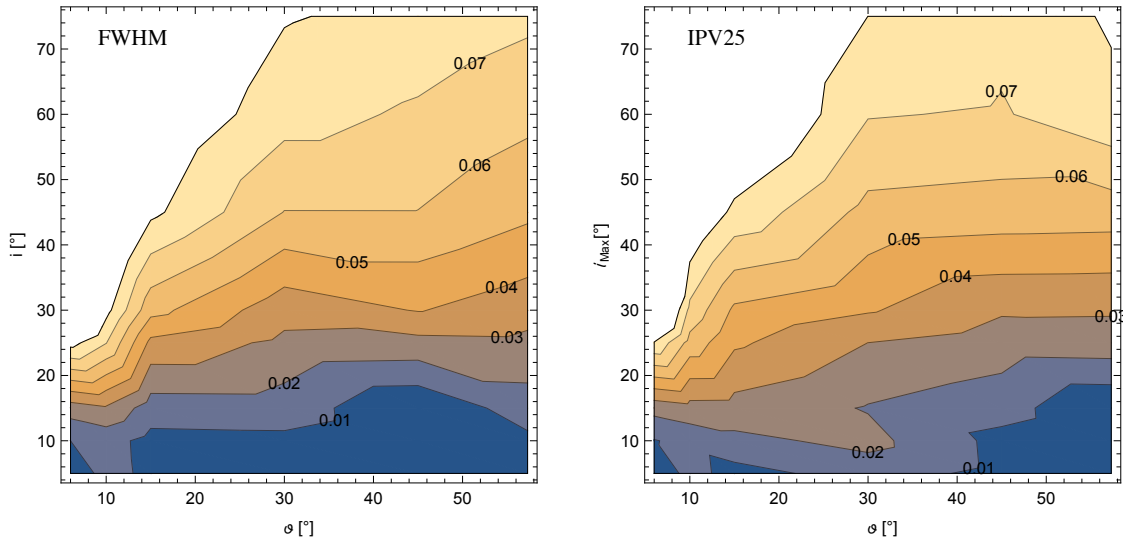

Figure 5.15: Contour plot of the standard deviation of the FWHM (left panel) and of IPV25 (right panel) vs launch and maximum inclination angles. Only the contours within the region that matches the Fine et al. results are shown.

In section 5.1 we showed that the profiles obtained for cases corresponding to larger inclination and small launch angles had double-horned profiles and mentioned that this contradicts observational results. The analysis presented in this section shows that inclination angle distributions reaching such large values for those small launch angles are in fact ruled out by their distribution of FWHM.

5.3 Clumpy torus

As mentioned above, Mor et al. (2009) adopted the more detailed expression for the escape probability proposed by N08. In that model, the torus is clumpy, consisting of

optically thick clouds and the quasar is obscured when one such cloud is seen along the LOS. Figure 5.16, adopted from Nenkova et al. (2008), shows the geometry of this model.

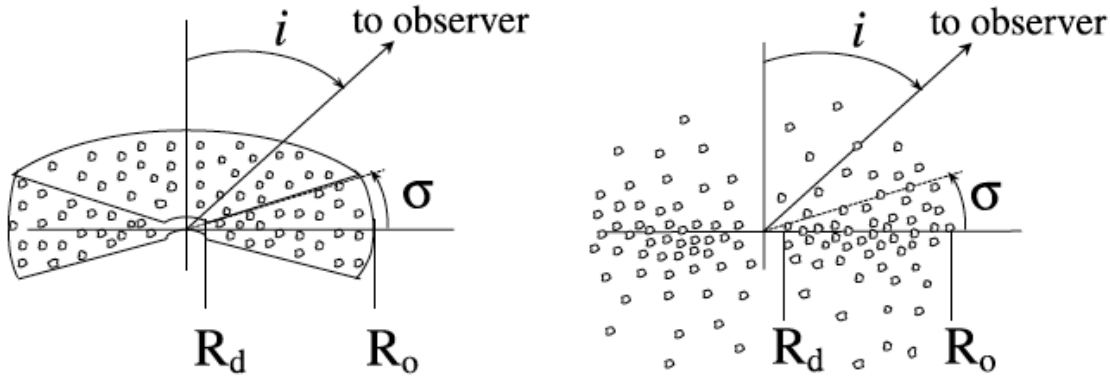

Figure 5.16: Nenkova et al. (2008) model geometry. Dusty clouds, each with visual (5500 Å) optical depth $\tau_{\rm V}$, occupy a toroidal volume from inner radius $R_{\rm d}$, determined by dust sublimation, to outer radius $R_{\rm o} = Y R_{\rm d}$. The radial distribution is a power law r^{-q}, and the total number of clouds along a radial equatorial ray is $\mathcal{N}_0$. The angular distribution has a sharp edge on the left panel and a smooth boundary on the right panel.

The torus is characterized by the inner radius of the cloud distribution (set to the dust sublimation radius, $R_{\rm d}$, that depends on the grain properties and mixture) and six other parameters. These are the outer radius, $R_{\rm o}$; the viewing angle i; the torus width parameter (analogous to its opening angle), σ; the mean number of clouds along a radial equatorial line, N_0; the optical depth per cloud, $\tau_{\rm V}$ (the same for all clouds in the configuration) and the power-law index of radial density profile, q, such that the number of clouds follows

$N(r) \propto r^{-q}$. Note that the outer radius is often given through the alternative parameter $Y = R_{\rm o}/R_{\rm d}$ (e.g., Mor et al. 2009, Nenkova et al. 2008).

Equation (3) in Mor et al. (2009) provides the weighting factor that we used in our evaluation:

$$P_{\rm esc}(i) = \exp\left[-N_0 \exp\left(-\frac{(90^\circ - i)^2}{\sigma^2}\right)\right]. \tag{5.5}$$

Implicitly, it is assumed that the disc and the torus are aligned. In their Fig. 6, Mor et al. (2009) present the torus parameter distributions for their sample, and from there it is clear that the distributions of the two parameters we need to input in Equation (5.5) (namely, N_0 and σ) are very broad. For completeness, we have reproduced in Table 5.3 the minimum, mean and maximum values of the two parameters, taken from Mor et al. (2009). The range of empirical values of σ obtained by Mor et al. (2009) do not differ significantly from that adopted by Nenkova et al. (2008). On the other hand, the maximum observational value reported by Mor et al. (2009) for the quantity N_0 is significantly smaller ($\sim$ half) than the upper limit, $N_0 \sim 15$, considered by Nenkova et al. (2008), who, based on the shape of the SED at wavelengths beyond 60 μm, deduced that the parameter would not likely exceed a value in the range 10-15.

Note that within this model, we only have $i_{\rm max} = 90^\circ$. The resulting distribution of the dispersions with the launch angle are presented in Figure 5.17, where each line corresponds to a given combination of σ and N_0. For clarity, in the Figure we excluded combinations such that at least one of the parameters takes its minimum value, as such

Parameter	Minimum	Mean	Maximum
N_0	1	4.923	8
σ [°]	15	34	57

Table 5.3: Minimum, mean and maximum values of the N_0 and σ torus parameters from the Mor et al. (2009) sample.

combinations yield lines farther away from the observed upper limit dispersion. However, two additional distributions of the dispersion curves are included in the same figure, corresponding to different warped disc models developed by Lawrence & Elvis (2010), that are discussed in section 5.4. Included is also a constant line, representing the Fine et al. (2010) constraint.

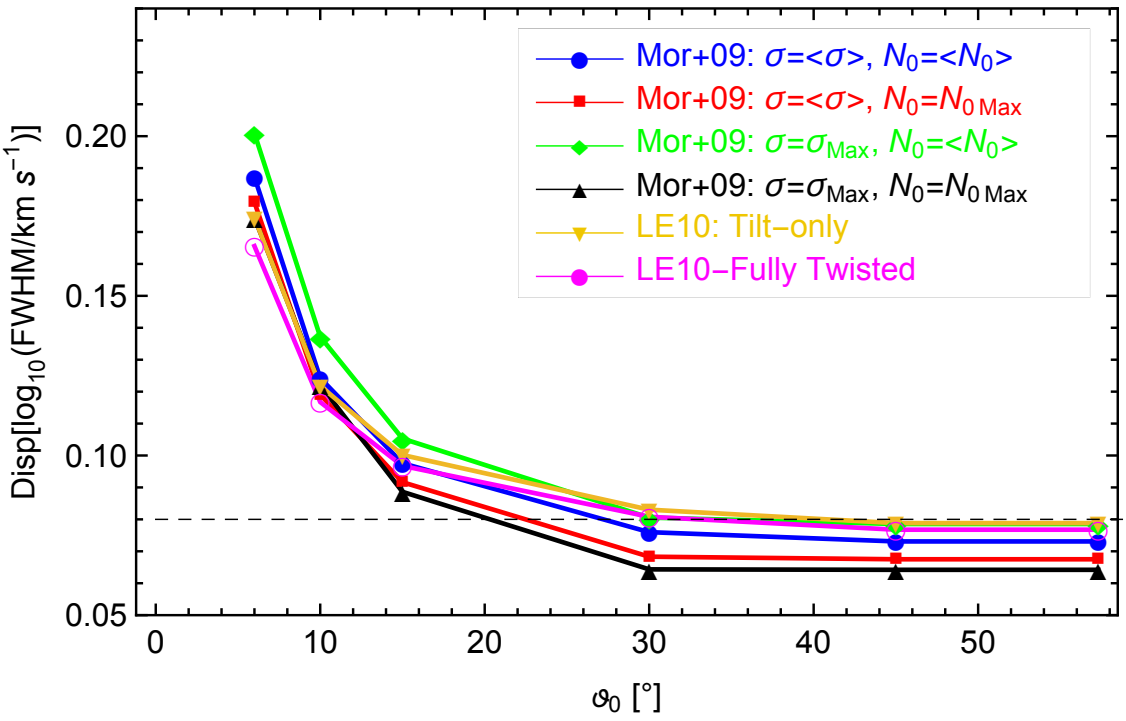

Figure 5.17: Dispersions of $\log(\mathrm{FWHM})$ using $P(i = 90^\circ - \beta)$ as given by Equation (5.5). Here, $i_{\min} = 2.5^\circ$, $i_{\max} = 84^\circ$. Each of the lines obtained using the N08 prescription represents a different combination of σ and N_0. Also included is a line corresponding to dispersions calculated assuming a tilt-only warped disc (see next section). The dashed line corresponds to the Fine et al. (2010) results.

The shape of the curves, regulated by the parameters σ and N_0, are similar to each other in all cases, with a slightly steeper descent in the cases $N_0 = \max(N_0^{\rm Mor+09})$. For $\vartheta_0 \lesssim 20^\circ$, all cases depart from the Fine at al. result, and the departure increases with decreasing N_0. For $\vartheta_0 \sim 20^\circ$, only the curves corresponding to $N_0 = \max(N_0^{\rm Mor+09})$, with $\sigma = \max(\sigma^{\rm Mor+09})$ and $\sigma = \bar{\sigma}^{\rm Mor+09}$ are below the Fine et al. constraint. That motivated us to analyse what different combinations of these parameters of the N08 model match the Fine et al. limit, and look for a trend in the minimum launching angle at which the condition is satisfied. We found that the ϑ_0 at which a curve corresponding to a given σ intersects the Fine et al. constraint line increases with decreasing N_0 and the family of curves moves towards the right for decreasing σ. For instance, adopting $\sigma = \bar{\sigma}^{\rm Mor+09}$ and increasing N_0, one finds that for $N_0 = 15$ (the likely upper limit, according to N08), all dispersions corresponding to $\vartheta_0 \gtrsim 15^\circ$ are below the Fine et al. boundary, while for $N_0 \sim \min(N_0)$ the curve is always above that constraint. If, instead, $\sigma = \max(\sigma^{\rm Mor+09})$ is adopted, for $N_0 \sim 8$ the dispersion is already below the Fine et al. limit for $\vartheta_0 \sim 20^\circ$ and for $N_0 \sim 15$, all dispersions for the cases $\vartheta_0 \gtrsim 10^\circ$ are below that line. If, on the other hand, N_0 is kept fixed and σ is changed, the trend is that the intersection-ϑ_0 increases with decreasing σ and the set moves almost rigidly to the right if N_0 decreases.

Note that Mor et al. (2009) found $P(i = 50^\circ) \simeq 30\%$ and $P(i = 70^\circ) < 3\%$ when N_0 and σ were set to their mean values, and, based on that, suggested that the inclination angle for type-1 objects should lie in the range $0^\circ - 60^\circ$. However, the authors found that

for the case in which all the parameters but the torus width are set to their mean values, the escape probability falls rapidly if $\sigma > 45°$. Our results indicate that the parameter N_0 is important when considering the dispersions of the line widths.

These results were obtained from a set of profiles corresponding to both mass and luminosity fixed, whereas Fine et al. (2010) and Mor et al. (2009) samples involve a range of masses and luminosities. However, as already mentioned, Fine et al. (2010) found that the dispersion in C IV linewidths essentially does not depend on luminosity. As can be seen from their Figure 2, the IPV linewidth measurements are bound by $10^{8.25} \lesssim M_{\rm BH}/M_{\odot} \lesssim 10^{10}$ and $0.1 \lesssim L/L_{\rm Edd} \lesssim 1$. Based on that, in Chajet & Hall (2013) we anticipated that our results would not be strongly affected by considering different masses and/or luminosities. In Chapter 6 we study this extension and show that the results do depend on both mass and luminosity, albeit not with the same strength. That is, our prediction was not accurate.

5.4 Warped Discs

As mentioned in the Introduction, the model of Lawrence & Elvis (2010, LE10 hereafter) replaces the torus by a warped disc. In this section we explore whether we can infer new constraints on the BLR or on the parameters of warped discs by applying a restricted set of such warped disc models. Briefly, we evaluate the unobscured solid angle distribution as a function of observer inclination i, $dC(i)$, calculated for arbitrary disc tilt angle θ.

Then, we restrict our attention to the subset within our constraint $i < 90° - \beta$, using the calculated unobscured solid angle distribution to determine the probability of the object being unobscured. Finally, we apply that probability to our emission-line profiles, in a way analogous to that employed with the Fine et al. (2010) model.

LE10 studied the fraction of type 2 AGN, $f_2 \approx 0.58$ among all AGN, and proposed a framework to account for it. They assumed that randomly directed infalling material at large scales would produce a warped disc at smaller scales, where it eventually aligns with the inner disc. They analysed both fully twisted and tilt-only cases (explained in detail below) under that assumption and showed that fully twisted discs can not reproduce the observed f_2. Models assuming tilt-only discs, on the other hand, match the observed f_2.

A warped disc can be analysed as a series of annuli, each characterized by its radius and the two angles $\theta(r)$ (the angle between the spin axes of the annulus and the inner planar disc, i.e., the tilt) and $\phi(r)$ (the angle of the line of nodes measured with respect to a fixed axis on the equatorial plane, i.e., the twist). Thus, a fully twisted disc corresponds to $\phi(r) = 0$, $\phi(r+\delta r) = 2\pi$, $\delta r \ll r$ and a tilt-only disc corresponds to the case of constant $\phi(r)$. Each of the two warp modes can be associated with a covering factor C depending on the misalignment, and the distribution of covering factors can then be inferred from the probability distribution of the misalignment. Conversely, knowing the distribution of covering factors, the probability distribution of misalignments can be evaluated. This

is the approach we take below. Note that LE10 calculated the azimuthally integrated covering factor while we study the covering fraction as a function of the azimuth.

Consider first the tilt-only case. In Appendix B we derive the expression for the differential covering factor $dC(i)$ corresponding to this case. We estimated the unobscured fraction $P(i) = dC(i)/2\pi\sin(i)$ as a function of the tilt angle and found that considering a random distribution in solid angle of θ up to $\theta_{\max} = \pi$ yields results incompatible with our line profiles. This is because that case corresponds to $i_{\max} = \pi/2$ for the Fine et al. case in all our diagrams. In a random distribution of incoming orientations with $\theta_{\max} = \pi$, for every case of orientation θ there is a corresponding case with orientation $\pi - \theta$ (statistically speaking), which means that this model is identical to the case $i_{\max} = 90^{\circ}$ for our purposes. A variant of that model, with a random distribution in solid angle of θ up to $\theta_{\max} = \pi/2$ was also analysed. Using equation (B.7) for the probability and Equations (5.3) and (5.4) we performed the same analysis applied in the Fine at al. case. Note that the only angle to be considered in this case is $i_{\max} = \pi/2$, so we also ruled out this model. We have included in Figure 5.17 the resulting dispersions for this model. The dispersions are far from the Fine et al. (2010) observational results for any launch angle considered.

An analogous analysis was performed for the full twist case, with $0 \leqslant \theta \leqslant \pi/2$. The probability of being unobscured for random inclinations is given by $P(i) = \cos(i)$ and, again, the region in the $i - \vartheta_0$ plane is the same obtained using other prescriptions.

5.5 Chapter Summary and Conclusions

We analysed how the resulting line profiles depend on different parameters of the model. In particular, we studied how the observing angle i and the wind launch angle ϑ_0 affect the emission line profiles. We found that for fixed ϑ_0 all profiles are slightly asymmetric, with more asymmetric profiles for smaller inclination. For a given launch angle, less inclined objects have a larger fraction of their flux corresponding to motion towards the observer, so their profiles are less symmetric. For fixed i, the angle to be considered is $\vartheta > \vartheta_0$, i.e., the angle at which a wind that started at ϑ_0 intercepts the base of the emitting region. Two different cases can be considered. If $\vartheta > i$, wind velocity projections are mostly towards the observer, with red wings increasingly important for the cases $\vartheta \leq i$.

Our main conclusion is that the shape of the line profiles, their FWHMs and shift amounts (whether red or blue) with respect to the systemic velocity depend not only on the viewing angle but also on the angle (with respect to disc plane) at which the outflow starts. In fact, the relevant quantity is a combination of the two angles, rather than either angle individually. This is a consequence of how the model has been constructed. In effect, the optical depth expression includes a dependence on the wind contribution, which ranges from $v_{\rm p}\sin(\vartheta+i)$ when $\phi = 0$, to $v_{\rm p}\sin(\vartheta-i)$ when $\phi = \pi$. The launch angle parameter, although included in the models, has been less explored in the literature. Note, however, that MC97 have reported that their C IV line profiles do not strongly depend on

ϑ_0 (λ_0 in their notation). This difference could be due to our use of EBS92 streamlines instead of MC97 streamlines, or it could be due to our more rigorous calculation of L_ν as compared to MC97. Flohic et al. (2012), who studied Balmer emission lines with a model that is also based on that of MC97, reported, as well, just a weak dependence of the parameter Q on the launch angle.

Using as a constraint the observational results obtained by Fine et al. (2010) for the C IV lines in their sample, we found that the allowed region in the $i - \vartheta_0$ plane has an upper limit that depends on the torus half-opening angle, $i_{\max}$. The line that defines the region boundary is a steep function of $i_{\max}$. For instance, a launch angle $\vartheta_0 \sim 7^\circ$ is only allowed for a torus half-opening angle $\lesssim 20^\circ$, while $\vartheta_0 \lesssim 20^\circ$ for $i_{\max} \sim 50^\circ$. We originally found that the maximum torus half-opening angle that is compatible with the observations is about 47°, but the analysis of the profiles obtained with the revised interpolation routine returned a larger allowed region in the $\vartheta_0 - i_{\max}$ plane. As a result, the maximum half-opening angle is higher than the original limit and the revised boundary is a steeper function of the parameters than the original. Considering a model that replaces the torus with a tilt-only warped disc, formed by the alignment at smaller distances of material falling at large distances from random directions, yields no difference in the resulting allowed region of the inclination-launch angle plane.

These results were obtained for a single mass and luminosity, as opposed to the Fine et al. (2010) and Mor et al. (2009) results which were obtained from datasets spanning an

order of magnitude in both parameters. However, as mentioned in section 5.2, Figure 2 of Fine et al. (2010) indicates a negligible dependence of the dispersion of the linewidth on both these parameters. Based on that, in Chajet & Hall (2013) we suggested that simulations for different masses and luminosities would yield similar results to those reported there, for our fiducial case. In Chapter 6 we expand the analysis to several different combinations of mass and luminosity, as well as other values of the dimensionless angular momentum parameter λ. There we show that, despite the expectation of no dependence on the source intrinsic parameters, the results are indeed affected by them.

6 Parameter space

6.1 Line Profiles

In Chapter 4 we presented our hybrid model, that combines the disc-wind model of Murray & Chiang (1997) with the MHD driving of Emmering et al. (1992). In Chapter 5 we applied that model to evaluate the line luminosity (Equation (4.14)) in our mass and luminosity fiducial case. We constructed a series of models parametrised by two angles, inclination and the wind launch angle, and estimated the maximum torus half-opening angle (measured from the polar axis) compatible with the observations for that case. Here we extend the analysis to a range of masses and luminosities. We have considered masses within the range $8 \leqslant \log(M/\mathrm{M}_{\odot}) \leqslant 10$ and luminosities that satisfy $45 \leqslant \log(L_{\mathrm{UV}}/10^{46}\mathrm{erg\ s^{-1}}) \leqslant 48$, organized in a grid such that, for each mass, three different luminosity values, corresponding to $\dot{m} \sim 0.1, 0.5, 1$, are considered. For brevity, we hereafter adopt the labelling convention $MxxxLyyy$ to refer to an object of mass $10^{xx.x}$ $\mathrm{M}_{\odot}$ and luminosity $10^{yy.y}$ erg $\mathrm{s^{-1}}$. The range of viewing angles is $5^{\circ} \leqslant i \leqslant 75^{\circ}$ and the launch angles are in the same range as in the previous chapter, $6^{\circ} \leqslant \vartheta_0 < 60^{\circ}$.

In section 6.2.1 we extend the sample to include an even smaller mass, $\log(M/\mathrm{M}_{\odot}) = 7$, and luminosities corresponding to the same three Eddington values considered for the other cases.

We also consider two different values of the dimensionless angular momentum parameter and run simulations using $\lambda = 10$ and $\lambda = 30$. These values were chosen to match those in EBS92 and BP82. Interestingly, the comparison shows that the results depend weakly on this parameter. In section 6.3 we discuss in detail how different λ values affect the results.

To scale the inner and outer radii of the emitting region from the fiducial case to any mass-luminosity combination we adopted a luminosity- and mass-based scaling:

$$r_{\mathrm{min,\,max}} = 2M_8^{1/3}L_{46}^{0.5}\ 10^{15,\,19}\ \mathrm{cm}, \tag{6.1}$$

where $M_8 = \frac{M}{10^8 \mathrm{M}_{\odot}}$ and $L_{46} = \frac{L_{\mathrm{UV}}}{10^{46}\mathrm{erg\ s^{-1}}}$ and M is the mass, in units of solar masses and L_{UV} is the object's UV luminosity, in erg s^{-1}. As mentioned in Table 5.2, $r_{\mathrm{min,\,max}} = 2 \times 10^{15,\,19}$ cm for a $M = 10^8$ M$_{\odot}$, $L_{\mathrm{UV}} = 10^{46}$ erg s^{-1} central object. We had initially set a scaling depending only on luminosity, $r_{\mathrm{min,\,max}} = 2L_{46}^{0.5}\ 10^{15,\,19}$ cm. However, the profiles rendered by such a scaling were too broad and, in addition, had much larger linewidth dispersions than the fiducial case. Incorporating the mass dependence had the effect of reducing both the FWHMs and corresponding dispersions. The mass dependence is an approach less explored in the literature, but has been applied before (in the optical by, e.g., Flohic et al. 2012). In that work, the computational domain (inner and

outer radii of the BLR) is given in units of the gravitational radius of the central object, $R_{\rm G} = G\ M/c^2$. The mass scaling adopted here is motivated by the results on the BLR reported by Elitzur et al. (2014), that will be discussed in section 6.2.

In Chapter 5 the source function $S(r)$ was evaluated for the fiducial parameters. The source function $S(r)$ in this chapter has been scaled to the different luminosities being considered. For objects of different L_{1350}, we scaled the line luminosity by replacing r_i with $r = r_i\sqrt{L_{1350}/10^{46}}$, linearly interpolating the resulting binned line luminosity $L(r)$ function in $\log_{10} r$, and then computing $S(r) = (L_{1350}/10^{46})L(r)/\pi r$. The radial points are evenly distributed in log-space, and thus the denominator comes from $2\pi\ (r + \Delta r)^2 - r^2 \simeq 2\pi r\Delta r$, with $\Delta r = \log_{10}\sqrt{10} = 0.5$.

Figure 6.1 shows several profiles obtained in our simulations. Each panel includes the lines corresponding to fixed viewing and launch angles and different masses and luminosities. Solid and dashed lines correspond to $\lambda = 10$ and 30, respectively and the normalization is with respect to the corresponding $\lambda = 10$ case. For clarity, only results corresponding to a subset of the viewing angles are included, making it possible to see general trends. Launch angles are constant and viewing angles increase along rows. On the other hand, viewing angles are constant and launch angles increase along columns.

For fixed launch and inclination angles (i.e., within a given panel), the profiles are, as expected, broader for more massive and less luminous objects. As a result of that, our fiducial case profiles are the narrowest among the mass-luminosity combinations studied.

As we will describe below, the trends noted in Chapter 5, when analysing this case, are presented in all other cases studied here.

Within each panel, not only the profiles are broader with increasing mass and decreasing luminosity, but also the shift of the peak and/or the fractions of the flux blue- and red-ward of the central velocity vary. For fixed ϑ_0 (i.e., looking along a row), for any mass-luminosity combination, the profiles are broader as the inclination angle increases.

The profiles corresponding to any mass-luminosity combination have similar general behaviour and trends to the fiducial case, analysed in Chapter 5. For instance, all profiles have a certain degree of asymmetry that decreases with increasing inclination. As before, the blue wings change less than the red wings, so that as the inclination angle increases, the red wings become relatively stronger.

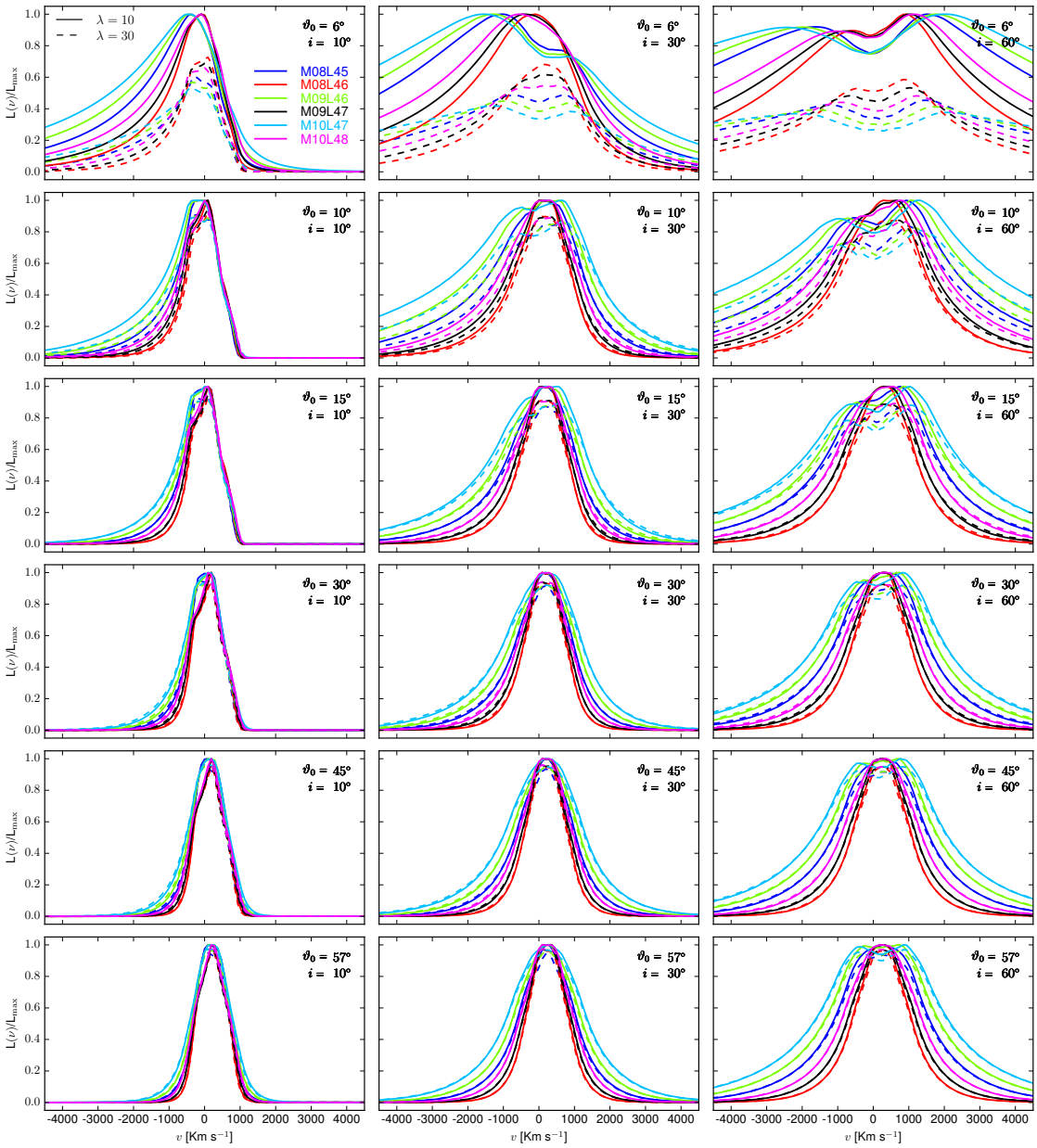

Figure 6.1: Normalized (with respect to the corresponding $\lambda = 10$ case profile) line luminosity vs. velocity for several values of viewing and launch angles. Solid and dashed lines correspond, respectively, to $\lambda = 10$ and $\lambda = 30$. Each panel shows the profiles for given launch and viewing angles.

In the same Figure, the effects of changing the launch angle ϑ_0 can be appreciated by looking along a column. Physically, the wind velocity depends on the launch angle, but the observer sees the fraction projected onto the LOS. However, as discussed in Chapter 5, in the framework of the present model, the actual angle to be considered is the angle ϑ at which a line launched with some ϑ_0 crosses the base of the emitting region (when ϑ_0 increases, so does ϑ).

For any given combination of the two angles i and ϑ_0, the projection of the velocity will be towards the observer on the fractions of the emitting region that satisfy the condition $\vartheta > i$.

The shape of a spectral line can be characterised by analysing the ratio $S = \text{FWHM}/\sigma_\text{l}$, where σ_l is the standard deviation of the line. A Gaussian profile is characterised by $S_\text{Gauss} = 2.\sqrt{2.\ln(2.)} \simeq 2.35$, while $S \to 0$ for Lorentzian and logarithmic profiles. Rectangular and triangular functions have $S = S_\text{rect} = 2\sqrt{3} \simeq 3.46$, and $S = S_\text{triang} = \sqrt{6} \simeq 2.45$, respectively. The minimum and mean values from our profiles are $S \sim 0.88$ and $S \sim 1.71$ respectively, neither of which are canonical values. This could be related to a limited frequency range and also to the fact that the profiles are better represented by a combination of cases.

Figure 6.2 shows the distribution of the parameter S for our profiles versus the line FWHM (left panel) and versus σ_l (right panel). As mentioned in Collin et al. (2006), the two line measurements are sensitive to different parts of the line profile. The line

dispersion is a higher order moment, relatively more sensitive to the line wings and less sensitive to the line core. The fact that most of our lines are below the $S_{\rm Gauss}$ value, indicates that they have more prominent wings than a simple Gaussian profile. This is not surprising, as we have modelled a turbulent motion superimposed on the thermal velocity.

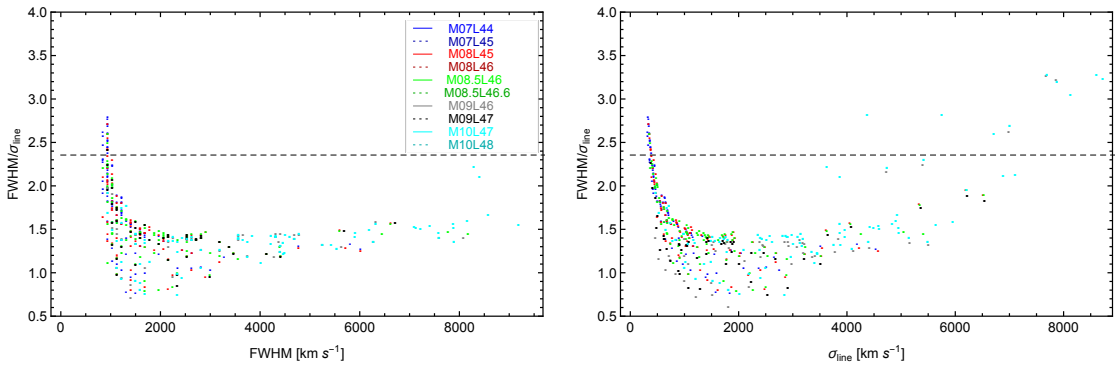

Figure 6.2: The left panel shows the line shape parameter, S, vs. FWHM, for all $\lambda = 10$ profiles, where $S = \mathrm{FWHM}/\sigma_{\rm l}$ and $\sigma_{\rm l}$ is the standard deviation of the line. The right panel shows the same S values versus $\sigma_{\rm l}$. The dashed line in both panels corresponds to the value $S = S_{\rm Gauss} = 2.\sqrt{2.\ln(2.)} \simeq 2.35$.

6.1.1 Luminosity-linewidth plane

Figure 6.3 is similar to Figure 2 from Fine et al. (2010). Note that here we used line FWHM (instead of IPV) and in the x-axis, luminosities have been plotted, instead of absolute magnitudes. The differences in luminosity from sources of intrinsic identical

luminosities are attributable to the differences in viewing angle. Because the observer sees a fraction that depends on the projection on the sky of the emitting region, the x-axis is constructed by multiplying the assumed object's luminosity by the cosine of the inclination angle. The grey-shaded area corresponds approximately to the densest (i.e., with the largest number of points per unit area) region in that figure. The dotted and dashed lines represent loci of constant mass and Eddington ratio, respectively, where the mass has been evaluated, as in Fine et al. (2010), using Equation (7) in Vestergaard & Peterson (2006). The shaded regions are bounded by lines of constant $\log(M_i) \pm 0.2$, where M_i is one of the mass values used in our simulations, in units of solar masses. While the sample standard deviation of the weighted average zero point of their mass scaling relationships reported by Vestergaard & Peterson (2006) is 0.36 dex, we had to use a smaller range around $\log(M_i)$ to avoid overlapping of regions belonging to two different such values. For each mass-luminosity combination, results corresponding to the same launch angle but different inclination are linked by solid lines, with the same colour scheme used in other figures.

We can draw some conclusions and constraints from the results in this figure. Note that $\vartheta_0 = 6^\circ$ results can not retrieve their original mass values, except for the lowest inclination angles. That could be seen as a failure of the model when smaller launch angles are considered. A new lowest ϑ_0 value should be determined if the tilt of the base of the emission region were modified. Part of the degeneracy around the $M = const.$

lines is due to the fact the expression given by Vestergaard & Peterson (2006) does not include viewing angle as a parameter.

Considering the $\log$-Luminosity vs $\log$-FWHM plane in Figure 6.3, we would like to assess which parameter(s), and in which direction(s), should be changed in future simulations to achieve better agreement with the observational results. First, note that the correlation between FWHM and IPV has a non-negligible scatter, as can be seen from e.g., Figure A8 of Fine et al. (2010). Moreover, there is no direct conversion from one measure to the other, except for well-determined cases, such as a Gaussian curve. The relation is FWHM $= 1.75\,$IPV in the Gaussian case. This degeneracy makes the comparison between our linewidth vs. luminosity with Figure 2 of Fine et al. (2010) not completely straightforward. A more direct comparison can be done with the results of Decarli et al. (2008), who reported a mean $\langle \text{FWHM} \rangle = 4030 \pm 1200$ Km s^{-1} from their sample. This value might be consistent with our findings, although it should be pointed out that their sample was much smaller than that of Fine et al. (2010).

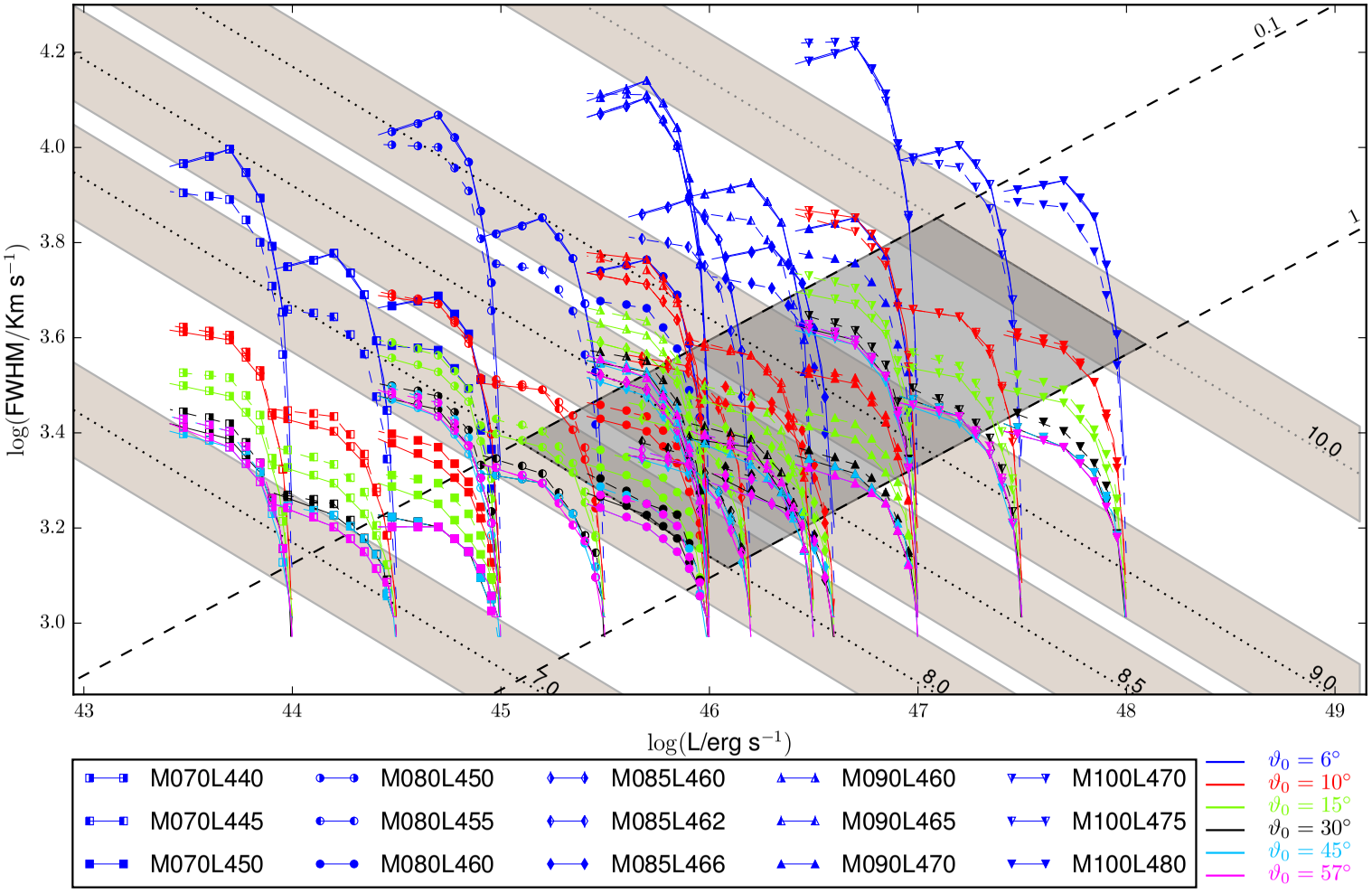

Figure 6.3: Luminosity-FWHM plane., similar to Figure 2 of Fine et al. (2010). The grey-shaded area corresponds approximately to the densest region in that figure. The dotted and dashed lines represent loci of constant mass and Eddington ratio, respectively. Each colour corresponds to a different launch angle. The points shown over each track are uniformly distributed over the solid angle, therefore they are closer to each other at larger viewing angles and more sparsely distributed at smaller i.

6.2 FWHM statistics

Here we perform the same calculations made for the fiducial case for each of the combinations of mass and luminosity. Thus, for each set of profiles obtained for different inclination angles i and launch angles ϑ_0, we study how the FWHMs are distributed with respect to i. Figure 6.4 shows $\log(\text{FWHM})$ of the line profiles from our simulations. Each panel corresponds to a given mass and luminosity and each colour, to a different launch angle, with solid and dashed lines used for the $\lambda = 10$ and $\lambda = 30$ cases respectively. Here we can see again that the results follow the expected behaviour of the FWHM with mass and luminosity, i.e., it increases with increasing mass and decreasing luminosity.

Notably, for any given mass and luminosity (i.e., within a particular panel), the differences due to the angular momentum are almost independent of the launch angle, except for the lowest ϑ_0 value.

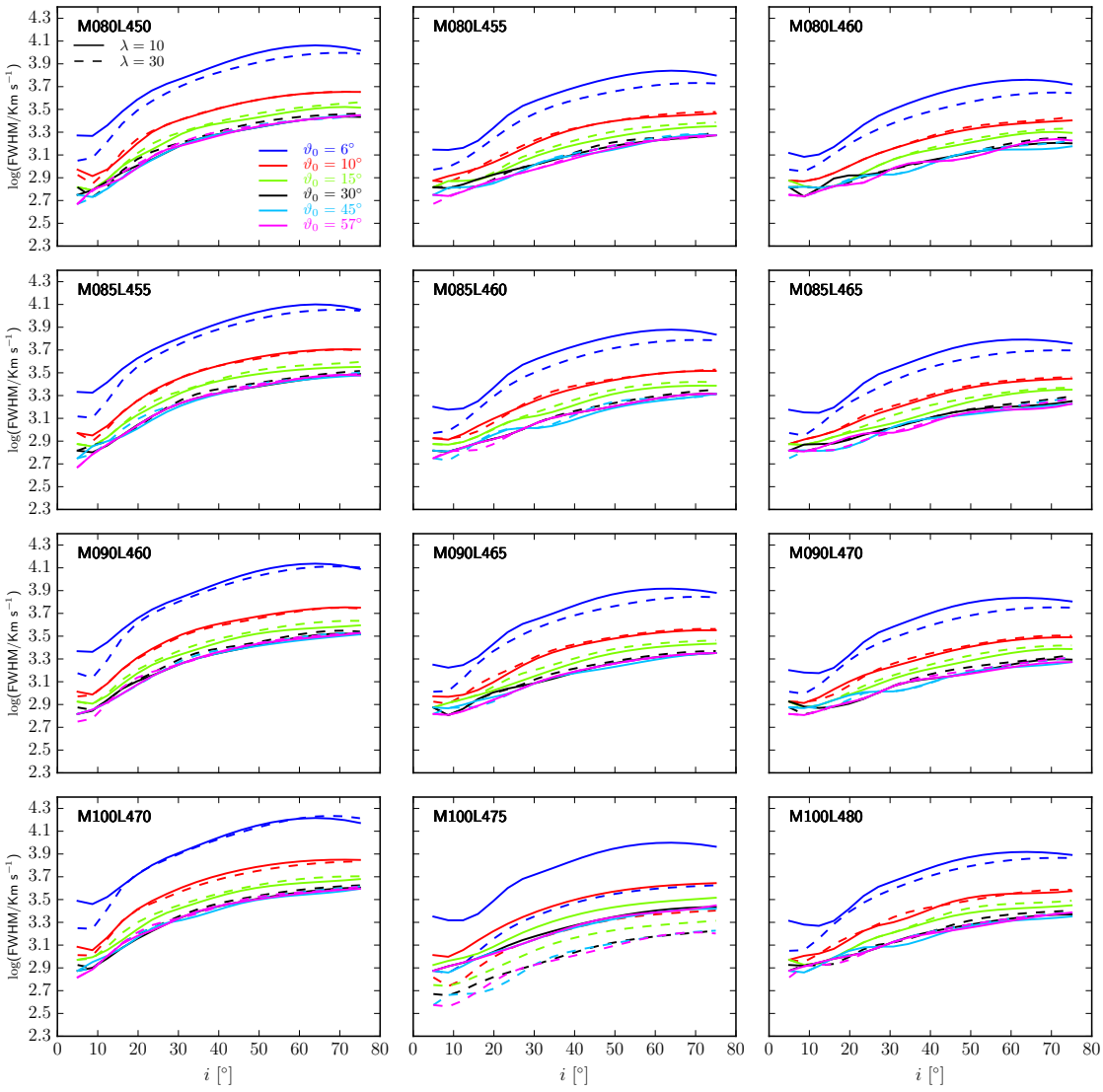

Figure 6.4: Profile FWHM vs. inclination angle. Solid lines are $\lambda = 10$ cases, while $\lambda = 30$ cases are represented by dashed lines. Each panel corresponds to a different combination of mass and luminosity and each line represents results for a given launch angle.

Analogously to what we did in Chapter 5, we analyse the FWHM of our line profiles applying the prescription of Fine et al. (2008, 2010). Using again the launch angle as a parameter, we evaluate the dispersion of the function $f(i) = \log(\mathrm{FWHM})$. We show the dispersion of our line profile sets versus $i_{\max}$ in Figure 6.5. The panels are arranged as constant mass along rows and constant Eddington ratio along columns. The solid and dashed lines correspond to $\lambda = 10$ and $\lambda = 30$ cases, respectively. The black horizontal dashed line represents, as before, the Fine et al. (2010) constraint. Again, only dispersions that satisfy $\sigma_f^2(i_{\max}) \leq 0.08$ dex are allowed, which imposes a constraint on the possible $i_{\max}$.

The set of allowed $i_{\max}$ changes from left to right, increasing as the Eddington ratio increases and the mass on each row is constant. From top to bottom, i.e., for constant Eddington ratio, the range of allowed $i_{\max}$ values shrinks with increasing mass. These features are related to the torus geometry and its dependence on mass and luminosity and will be discussed below.

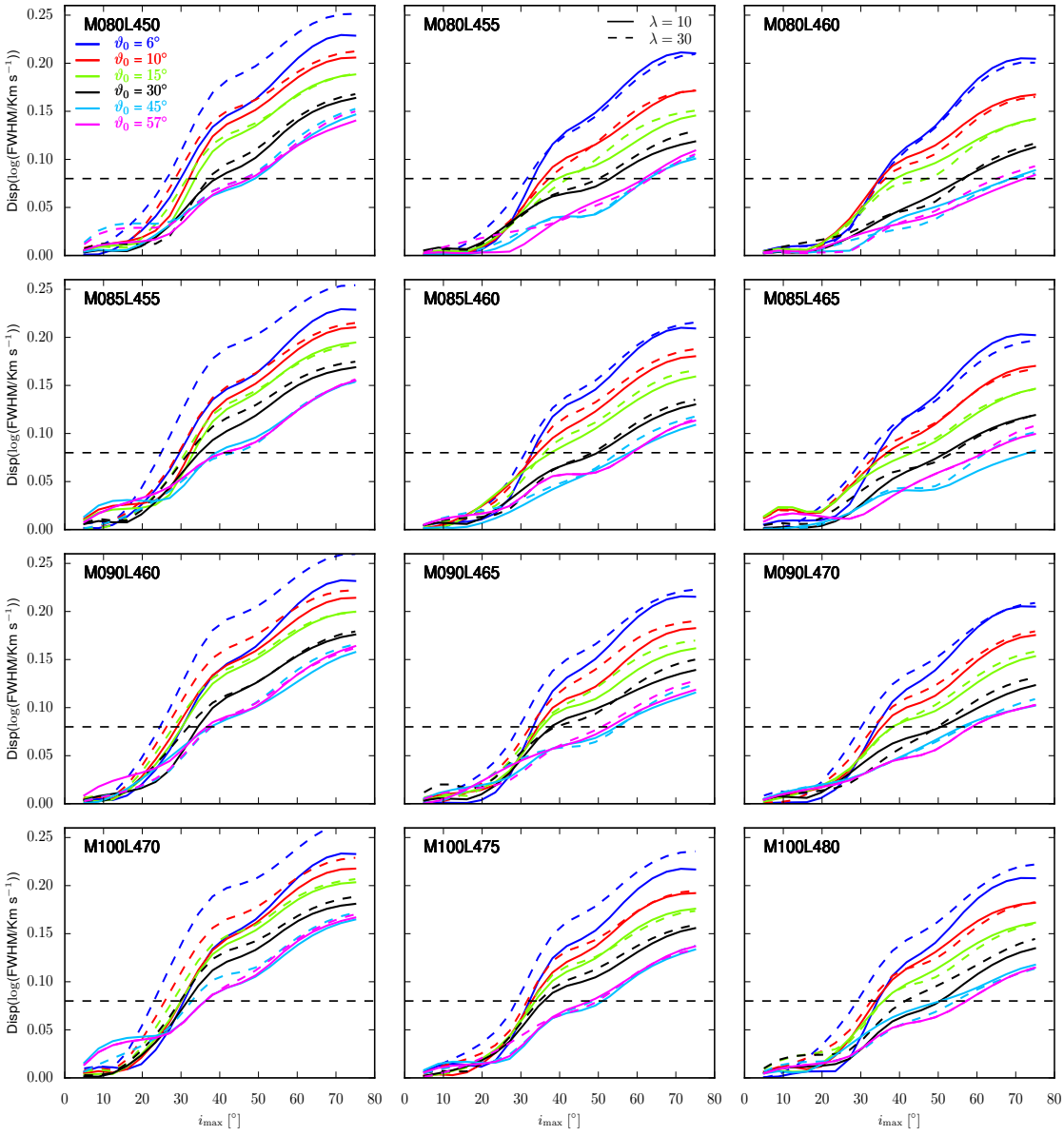

Figure 6.5: Standard deviation of the profile FWHM vs. inclination angle. The symbol code is as in Figure 6.4 and the black horizontal dashed line corresponds to the Fine et al. (2010) 0.08 dex constraint. Each panel corresponds to a different combination of mass and luminosity and each curve represents results for a given launch angle.

As shown for the fiducial case, another way to visualize the constraint on the $i_{\max}$ parameter is by making contour plots of the corresponding $\sigma_f(i_{\max})$ as function of both ϑ_0 and $i_{\max}$. In Figure 6.6 we show such contour plots of the standard deviation of the profile FWHM vs. launch and inclination angles for our set of masses and luminosities for the case $\lambda = 10$. The data are shown in the same arrangement as in Figure 6.5.

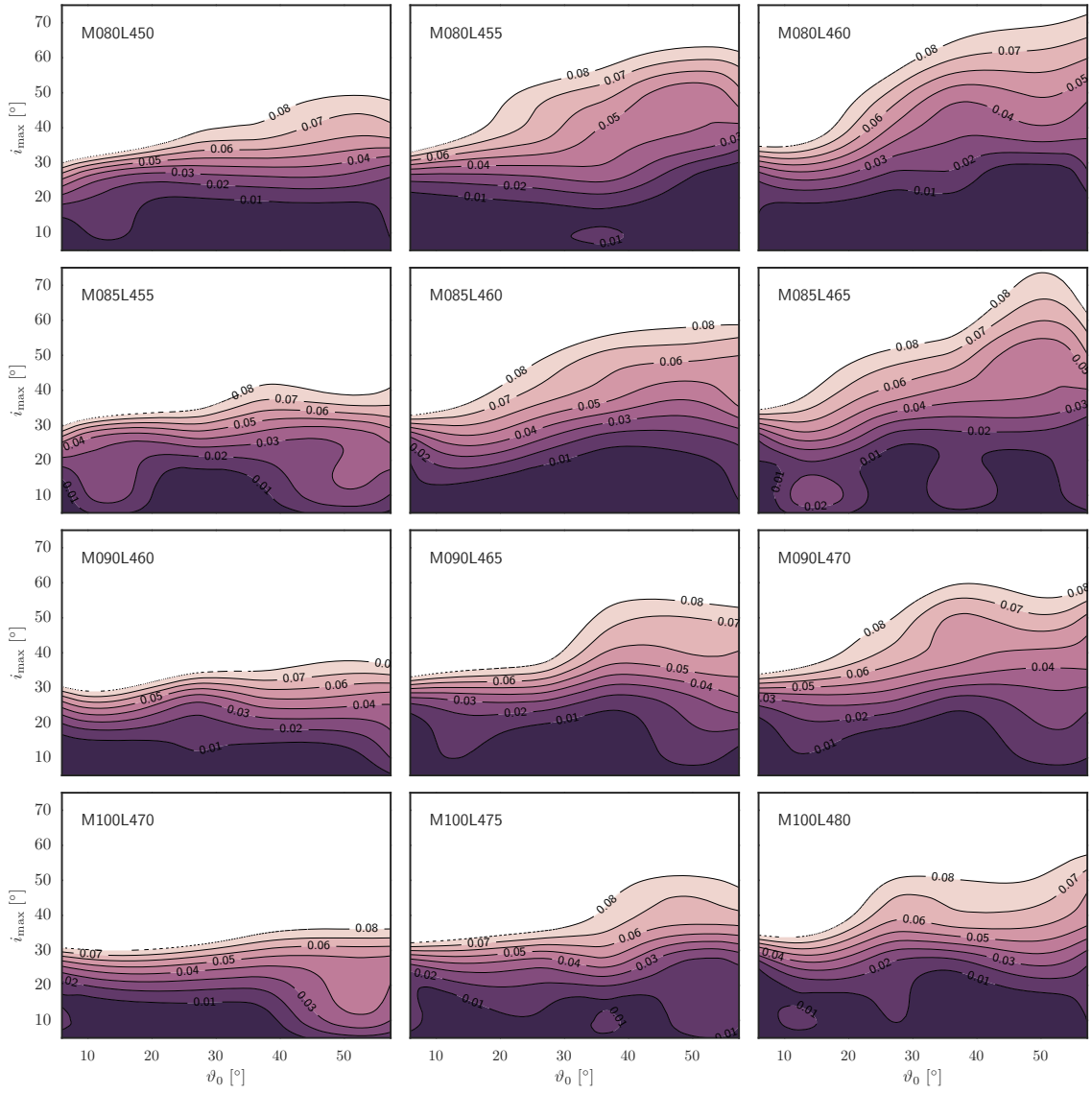

Figure 6.6: Contour plot of the standard deviation of the profile FWHM vs. launch and inclination angles, for the $\lambda = 10$ case. Only the contours within the region matching the Fine et al. (2010) results are shown. Each panel corresponds to a different combination of mass and luminosity, labelled according to the adopted convention $Mxxx Lyyy$ refers to an object of mass $10^{xx.x}$ $M_\odot$ and luminosity $10^{yy.y}$ erg s^{-1}.

Recall that the region allowed by the Fine et al. (2010) result is a measure of the torus opening angle and the torus is, in the standard model, the component that determines whether an object seen under a viewing angle i is type 1 or 2. As can be seen from Figure 6.6, in the present framework our upper limit on the half-opening angle of the torus of an AGN depends on both the mass and luminosity of the central engine.

Looking along each row in Figure 6.6 the mass is constant and the allowed regions in the $i_{\max} - \vartheta_0$ plane increase in size from left to right, as the accretion ratio increases. We would like to link this to observational results other than those of Fine et al. (2010). By construction, increasing the allowed region implies the possibility that the torus opening angle measured **from the axis** also increases. In the scenario under consideration (fixed mass), that would imply that more luminous objects have a higher probability of being observed as type 1 that less luminous counterparts. That is, there could be more torus opening angle values under which a luminous object would be classified as Type 1 than there are for fainter objects. Recent discussions in the literature suggest that this might the case. Elitzur et al. (2014) extended the analysis of Elitzur & Ho (2009) and confirmed the viability of a model where AGN broad-line emission follows an evolutionary sequence from type 1 to 2 as the accretion rate onto the central black hole is decreasing. The authors suggest that the (at least partially) controlling parameter of this spectral evolution and the torus opening angle is $L_{\rm Bol}/M^{2/3}$, that is only a function of L for the $M =$ const. case.

On the other hand, at fixed Eddington ratio (i.e., along a column in Figure 6.6), the allowed region decreases from top to bottom, i.e, with increasing mass. The Elitzur et al. (2014) results could be interpreted as implying that under fixed Eddington ratio conditions the torus opening angle (measured from the axis) should increase with decreasing mass. That can be seen by rewriting the Elitzur et al. (2014) parameter in terms of the Eddington ratio as $L_{\rm Bol}/M^{2/3} = \left(L_{\rm Bol}/M\right) M^{1/3} \propto \left(L_{\rm Bol}/L_{\rm Edd}\right) M^{1/3} = \dot{m}\ M^{1/3}$. As mentioned, for the fixed Eddington ratio case, the results for our limits are opposite to Elitzur et al. (2014). However, when considering fixed mass, our results match those of Elitzur et al. (2014).

Note here that, in the case of Elitzur et al. (2014) framework, the decrement in observed broad lines originates in a decreasing accretion rate towards the central engine, that in turn decreases the outflow rate and the object's bolometric luminosity. At sufficiently low accretion rates, the BLR and the obscuring region are quenched, running out of fuel.

We can also analyse how our findings can be explained in the context of a popular parametrization of the BLR size and the vertical size of the torus that is related to its half-opening angle, $\sigma_{\rm t}$. Some determinations of the vertical size of the torus (e.g., Simpson 2005) provide $h_{\rm t} \propto L^{1/4}$. Then, we can obtain a crude estimate of the BLR opening using (see e.g., Hönig & Beckert 2007) $\sigma_{\rm t} \sim h_{\rm t}/R_{\rm BLR} \sim L^{-1/4}$. Therefore, if we compare the

BLR aperture σ_1 and σ_2 due to two different luminosities $L_2 > L_1$, we would get

$$\frac{\sigma_2}{\sigma_1} \sim \left(\frac{L_1^{1/4}}{L_2^{1/4}} \right). \tag{6.2}$$

That means that more luminous objects would have smaller torus openings (measured from the disc). This is in agreement both with our results (at $M = \text{const.}$) and those of Elitzur et al. (2014).

The dependence of the torus height on luminosity is a modification suggested by Simpson (2005) to the model known as "receding torus", proposed by Lawrence (1991), wherein the height of the torus is constant as a function of radius. As discussed in the recent review by Bianchi et al. (2012), this dependence of the obscuring structure covering factor on the luminosity has been supported by many observational results, in different wavelengths. For instance, hard X-ray studies (e.g., Ueda et al. 2003, Akylas et al. 2006, Tozzi et al. 2006) and in the optical (e.g., Arshakian 2005, Simpson 2005, Polletta et al. 2008). Bianchi et al. (2012) point out that the receding torus model can not account for the decrease of the covering factor inferred from X-ray studies, that do not trace the dusty component of the absorber. Moreover, Lawrence & Elvis (2010) have questioned the above results, arguing that, at least in optical and IR-selected samples, such a luminosity dependence is an artifact due to the adopted definition of "obscured" and to the inclusion of low excitation AGN.

Some authors (e.g., Hönig & Beckert 2007, Nenkova et al. 2008), that support a clumpy rather than a smooth dust distribution torus, argued that the decreasing fraction

of type 2 objects at high luminosities depends not only on the decreasing torus opening angle, but also on the decreasing N_0. In Figure 6.7 we show the standard deviation of the profile FWHM vs. inclination angle obtained from our line profiles for the Nenkova et al. (2008) clumpy torus prescription. Each panel corresponds to a different combination of mass and luminosity and each line represents results for a different value of the Nenkova et al. (2008) torus model parameters $\sigma_{\rm t}$ and N_0 adopted from the Mor et al. (2009) sample. The black horizontal dashed line is the Fine et al. (2010) 0.08 dex constraint. As in Figure 6.6, the mass is constant along rows and the accretion rate is constant along columns. As in the smooth torus case, we find that the agreement (or lack thereof) with the observational constraint depends on the mass and the accretion rate separately, with better agreement (i.e., reached from a smaller ϑ_0 angle) reached for the lowest mass and larger Eddington ratio. Additionally, the curves corresponding to larger N_0 and σ cross the limiting line at smaller ϑ_0.

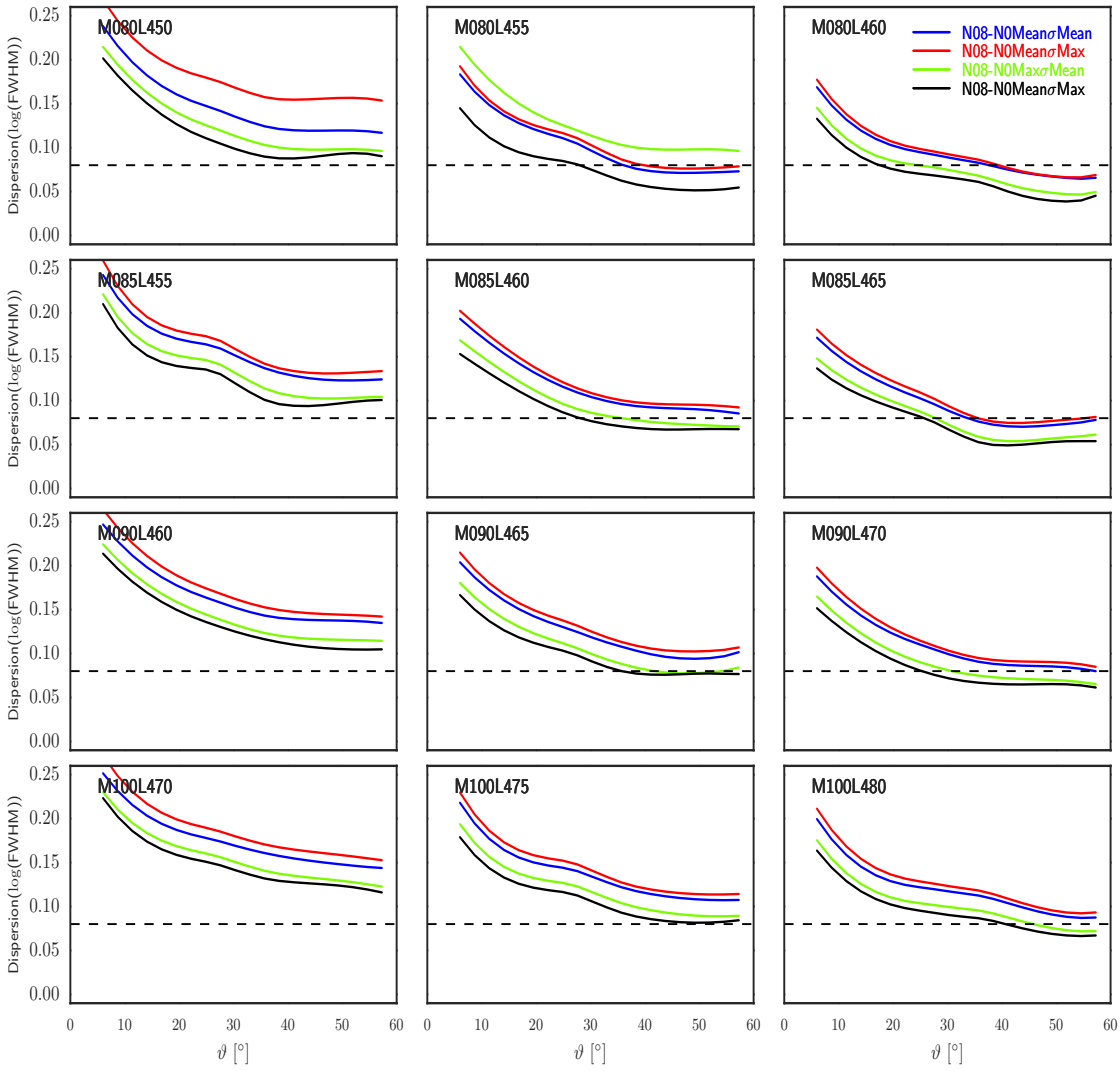

Figure 6.7: Standard deviation of the profile FWHM vs. inclination angle, using the Nenkova et al. (2008) clumpy torus prescription. The symbol code is as in Figure 6.4. Each panel corresponds to a different combination of mass and luminosity and each line represents results for a different value of the N08 torus model parameters $\sigma_{\rm t}$ and N_0. The black horizontal dashed line corresponds to the Fine et al. (2010) 0.08 dex constraint.

6.2.1 Including a Smaller Mass

We discussed above that the larger allowed range of $i_{\max}$ found for our fiducial case was expectable. Here we present the result of the same analysis done on a smaller mass, $M = 10^7$ M$_\odot$, for the same Eddington ratios applied to the other cases. Figure 6.8 shows the FWHM vs. i of the emission lines corresponding to this case, while the next two figures are different representations of the dispersion of this line measurement. In all these figures we have included a bottom row, corresponding to the $M = 10^8$ M$_\odot$ case, for comparison purposes.

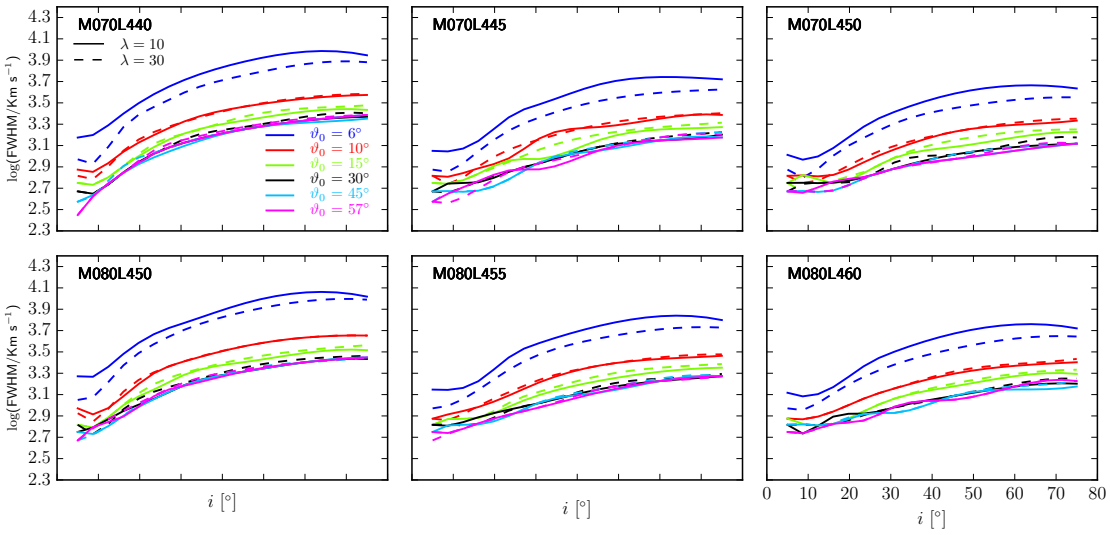

Figure 6.8: Profile FWHM vs. inclination angle for an additional smaller mass. The colour and dashing codes are the same as in Figure 6.4. Upper panel corresponds to a central object's mass $M = 10^7$ M$_\odot$, for the three Eddington ratios considered above, i.e., from left to right: $\dot{m} \sim 0.1, 0.5, 1$. The lower row represents the corresponding fiducial case results.

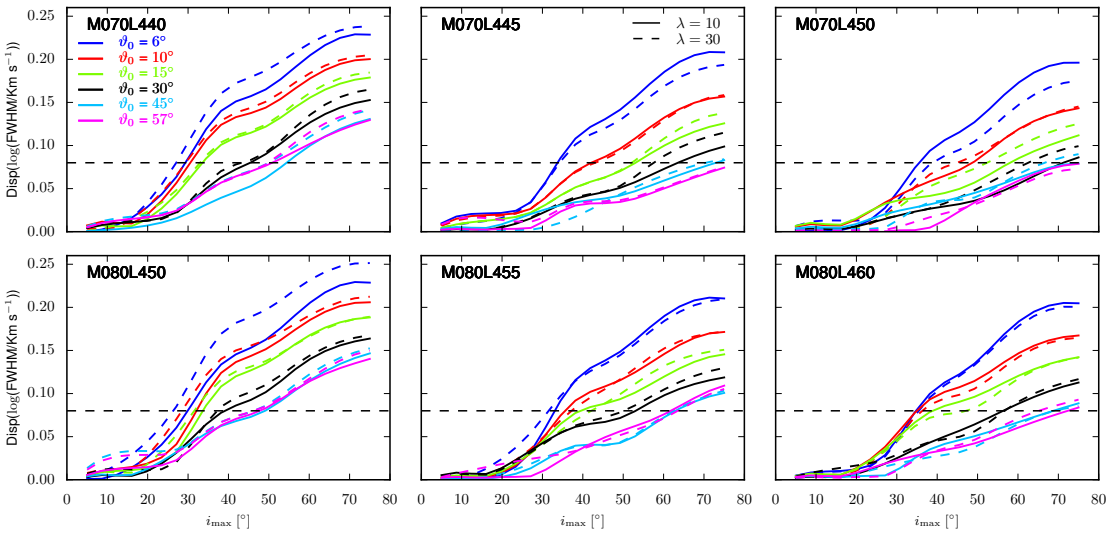

Figure 6.9: Analogous to Figure 6.5. Standard deviation of the profile FWHM vs. $i_{\max}$. The upper and lower rows correspond to the $M = 10^7$ M$_\odot$ and $M = 10^8$ M$_\odot$ respectively, and the columns correspond, as before, to $\dot{m} \sim 0.1, 0.5, 1$.

Figure 6.9 shows the dispersion of line FWHM vs. $i_{\max}$. Each individual curve corresponds to a given ϑ_0 value. In Figure 6.10, on the other hand, we present the contour plots of $\sigma_{\rm fwhm}$ in the $\vartheta_0 - i_{\max}$ plane.

The analysis of the two figures shows that the smaller mass results follow the trend previously observed. From Figure 6.9 it is evident that, as the launch angle ϑ_0 increases, the corresponding curve intercepts the observational constraint line at a (slightly, in some cases) larger $i_{\max}$ value. Figure 6.10 indicates that the allowed region in the $\vartheta_0 - i_{\max}$ plane increases with decreasing mass. For fixed mass, it implies that, as the luminosity

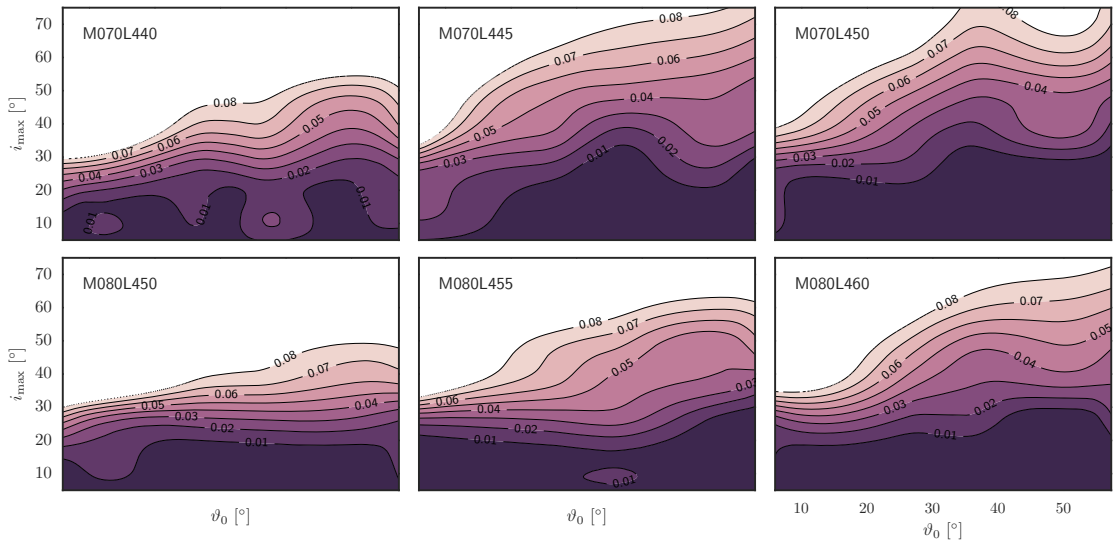

Figure 6.10: Contour plot of the standard deviation of the profile FWHM vs. launch and inclination angles. The upper panels correspond to an object of mass $M = 10^7$ M$_\odot$ with $\lambda = 10$. The three luminosity values are, from left to right, $L = 10^{44}, 10^{44.5}, 10^{45}$ erg s^{-1}, corresponding to $\dot{m} \sim 0.1, 0.5, 1$. The lower panels, corresponding to a $M = 10^8$ M$_\odot$ case, are included for ease of comparison. As before, only the contours within the region matching the Fine et al. (2010) results are shown.

(or, equivalently, the Eddington ratio) increases, the range of viewing angles under which an object can be characterized as Type 1 also increases. In other words, the torus opening angle decreases.

6.3 Comparing results for different λ values

In previous sections we have shown that the line profiles, and so their FWHMs and corresponding dispersions, depend only weakly on the dimensionless angular momentum parameter. Here we discuss this result in terms of the velocity and magnetic fields gov-

erning the line formation in the framework of our model.

Recall that, as discussed in Chapter 3, the angular momentum l is constant along a field line (and so is its dimensionless version λ). Moreover, as also discussed in Chapter 3, in the EBS92 model (and, therefore in ours), the adopted free parameters are λ and ϑ_0, while κ is related to λ by a nonlinear correspondence, shown in Equation (3.95).

Thus, if we consider cases of equal masses and luminosities but different λ, and additionally assume same launch angles (i.e., same ξ_0' values) and density structures, we can see that any difference can only be due to differences in the magnetic fields at the disc surface.

Comparing the profiles presented in Figure 6.1, it is evident that the differences in shape and line-width between results based on the two different λ values adopted depend on ϑ_0 but very mildly (if at all) on the viewing angle. For i = const., the difference is maximum for the minimum adopted value of ϑ_0 and becomes negligible as the parameter increases. For ϑ_0 = const., the difference between profiles remain fairly constant along the whole range. There are a few departures, generally at the lowest ϑ_0 and for the smallest i, but those do not invalidate the general behaviour. As will be shown below, the fact that the different λ values yield profiles independent of the viewing angle is a natural consequence of the model.

Similarly, the shapes and FWHMs show maximum differences for $\vartheta_0 = 6^\circ$ and almost negligible for larger ϑs, as can be seen from Figure 6.4. The dispersion of linewidths

plotted in Figure 6.5, show also that the larger differences occur, in general, at smaller ϑ_0 values, with a few cases where noticeable differences are seen at large ϑ_0 angles.

The question is now, why the results from the two different λ values seem to be more distinguishable for smaller ϑ_0? To analyse the issue, we use the fact that $\lambda =$ const. along a field line. Thus, we can evaluate it at a convenient position, e.g., $\chi = 0$ or $\chi = \chi_{\rm A}$.

We start with the dimensionless angular momentum expression, introduced in Chapter 3, Equation (3.82):

$$\lambda = \frac{r\, v_\phi - r\, \frac{B_\phi}{k}}{(GMr_0)^{1/2}}, \tag{6.3}$$

where we have explicitly written in the numerator the angular momentum l, that is constant along a field line, introduced in Equation (3.35). We can now express r in terms of the self-similar coordinates, that is $r = r_0\xi(\chi)$. The mass-to-magnetic flux ratio satisfying $k/4\pi = \rho v_{\rm p}/B_{\rm p}$ is also constant along a field line and can be replaced by the dimensionless quantity $\kappa = k(1+\xi_0'^2)^{1/2}\frac{(GM/r_0)^{1/2}}{B_0}$, where $B_0 = B_{\rm p}(\chi = 0)$. Expression (6.3) is now

$$\lambda = \frac{r_0\xi\; v_\phi - r_0\xi\; \frac{B_\phi\,(1+\xi_0'^2)^{1/2}}{\kappa B_0}\left(\frac{GM}{r_0}\right)^{1/2}}{(GMr_0)^{1/2}}, \tag{6.4}$$

where we can recognize in the first term the function $g(\chi)$, related to the azimuthal velocity component through $v_\phi(r_0,\chi) = g(\chi)\sqrt{GM/r_0}$. The second term is simplified to $\frac{B_\phi\,(1+\xi_0'^2)^{1/2}}{\kappa B_0}$. Choosing $\chi = 0$ in expression (6.3) yields

$$\lambda = \xi(0)\left(g(0) - \frac{B_\phi(0)\,\sqrt{(1+\xi_0'^2)}}{\kappa B_{\rm p}(0)}\right), \tag{6.5}$$

where we recall that the conditions satisfied at the disc surface are $g(0) = \xi(0) = 1$. Replacing these values in Equation (6.5) allows to obtain an expression for the initial magnetic field from conserved quantities:

$$\left|\frac{B_\phi(0)}{B_{\rm p}(0)}\right| = \frac{(\lambda-1)\,\kappa}{\sqrt{(1+\xi_0'^2)}} = (\lambda-1)\,\frac{2}{\sqrt{(1+\xi_0'^2)}}\left(\frac{3}{2\lambda-3}\right)^{3/2}, \tag{6.6}$$

where the last equality is obtained from the previous using $\kappa = 2(3/(2\lambda-3))^{3/2}$, that is the expression of κ corresponding to the adopted model. Expression (6.6) is exact for $\chi = 0$, and is the same as Equation (5.1a) in BP82, who give it as (approximately) valid in the vicinity of the disc. The above expression relates to ϑ_0 via $\xi_0' = \cot\vartheta_0$, presented in section 3.7.

If Equation (6.6) is taken as a function of λ, it gives the expected behaviour of the ratio of the magnetic field components at the disc surface and shows it to be decreasing with increasing λ. That is, for any given value of the parameter λ there is a definite value of the ratio $\left|B_\phi(0)/B_{\rm p}(0)\right|$.

6.4 Discussion

Note that the angle $i_{\max}$ used throughout this work is measured from the polar axis (i.e, it is the complementary to the angle $\sigma_{\rm t} = \tan^{-1} h_{\rm t}/r_{\rm t}$ defined above). In terms of that parameter, the receding torus model posits that the torus opening angle of more luminous objects are larger. However, although for constant mass our results permit that trend, in

general our results suggest that the torus opening angle of more luminous objects is smaller than that of fainter counterparts. But, as mentioned in Section 6.2, at fixed mass the trend is that suggested by Elitzur et al. (2014), i.e., that the torus opening angle decreases with luminosity. That suggests that our model is, in its general conception, adequate although some of the parameter choices have to be reviewed for it to better represent real cases.

For example, the tilt of the emitting region with respect to the equatorial plane was chosen to match that of MC97, which was in turn chosen based on a BAL quasar fraction of ~ 0.1, a value that has been updated (e.g., Allen et al. 2011). More recent values put the BAL fraction as large as ~ 0.25 of the quasar population, implying an emission region with a steeper slope. In such a case, the effective length over which the emission is obtained would increase and be at higher distances above the disc. This would affect both the velocities and their derivatives, thus affecting Q and the optical depth, ultimately modifying the FWHM of the line profiles, but perhaps not as much their shapes. Here we recall that this slope can be a function of the radius, as opposed to the fixed value adopted in this work. Adopting a function that smoothly increases with radius (similar to the bowl-shaped BLR geometry in the model proposed by Goad et al. (2012)) instead of a constant slope, would make the streamlines intercept the emission region at higher heights from the disc plane, which would produce broader profiles, and probably with more dispersion. This could provide a constraint to the families of possible curves to

adopt as the base of the emission region.

The spatial profile of the density could be reviewed or adjusted, too. Here we have to consider both the radial and the vertical structures, that are decoupled in the adopted model. As discussed in Chapter 4, the density structure in the radial direction is such that $n(r) \propto r^{-2}$, but a closer value to the corresponding Shakura & Sunyaev (1973) relevant accretion disc region would be a power-law exponent $-3/2$. Other possibilities involve changing the underlying disc model, adopting, e.g., a slim disc instead of the geometrically thin and optically thick disc of Shakura & Sunyaev (1973). Slim discs were developed in the pseudo-Newtonian limit by Abramowicz et al. (1988) and are more suitable for larger accretion rates ($\dot{m} \gtrsim 0.3$, e.g., Abramowicz & Fragile (2013)).

In the z direction, the density drops off away from the base of the emission according to a half-Gaussian dependence, regulated by both the height and the thickness of the emission region. The former depends on the geometry of the region, discussed in the previous paragraph. Any modification to the latter should still ensure that it satisfies $l_{\rm em} \ll z_{\rm em}$. Reducing $l_{\rm em}$ from the expression given in Equation (4.18), an even smaller $l_{\rm em}$ would decrease the size of the region where line emission is efficient.

The turbulent velocity has been chosen to be constant, but it also can depend on the radial coordinate. For instance, it has been shown that magnetorotational instability (MRI, Balbus & Hawley 1991) provides a plausible mechanism to develop turbulence and transport angular momentum in discs, due to their differential Keplerian rotation.

Another point to consider is that we did not explore changes in the photoionization calculations. The CLOUDY runs yielding the source function results used in this work were obtained adopting specific prescriptions for the various parameters in the code that define the photoionization state of the gas. The ionization and excitation structure of the gas depend on the SED, the number density n_γ of ionizing photons irradiating the gas, the metallicity and number density n of the gas. Changes in the adopted prescription of any (or all) of these parameters will lead to a different structure of the gas and its ionization and excitation states, in the disc and wind. For example, for most of their model cases Murray & Chiang (1997, 1998) employed a (modified in the X-ray region) Mathews & Ferland (1987) SED, that is still very popular in the literature. Adopting a different SED would affect the ionization structure in the wind, but in a wind scenario there is not total freedom in choosing an alternative. A distribution too strong in X-rays compared with the UV portion may preclude the formation of a wind, because the gas is overionised before it can be accelerated. In such a case, the higher ionization lines, such as C IV, would instead be produced in the low-velocity gas, that is illuminated by a continuum that is now strong in the extreme UV and in the X-rays (Leighly 2004).

7 Summary and Conclusions

In this work we have studied AGN broad emission line profiles with a model that combines an improved version of the accretion disc wind model of Murray & Chiang (1997) with the hydromagnetic driving of Emmering et al. (1992). The dynamics of these self-similar MHD outflows is characterized by two parameters, e.g., the dimensionless angular momentum λ, and the wind-launching angle with respect to the disc plane ϑ_0. We first analysed a fiducial case, with $M = 10^8$ $\mathrm{M}_\odot$ and $L = 10^{46}$ erg s^{-1} for the mass and luminosity of the central object respectively. For this configuration, we constructed a series of model runs parametrized by the wind-launching and viewing angles, while keeping $\lambda = 10$ fixed.

Within the fiducial case we explored part of the parameter space analysing the effect on the results when a given parameter is changed. Thus, changing the density at the base of the emitting region (and, consequently changing the opacity) translates into relatively small changes in the line profiles, due to the effect of the velocity field. This dependence is weaker at smaller viewing angles, and becomes stronger moving towards more edge-on

cases.

We have compared the dispersions in our model C IV linewidth distributions to observational upper limits on that dispersion. Those limits translate to an upper limit to the half-opening angle of the putative torus feature that is part of the standard model describing the AGN phenomenon. To achieve this, we constructed contour plots of the dispersion of $\log(\mathrm{FWHM})$ in the $\vartheta_0 - i_{\max}$ plane, capped with the Fine et al. (2010) observed upper limit dispersion, defining in this way a boundary line $i_{\max}$ vs ϑ_0, below which an object can be seen as Type 1.

We have corrected an initially-estimated maximum torus half-opening angle of about 47°, reported in Chajet & Hall (2013). This value had been obtained based on a mistaken interpolation routine of the CLOUDY-generated source function points. The revised maximum torus half-opening angle is larger, about 75°. In fact, the maximum torus half-opening angle is an increasing function of the wind launching angle ϑ_0.

We also considered two alternative obscuring structures: a clumpy torus and a warped disc. In both cases the limiting viewing angle to integrate over was always 90°, as opposed to the differential $i_{\max}$ that was used in the putative smooth torus case. Except for this difference, the two alternative possibilities yielded similar constraints to those obtained with the traditional torus.

We further extended the analysis to consider a range of black hole masses and luminosities. In a similar manner to the approach adopted in the fiducial case, we computed,

for different combinations of mass and luminosity of the central object within that range, line profiles corresponding to the same combinations of wind-launching and viewing angles used before.

Additional series of model runs with different values of λ suggest, on the other hand, that the profile linewidths and corresponding dispersions depend only mildly on this parameter.

We also found that many of the profile line characteristics, such as the FWHM, the (blue- or red-) shift with respect to the systemic velocity, and the degree of asymmetry, depend not only on the viewing angle (a parameter external to the object, depending on the relative geometry source-observer), but also on the launching angle, a parameter that is intrinsic to the object. Additionally, our results suggest that large values of ϑ_0 are preferred.

We then studied, for each case, the dispersion of $\log(\mathrm{FWHM})$ and imposed the observational results of Fine et al. (2010). Again, contour plots of the dispersion of $\log(\mathrm{FWHM})$ in the $\vartheta_0 - i_{\max}$ plane, constrained with the Fine et al. (2010) results, were used to determine the torus half-opening angle appropriate for each case. The picture that emerged is that the dispersion of the linewidth depends on both the mass of the central object and the Eddington ratio at which it is fed. At fixed mass, the maximum allowed torus half-opening angle (measured from the axis) increases with increasing Eddington ratio (equivalent, under the fixed mass condition, to increasing luminosity). That can

be interpreted as objects with larger accretion rates having a higher probability of being observed as Type 1 AGN than those fed at a lower rate. At fixed Eddington ratio, the probability that an object will be seen as Type 1 decreases with increasing mass.

Ultimately, this work links theory with observational results, by imposing an observational constraint to the distribution of a property of the emission lines emerging from the BLR. The BLR is modelled through a physically well motivated wind description and the observational constraint on the dispersion of the line-width distribution allows it to be translated into a constraint on the geometry of the obscuring structure that is invoked to explain the Type 1/Type 2 dichotomy among AGNs.

7.1 Future Directions

We have identified a number of possible directions that could expand this study. Most of them will require modifying either the numerical code applied, the underlying model, or both. In addition, it is also possible to further exploit the currently available set of simulations and evaluate some properties, not yet analysed, of those profiles and compare the results to observational equivalents in the literature. For instance, we can compare the equivalent widths and line asymmetry of the line profiles used in this work to the results reported by Richards et al. (2011).

An important task is to analyse the self-consistency of the radial emissivity applied here and, possibly, to run new CLOUDY simulations, using an updated version of that

software.

Future work will also consider applying the model to other high-ionization lines, such as Si IV, as well as low-ionization lines, such as Mg II. One interesting further extension of a Mg II simulation set is that it would be possible to explore the third moment of the resulting line-width distribution and compare it to the observational results discussed by Fine et al. (2008). Additionally, for any transition studied, we would also like to explore the effect of different sizes of the line-emitting region. This quantity, given by the ratio $r_{\rm max}/r_{\rm min}$, was fixed throughout the present work. However, the amount of line shift and the degree of asymmetry of the line profiles are functions of it (e.g., Flohic et al. 2012). Therefore, it would be important to study how different lines are effected by this parameter.

The present work does not include the treatment of resonance scattering of continuum photons or general relativistic (GR) effects. The inclusion of resonance scattering has the effect of broadening the line profiles, but it might have a negligible impact on the statistics of the line-width distribution. Considering scattered photons would become necessary for a study that included not only emission, but also absorption lines.

As mentioned in the text, the relativistic MHD case has been studied by several authors, often in the context of jet launching and collimation and in relation to several different astrophysical environments. Different authors have considered the problem in steady and time-dependent regimes. In the relativistic MHD framework, the line forma-

tion problem has been considered in the X-ray range in relation to the iron K-line (e.g. Müller & Camenzind 2004). However, to our knowledge, a combination of a relativistic, improved version of MC97 (e.g., Flohic et al. 2012) with relativistic MHD driving has not been yet explored in the literature. We consider that as one of the possible future lines of work to pursue. Due to the stratification of the BLR radial ionization profile, we expect that the inclusion of GR effects would affect more strongly high-ionization lines, emitted predominantly at smaller radii than low-ionization lines.

A The radiative transfer equation

When radiation propagates through a medium it is transformed by emission and absorption processes occurring there. The result is the observed spectrum, including spectral lines. The physics of such a transformation is mathematically described by a differential equation known as radiative transfer equation. Here we provide a very concise overview on the radiation transfer problem. Among the vast literature on the topic, a classical reference is the book by Rybicki & Lightman (1979).

The flux of energy dE through an area dA normal to the direction of photon propagation within the solid angle $d\Omega$ during the time interval dt in the frequency interval $d\nu$ is given by

$$dE = I_\nu \, dA \cos\theta d\nu d\Omega dt, \tag{A.1}$$

where the specific intensity $I_\nu = I_\nu(\mathbf{r}, \mathbf{n}, t)$ defines the radiation field. In the cgs system, the units of I_ν are erg s^{-1} cm^{-2} Hz $^{-1}$ sr^{-1}.

Using conservation of energy for the radiation field it is easy to show that the intensity is conserved in free space. In a medium, however, conservation of energy implies that

the intensity changes along its path through the material, due to the interactions between the radiation field and the matter. Figure A.1, adopted from Bradt (2004), shows the geometry for constructing the radiative transfer equation. Radiation originating from a background source at some temperature T_0 is incident on a uniform cloud, of depth Λ at temperature $T_{\rm s}$, and optical depth τ_Λ that lies between the observer and the background source.

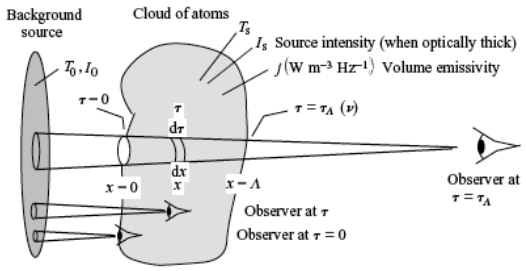

Figure A.1: Geometry for the radiative transfer equation. The background surface emits with specific intensity I_0 and the intervening gas cloud emits thermal radiation with specific intensity $I_{\rm s}$ (refer to as S_ν in the text) when it is optically thick. An observer in the cloud at position x, or optical depth τ viewing leftward will detect radiation from the cloud atoms at lesser τ and from the background source to the extent it is not absorbed by the cloud. Note that the units in the figure are in the international system, whereas most of the units in this works are in the cgs system. Adopted from Bradt (2004).

In general, the initial intensity of a beam decreases if photons are either absorbed or scattered out of the it, and increases if photons are either emitted or scattered into the beam. The rates at which these changes occur are defined in terms of coefficients specific to each process, which, in turn, depend on the radiation field.

Over a distance ds in the direction of the beam , the specific intensity increases due to photon emission by an amount, $j_\nu ds$, and decreases due to absorption by an amount proportional to its magnitude, $k_\nu ds I_\nu$.

$$\mathbf{n} \cdot \nabla I_\nu = -k_\nu I_\nu + j_\nu, \tag{A.2}$$

where j_ν is the emission coefficient (energy emitted per unit time per unit solid angle per unit volume in direction $\mathbf{n}$) and $k_\nu = \kappa_\nu \rho$ is the absorption coefficient, where ρ is the mass density of the medium (in g cm^{-3}) and κ_ν is the opacity, defined by

$$\kappa_\nu = \sigma n / \rho, \tag{A.3}$$

where n is the number density of particles and σ is the cross section for interaction. Opacity is the probability of a photon being absorbed (or scattered) by matter.

The transfer equation takes a particularly simple form if the optical depth is used instead of the physical path-length s. The optical depth τ_ν along a path $\mathbf{r} = \mathbf{r}(s)$ from the source to the observer is defined by

$$d\tau_\nu = k_\nu ds. \tag{A.4}$$

Re-expressing the radiative transfer equation in terms of the τ_ν separates the terms that are properties of the matter from those of the radiation:

$$\frac{dI_\nu}{d\tau_\nu} = -I_\nu + S_\nu, \tag{A.5}$$

where S_ν, the source function, defined as the ratio of the emission coefficient to the absorption coefficient,

$$S_\nu = j_\nu / k_\nu,$$

characterizes the medium. Note that the source function has the same units as the intensity.

In the transfer equation, both the intensity and the source function are functions of the optical depth, which increases along the path. The formal solution has the form:

$$I_\nu(e^{\tau_\nu}) = I_\nu(0)e^{-\tau_\nu} + \int_0^{\tau_\nu} S_\nu(\tau'_\nu)e^{-(\tau_\nu - \tau'_\nu)}d\tau'_\nu. \tag{A.6}$$

Each term has a simple physical interpretation. The first term in the right hand side, $I_\nu(0)e^{-\tau_\nu}$, represents the attenuation of the incident radiation by the factor $e^{-\tau_\nu}$ due to absorption. The last term is the integrated source modulated by a factor that accounts for increase due to emission ($e^{\tau'_\nu}$) and for decrease due to absorption ($e^{-\tau_\nu}$).

This formal solution can not be further simplified without more information on the source function. One possible simplification is to assume that the material is homogeneous over the path-length ds, such that $S_\nu(\tau) = S_\nu$. The solution (A.6) reduces, then, to

$$I_\nu(\tau_\nu) = I_\nu(0)e^{-\tau_\nu} + S_\nu(1 - e^{-\tau_\nu}). \tag{A.7}$$

It is interesting to analyse the two limiting cases: $\tau_\nu \ll 1$ and $\tau_\nu \gg 1$. When $\tau_\nu \ll 1$

the medium is optically thin.

$$I_\nu(\tau_\nu) = I_\nu(0) + (S_\nu - I_\nu(0))\tau_\nu. \tag{A.8}$$

When, on the other hand, $\tau_\nu \gg 1$, the medium is optically thick and the emergent radiation is due to the source function only:

$$I_\nu(\tau_\nu) = S_\nu. \tag{A.9}$$

B Differential Covering Factor for Tilt-only Discs

Below we outline the evaluation of $dC(i)$ for arbitrary disc tilt angle θ, to within the numerical factor required so that the total probability in a given situation is unity. Recall that in the following analysis the covering fraction is a function of the azimuth, while it is azimuthally integrated in the calculations of LE10.

Define the line of nodes of the tilted outer disc relative to the inner disc to be at $\phi = 0$. Then at each ϕ, the obscuration from the outer disc extends an angle θ' above the inner disc given by $\sin\theta' = \sin(\theta)\sin(\phi)$ (sine rule for spherical right triangles); see Figure B.1.

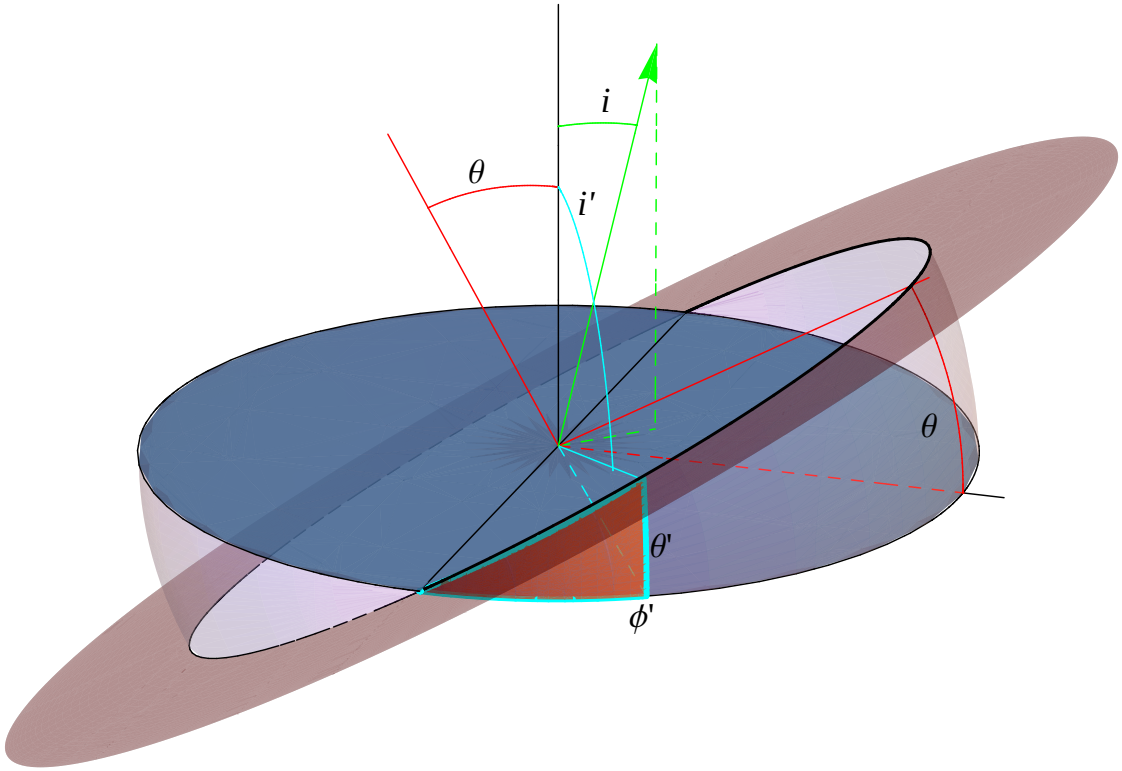

Figure B.1: Tilt-only disc (warped but not twisted). The outermost disc (shown as an annulus) is tilted at an angle θ with respect to the inner disc. The transition from outer disc to inner disc occurs over a range of radii in reality, but is shown here happening at a single radius. Adopting the azimuth of the ascending node as $\phi = 0$, at azimuth ϕ' the obscuration from the outer disc extends an angle θ' above the inner disc given by $\sin(\theta') = \sin(\theta)\sin(\phi')$. The equivalent polar angle $i' = \frac{\pi}{2} - \theta'$ is given by $\cos(i') = \sin(\theta)\sin(\phi)$. At each azimuth, the light purple shading represents the obscuration due to the tilted disc (which takes the form of two wedges of maximum width θ). The light shadow represents the obscuration due to the tilted disc at all azimuths. The region at azimuths $0 \leq \phi \leq \phi'$ has a darker shadow to emphasize the angles intervening in the θ' calculation.

The equivalent polar angle $i' = \frac{\pi}{2} - \theta'$ is given by $\cos(i') = \sin(\theta)\sin(\phi)$. Solving the latter equation for the maximum unobscured ϕ at a given i, $\phi_{\max}(i, \theta)$, yields

$$\phi_{\max}(i, \theta) = \arcsin[\cos(i)/\sin\theta], \tag{B.1}$$

where $0 < \phi_{\max}(i, \theta) < \frac{\pi}{2}$.

For $0 < \theta < \frac{\pi}{2}$, there is an unobscured polar cap (at $i < \frac{\pi}{2} - \theta$) and a region where obscuration increases from 0% at $i = \frac{\pi}{2} - \theta$ to 50% at $i = \frac{\pi}{2}$. The differential solid angle in each region is:

$$dC\left(i < \frac{\pi}{2} - \theta\right) = 2\pi\sin(i)di \tag{B.2}$$

$$\begin{aligned} dC\left(\frac{\pi}{2} - \theta < i < \frac{\pi}{2}\right) &= \sin(i)di\left(\pi + 2\int_{\phi=0}^{\phi_{\max}(i,\theta)} d\phi\right) \\ &= \sin(i)di\left(\pi + 2\arcsin\left[\frac{\cos(i)}{\sin\theta}\right]\right) \end{aligned} \tag{B.3}$$

For $\frac{\pi}{2} < \theta < \pi$, there is a polar cap of complete obscuration $(i < \theta - \frac{\pi}{2})$ and a region where obscuration decreases from 100% at $i = \theta - \frac{\pi}{2}$ to 50% at $i = \frac{\pi}{2}$. The differential solid angle in the partially unobscured region is:

$$\begin{aligned} dC\left(\frac{\pi}{2} + \theta < i < \pi\right) &= \sin(i)di\left(\pi - 2\int_{\phi=0}^{\phi_{\max}(i,\theta)} d\phi\right) \\ &= \sin(i)di\left(\pi - 2\arcsin\left[\frac{\cos(i)}{\sin\theta}\right]\right) \end{aligned} \tag{B.4}$$

For $0 < \theta < \frac{\pi}{2}$, large i values are underrepresented, while small i values are underrepresented for $\frac{\pi}{2} < \theta < \pi$. At $\theta = \frac{\pi}{2}$, the half of the hemisphere with $0 < \phi < \pi$ is obscured,

which leads to a uniform 50% reduction in the probability of observing the quasar along every sightline as compared to the no-obscuration case.

B.1 Random orientations with $0 \leq \theta \leq \frac{\pi}{2}$.

Here we analyse in more detail a restricted variant of the model where instead of a fixed tilt angle θ, a distribution of such angles randomly distributed in solid angle from $0 \leq \theta \leq \frac{\pi}{2}$ is considered. Combining equations B.2 and B.3 we obtain:

$$dC(i) = \sin(i)di \left[\int_{\theta=0}^{\frac{\pi}{2}-i} 2\pi \sin\theta d\theta + \int_{\theta=\frac{\pi}{2}-i}^{\frac{\pi}{2}} \left(\pi + 2\arcsin\left[\frac{\cos(i)}{\sin\theta}\right] \right) \sin\theta d\theta \right], \tag{B.5}$$

which becomes

$$dC(i) = \sin(i)di \left[2\pi - \pi\cos\left(\frac{\pi}{2} - i\right) + 2\int_{\theta=\frac{\pi}{2}-i}^{\frac{\pi}{2}} \arcsin\left[\frac{\cos(i)}{\sin\theta}\right] \sin\theta d\theta \right] \tag{B.6}$$

From $dC(i)$ we define $P(i)$, the probability of being unobscured, as

$$P(i) = \frac{dC(i)}{2\pi\sin(i)}. \tag{B.7}$$

In the text, we comment on the results of combining the latter expression with equations 5.3 and 5.4 to perform the same analysis applied in the Fine at al. case.

C Glossary

- $a(r)$: area factor at cylindrical radius r
- $\mathbf{A}$: vector potential
- β: half-opening angle of the emission region
- $\mathbf{B} = (B_{\rm r}, B_\phi, B_{\rm z})$: magnetic field
- $B_{\rm p}$: poloidal (r-z-plane) component of the magnetic field
- c: speed of light in a vacuum
- $c_{\rm s}$: local speed of sound
- χ: self-similar independent coordinate
- χ_i: abundance of the element being considered
- $d\ell = dz \cos\beta / \cos\iota$: path element through the emitting region along the line of sight to the observer

- η_i: ionization fraction of the ion being considered
- e: electric charge in esu (electrostatic unit)
- $\mathbf{E}$: electric field
- f: transition's oscillator strength,
- $f(\chi)$: self-similar scaling of the velocity poloidal component along a field line
- G: gravitational constant
- $g(\chi)$: self-similar scaling of the velocity azimuthal component along a field line
- h: specific enthalpy
- $h_{\rm t}$: torus height
- ι: local inclination angle
- i: viewing angle
- $i_{\rm max}$: torus opening angle (measured from the polar axis)
- I_ν: specific intensity
- J: determinant of the Jacobian matrix of the transformation $(r, z) \rightarrow (r_0, \chi)$ (Chapter 3)

- k: mass loading factor
- k_0: line opacity
- $k_{\rm B}$: Boltzmann's constant
- $\kappa_{\rm th}$: thermal diffusivity
- λ: dimensionless specific angular momentum
- Λ: strain tensor
- $l = l(\Psi)$: angular momentum invariant
- $l_{\rm em}(r)$: thickness of the emission region at cylindrical radius r
- $\mathcal{L}$: typical length scale of the fluid
- $L_\odot$: Solar luminosity
- L_{1350}, $L_{\rm UV}$: Quasar ionizing luminosity
- m: square of the Mach-Alfvén number
- $m_{\rm p}$: proton mass
- $M_\odot$: Solar mass
- M, $M_{\rm BH}$: black hole mass

- μ: mean atomic weight
- $n(r, z)$: hydrogen number density at the cylindrical coordinates (r, ϕ, z)
- $n_0(r)$: hydrogen number density at the base of the emission region
- $\hat{\mathbf{n}}$: unit vector in the direction of the observer
- ν: frequency
- ν_0: central frequency of the transition
- ν: kinetic diffusivity Chapter 3)
- $\nu_{\rm D}$: Doppler-shifted central frequency of the line
- $\nu_{\rm m}$: magnetic diffusion coefficient
- $\xi(\chi)$: self-similar dependent coordinate
- $\xi_0' = \xi'(\chi = 0) = \cot \vartheta_0$: first derivative of the self-similar dependent coordinate evaluated at the disc plane
- Ω: angular velocity
- $\varphi_\nu(r, \phi, z)$: line profile function at the cylindrical coordinates (r, ϕ, z)
- $\Phi_{\rm g}$: gravitational potential

- p: thermal pressure
- Pr: Prandtl number
- $\mathrm{Pr_m}$: magnetic Prandtl number
- Ψ: flux function
- q_{tt}: 'thermal Q'
- Q: line-of-sight gradient of the line-of-sight wind velocity
- r_0: self-similar radial coordinate
- r_{max}: BLR outer radial boundary
- r_{min}: BLR inner radial boundary
- Re: Reynolds number
- $\mathrm{Re_m}$: magnetic Reynolds number
- ρ: matter density
- r_{A}: Alfvén radius
- S: related to the true gravitational potential (Chapter 3)
- S_ν: source function

- $\sigma_{\rm e}$: electric conductivity of the plasma
- $\sigma_{\rm t}$: torus half- opening angle (measured from the disc plane)
- $\sigma_{\rm T}$: Thomson scattering cross-section for an electron
- τ_ν: optical depth
- T: temperature
- T: related to the effective gravitational potential (Chapter 3)
- $t_{\rm dyn}$: dynamical time
- $t_{\rm sc}$: sound crossing time
- ϑ_0: wind launching angle
- ϑ: wind angle at the base of the emission region
- $\mathcal{U}$: typical velocity of the fluid
- $\mathbf{v} = (v_{\rm r}, v_\phi, v_{\rm z})$: velocity field
- $v_{\rm A}$: Alfvén speed
- $v_{\rm D}$: Doppler velocity
- v_∞: asymptotic velocity

- $v_{\rm p}$: poloidal (r-z-plane) component of the velocity
- $v_{\rm sh}$: shear velocity
- $v_{\rm tt}$: thermal plus turbulent velocity
- $z_{\rm em}(r)$: height of the emission region at cylindrical radius r

Bibliography

Abramowicz, M.A., Czerny, B., Lasota, J.-P., Szuszkiewicz, E., 1988, ApJ., 332, 646

Abramowicz M. A., Fragile P. C., 2013, LRR, 16, 1

Akylas A., Georgantopoulos I., Georgakakis A., Kitsionas S., Hatziminaoglou E., 2006, A&A, 459, 693

Alfvén H., 1943, ArA, 29, 1

Allen, J. T., Hewett, P. C., Maddox, N., Richards, G. T., Belokurov, V., 2011, MNRAS, 410, 860

Alonso-Herrero A., Sanchez-Portal M., Ramos Almeida C., et al. 2012, MNRAS, 425, 311

Antonucci, R. R. J., Miller, J. S. 1985, ApJ, 297, 621

Antonucci, R. 1993, ARA&A, 31, 473

Arav, N., Barlow, T. A., Laor, A., Sargent, W. L. W., Blandford, R. D., 1998, MNRAS, 297, 990

Arshakian T. G., 2005, A&A, 436, 817

Balbus, S. A., Hawley, J. F., 1991, ApJ, 376, 214

Baldwin, J. A., Ferland, G. J., Korista, K. T., Hamann, T., Dietrich, M. 2003, ApJ, 582, 590

Barenblatt, G. I., 1996, Similarity, Self-Similarity and Intermediate Asymptotics, Cambridge University Press, Cambridge, UK

Barthel, P. D., 1989, ApJ, 336, 606

Batchelor, G.K., 1967, An Introduction to Fluid Mechanics. Cambridge University Press, Cambridge

Begelman, M. C., Li, Z. Y. 1994, ApJ, 426, 269

Beskin, V.S., Istomin, Ya.N., Pariev, V.I., 1992, in Extragalactic Radio Sources – From Beams to Jets. pp. 45-51. Cambridge University Press, Cambridge

Beskin, V.S., Kuznetsova, I.V., Rafikov, R.R., 1998, MNRAS, 299, 341

Beskin, V. S., Kuznetsova, I. V., 2000, ApJ, 541, 257

Beskin V. S., 2010, MHD Flows in Compact Astrophysical Objects: Accretion, Winds and Jets. Springer-Verlag, Berlin

Bianchi S., Maiolino R., Risaliti G., 2012, AdAst., 2012, 17

Biretta, T., 1996, in Solar and Astrophysical MHD Flows, K. Tsinganos (ed.). Kluwer Academic Publishers, 357, 119

Bisnovatyi-Kogan, G.S., Kazhdan, Ya. M., Klypin, A.A., Lutskii, A.E., Shakura, N.I., 1979, Sov. Astron. 23, 201

Blackman E.G., 2013, EJPh., 34, 489

Blandford, R.D., Znajek, R.L., 1977, MNRAS 179, 433

Blandford, R. D., Payne, D. G., 1982, MNRAS, 1999, 883

Blandford, R. D., Rees, M.J., 1974, MNRAS 169, 395

Bottorff M. C., Korista K. T., Shlosman I., Blandford R. D., 1997, ApJ, 479, 200

Bottorff M. C., Ferland G. J., 2000, MNRAS, 316, 103

Carter B., Henriksen R.N., 1991, JMP, 32, 10, 2580

Casse F., Ferreira J., 2000a, A&A, 353, 1115

Casse F., Ferreira J., 2000b, A&A, 361, 1178

Chajet L. S., Hall, P. B., 2013, MNRAS, 429, 3214

Chiuderi, C., Velli, M., 2012, Fisica del Plasma: Fondamenti e applicazioni Astrofisiche. Springer, Milan

Choudhuri A.R., 1998, The physics of fluids and plasmas. Cambridge University Press, Cambridge

Collin S., Kawaguchi T., Peterson B. M., Vestergaard M., 2006, A&A, 456, 75

Contopoulos J., Lovelace R.V.E., 1994, ApJ. 429, 139

de Kool M., Begelman M. C., 1995, ApJ, 455, 448

Decarli R., Gavazzi G., Arosio I., et al., 2007, MNRAS, 381, 136

Decarli R., Labita M., Treves A., Falomo R., 2008, MNRAS, 387, 1237

Dietrich M., Wagner S. J., Courvoisier T. J. L., Bock H., North P., 1999, A&A, 351, 31

Elitzur M., 2008, NewAR, 52, 274

Elitzur M., Ho L. C., 2009, ApJ, 701, L91

Elitzur M., Ho L., Trump J., 2014, MNRAS, 438, 3340

Elvis M., 2012, JPhCS, 372, 2032

Emmering R. T., Blandford R. D., Shlosman I., 1992, ApJ, 385, 460

Eracleous M., Halpern J. P., 2003, ApJ, 599, 886

Everett J., 2005, ApJ, 631, 689

Feldman W.C., Phillips J.L., Barraclough, B.L., Hammond C.M., 1996, in Solar and Astrophysical MHD Flows, Tsinganos K. (ed.), Kluwer Academic Publishers, 265

Ferland G. J., Porter R. L., van Hoof P. A. M., et al., 2013, RMxAA, 49, 1 (2013 Release of Cloudy)

Ferrarese L., Merritt D., 2000, ApJ , 539, L9

Ferraro V. C. A., 1937, MNRAS, 79, 458

Ferreira J., Pelletier G., 1995, A&A 295, 807

Ferreira J., 1997, A&A, 319, 340

Ferreira J., in Star Formation and the Physics of Young Stars, Bouvier J., Zhan J. P. eds., EDP Sciences, Cambridge, p. 229

Fine S., Croom S. M., Hopkins P. F., et al., 2008, MNRAS, 390, 1413

Fine S., Croom S. M., Bland-Hawthorn J., et al., 2010, MNRAS, 409, 591

Fleishman G. D., Toptygin I. N., 2013, Cosmic electrodynamics: electrodynamics and magnetic hydrodynamics of cosmic plasmas. Springer, New York.

Flohic H. M. L. G., Eracleous M., Bogdanović T., 2012, ApJ, 753, 133

George I. M., Fabian A. C., 1991, MNRAS, 249, 352

Goad M. R., Korista K. T., Ruff A. J. 2012, MNRAS, 426, 3086

Goedbloed J. P. H., Poedts S., 2004, Principles of Magnetohydrodynamics: With Applications to Laboratory and Astrophysical Plasmas, Cambridge University Press, Cambridge

Goldreich P., Julian W. H., 1970, ApJ, 160, 971

Gratton, J., 1991, FCPh, 15, 1

Gultekin K., Richstone D. O., Gebhardt K., et al., 2009c, ApJ, 698, 198

Grad H., Rubin H., 1958, in Proc. 2nd Int. Conf. on Peaceful Uses of Atomic Energy, United Nations, Geneva, 31, 190

Hainline K. N., Shapley A. E., Greene J. E., Steidel, C. C., 2011, ApJ, 733, 31

Haring N., Rix H.-W., 2004, ApJ, 604, L89

Heyvaerts, J., 1996, in Chiuderi C., Einaudi, G., eds, Plasma Astrophysics, Springer-Verlag, Berlin, p. 31

Heyvaerts J., Norman C.A., 1989, ApJ, 347, 1055

Heyvaerts J., Norman C., 2003, ApJ, 596, 1240

Hönig S. F., Beckert T., Ohnaka K., Weigelt G., 2006, A&A, 452, 459

Hönig S. F., Beckert T., 2007, MNRAS, 380, 1172

Kaspi S., Netzer H., 1999, ApJ, 524, 71

Kaspi S., Brandt W. N., Maoz D., et al. 2007, ApJ, 659, 997

Königl A., 1989, ApJ, 342, 208

Königl A., Kartje J. F., 1994, ApJ, 434, 446

Kormendy J, Richstone D. 1995, ARA&A, 33, 581

Krawczyk C. M., Richards G. T., Mehta S. S., et al., 2013, ApJS, 206, 4

Kudoh T., Shibata K. 1997, ApJ, 474, 362

Kurosawa R., Proga D., 2009, MNRAS, 397, 1791

LaMassa S. M., Cales S., Moran E. C., et al., 2015, ApJ, 800, 144

Lawrence A. 1991, MNRAS, 252, 586

Lawrence A., Elvis M., 2010, ApJ, 714, 561

Leighly K. M., 2004, ApJ, 611, 125

Lery, T., 2007, in Ferreira, J. and Dougados, C. and Whelan, E., ed, Jets from Young Stars, Lecture Notes in Physics, Volume 723, Berlin Springer Verlag, p. 185

Li Z.-Y., Chiueh T., Begelman M. C., 1992, ApJ, 394, 459

Li Z.-Y. 1995, ApJ, 444, 848

Livio M., 1997a. In Wickramasinghe, D.T. et al., Eds., Accretion Phenomena and Related Outflows, ASP Conf. Ser., San Francisco, p. 845.

Lorrain P., Lorrain, F., Houle, S., 2006, Magneto-fluid dynamics: fundamentals and case studies of natural phenomena Springer, New York,

Lovelace R. V. E., Berk H. L., Contopoulos J., 1991, ApJ, 379, 696

Lüst & Schlüter 1957, ZNatA, 12a, 850

Lynden-Bell D. 1969, Nature, 223, 690

Lyubarsky Y., 2009, ApJ, 698, 1570

Marconi A., Hunt, L. K., 2003, ApJ, 589, L21

Magorrian J., Tremaine S., Richstone D., et al., 1998, AJ, 115, 2285

Mathews W. G., Capriotti E. R., 1985, in Miller J. S., ed., Astrophysics of Active Galaxies and Quasi-Stellar Objects. Univ. Science Books, Mill Valley, CA, p. 185

Mathews W. G., Ferland G. J., 1987, ApJ, 323, 456

McLure R. J., Dunlop J. S., 2001, MNRAS, 327, 199

McLure R. J., Dunlop J. S., 2002, MNRAS, 331, 795

Meier D.L., 2012, Black Hole Astrophysics: The Engine Paradigm. Springer-Verlag, Berlin, Heidelberg

Mestel L., 1968, MNRAS, 138, 359

Miller J.S., Goodrich B.F., 1990, Ap.J., 355, 456

Mirabel I. F., Rodríguez, L. F., 1996, in Tsinganos K. C. Eds., Solar and Astrophysical Magnetohydrodynamic Flows, Kluwer, p 683

Mor R., Netzer H., Elitzur M., 2009, ApJ, 705, 298

Moran E. C., Barth A. J., Kay L. E., Filippenko,A. V., 2000, ApJ, 540, L73

Mullaney J. R., Alexander D. M., Goulding A. D., Hickox R. C., 2011, MNRAS, 414, 1082

Müller A., Camenzind M., 2004, A&A, 413, 861

Mundell C. G., Pedlar A., Baum S., et al., 1995, in Green D. A., Steffen W. eds., The XXVII Young European Radio Astronomers Conference, in association with Cambridge University Press, p 21, Neutral hydrogen absorption in the Seyfert nucleus of NGC 4151

Murray N., Chiang, J., Grossman S. A., Voit G. M., 1995, ApJ, 451,498

Murray N., Chiang J., 1997, ApJ, 474, 91

Murray N., Chiang J. 1998, ApJ, 494, 125

Nemmen R. S., Brotherton M. S., 2010, MNRAS, 408, 1598

Nenkova M., Ivezić, Ž., Elitzur M. 2002, ApJ, 570, L9

Nenkova M., Sirocky M. M., Ivezić, Ž., Elitzur M., 2008, ApJ, 685, 147

Nenkova M., Sirocky M. M., Nikutta R., et al., 2008, ApJ, 685, 160

Netzer H., 1990, in Blandford R. D., Netzer H., Woltjer L., eds, Saas-Fee Advanced Course 20: Active Galactic Nuclei Springer-Verlag, Berlin, p. 57

Netzer H., 2013, Physics and Evolution of Active Galactic Nuclei, Cambridge University Press, Cambridge

Netzer H., 2015, ARA&A, 53, 365

Osterbrock D. E. 1989, Astrophysics of Gaseous Nebulæ and Active Galactic Nuclei, University Science Books, Mill Valley

Ostriker E.C., 1997, ApJ, 486, 291

Parker E.N., 1958, ApJ, 123, 664

Pelletier G., Pudritz R.E., 1992, ApJ, 394, 117Ð138

Peterson B. M., Wandel A., 2000, ApJ, 540, L13

Phinney E. S., 1983, in Ferrari A., Pacholczyk A. G., eds, Astrophysical Jets. Reidel, Dordrecht, p. 201

Pier E. A., Krolik J. H., 1992, ApJ, 401, 99

Polletta M., Courvoisier T. J.-L., Hooper E. J., Wilkes, B. J., 2000, A&A, 362, 75

Polletta, M., Weedman D., Hönig S., et al., 2008, ApJ, 675, 960

Pudritz, R.E., Norman C. A., 1986, ApJ, 301, 571

Pudritz R. E., Hardcastle M. J., Gabuzda, D. C., 2012, SSRv, 169, 27

Rees M. J. 1984, ARA&A, 22, 471

Rice M. S., Martini P., Greene, J. E., et al., 2006, ApJ, 636, 654

Richards G. T. et al., 2006, ApJ, 166, 470

Richards G. T. et al., 2011, ApJ, 141, 167

Richards, G. T., 2012, in Chartas, G., Hamann, F. and Leighly, K. M., eds, AGN Winds in Charleston Astronomical Society of the Pacific Conference Series, 460, p. 67

Rosso F., Pelletier G., 1994, A&A, 287, 325

Rowan-Robinson 1995, MNRAS, 272, 737

Runnoe J. C., Brotherton M. S., Shang Z., 2012, MNRAS, 422, 478

Rybicki G. B., Hummer D. G., 1978, ApJ, 219, 654

Rybicki, G. B., Lightman, A. P. 1979, Radiative processes in astrophysics, Wiley-Interscience, New York

Rybicki G. B., Hummer D. G., 1983, ApJ, 274, 380

Sari R., Piran T., Halpern J. P., 1999, ApJ, 519, L17

Sauty C., Tsinganos, 1994, A&A, 287, 893

Sauty C., Tsinganos K., Trussoni E., 1999, A&A, 348, 327

Schartmann M., Meisenheimer K., Camenzind M., et al. 2008, A&A, 482, 67

Shafranov V. D., 1958, Sov. Phys. JETP 6, 545

Shafranov V. D., 1960, Sov. Phys. JETP 26, 682

Shakura N.I., Sunyaev, R.A., 1973, A&A, 24, 337

Simpson C., 2005, MNRAS, 360, 565

Silvers, L. J., 2008, RSPTA, 366, 4453

Somov, B. V., 2006, Plasma Astrophysics, Part I: Fundamentals and Practice. Moscow State University, Moscow, Russia Springer New York

Spruit, H. C., 1996, in Wijers, R. A. M. J., Davies, M. B. and Tout, C. A. eds., Physical processes in Binary Stars, Kluwer Dordrecht, NATO Advanced Science Institutes (ASI) Series C, 477, p. 249

Sulentic J. W., Marziani P., Dultzin-Hacyan, D., 2000, ARA&A, 38, 521

Thorne K. S., 1974, ApJ, 191, 507

Tozzi P., Gilli R., Mainieri V., et al. 2006, A&A, 451, 457

Tran H. D, 1995, ApJ, 440, 565

Trussoni E., Tsinganos K., 1993, A&A, 269, 589

Trussoni E., Tsinganos K., Sauty, C., 1997, A&A, 325, 1099

Tsinganos K., Trussoni E., 1990, A&A, 231, 270

Tsinganos K., Trussoni, E., 1991, A&A, 249, 156

Tsinganos K., Sauty C., 1992, A&A, 257, 790

Tsinganos K., Sauty E., Surlantzis G., et al., 1996, MNRAS 283, 811

Tsinganos K., 2007, in Ferreira J., Dougados C., Whelan E. eds, Lecture Notes in Physics, Vol. 723. Theory of MHD Jets and Outflows. SpringerVerlag, Berlin, p. 117

Tsinganos K., 2010, MSAIS, 15, 102

Ueda Y., Akiyama M., Ohta K., Miyaji T., 2003, ApJ, 598, 886

Urry C. M., Padovani P., 1995, PASP, 107, 803

Ustyugova G. V., Koldoba A. V., Romanova M. M., et al., 1999, ApJ, 516, 221

van de Hulst H.C.: Interstellar polarization and MHD waves. In Burgers, J.M., van de Hulst H.C., eds. Problems of Cosmical Aerodynamics, pp. 45Ð57, Central Air Documents Office, Dayton, Ohio

Vanden Berk D. E. et al., 2001, AJ, 122, 549

Vestergaard M., Peterson B. M. , 2006, ApJ, 641, 689

Vlahakis N., Tsinganos K., 1998, MNRAS, 298, 777

Vlahakis N., Tsinganos K., Sauty C., Trussoni E., 2000, MNRAS, 318, 417

Vlahakis N., Königl A., 2003, ApJ., 596, 1030

Weber D.J., Davis, L.J., 1967, ApJ. 148, 217

Whittle M., 1985, MNRAS, 213, 1

Wielebinski R., Beck R., 2005, LNP, Cosmic Magnetic Fields, 664

Zeldovich Y. B., Novikov I. D., 1964, SPhD, 158, 811